Volume 37
DOE/DP40200-83

LLE Review

Quarterly Report

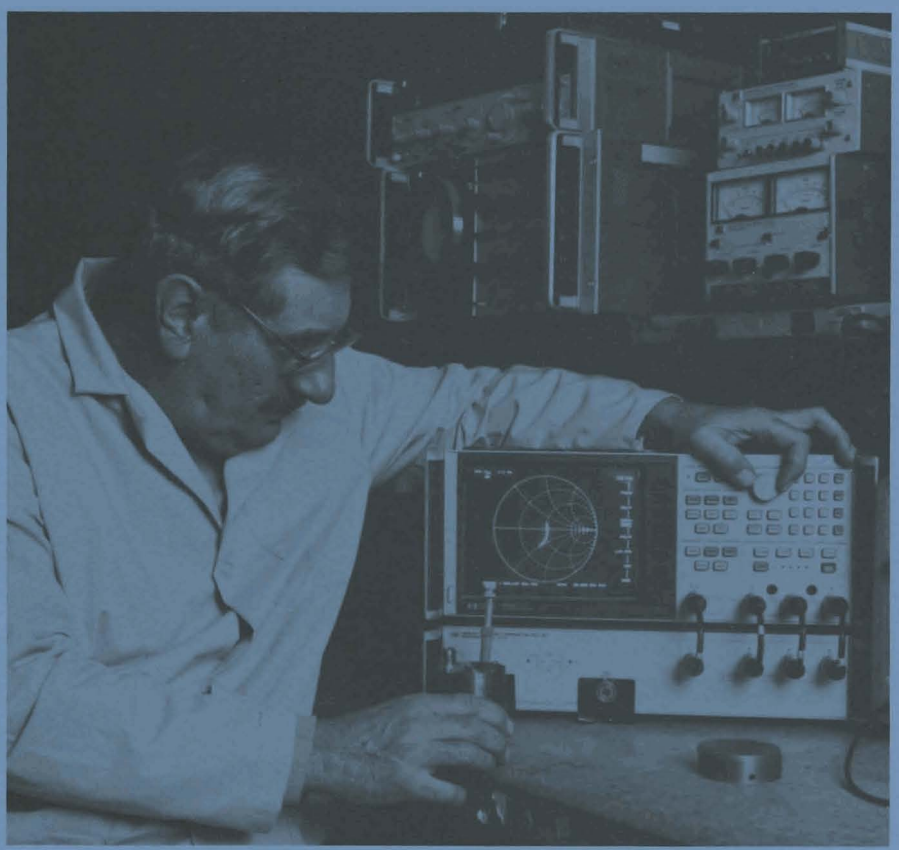

October–December 1988

Laboratory for Laser Energetics
College of Engineering and Applied Science
University of Rochester
250 East River Road
Rochester, New York 14623-1299

Volume 37
DOE/DP40200-83

LLE Review

Quarterly Report

Editor: P. W. McKenty
(716) 275-3865

October–December 1988

Laboratory for Laser Energetics
College of Engineering and Applied Science
University of Rochester
250 East River Road
Rochester, New York 14623-1299

IN BRIEF

This volume of the LLE Review, covering the period October–December 1988, contains several articles devoted to our work in the understanding, identification, and correction of illumination nonuniformities on the OMEGA laser system. Finally, the activities of the National Laser Users Facility and the GDL and OMEGA laser facilities are summarized.

The following are highlights of the research reports contained in this issue:

- The effects of illumination nonuniformities on direct-drive targets are reviewed, identifying the significance of the individual contributions of the long- and short-wavelength nonuniformities on target performance.
- A significant source of illumination nonuniformities—power imbalance between incident laser beams—has been identified. The origins of power imbalance are examined and the steps taken to correct for them on the OMEGA laser system are discussed.
- The theoretical considerations for the implementation of smoothing by spectral dispersion (SSD)—a scheme for achieving high-quality, on-target laser beam patterns—on a laser system such as OMEGA are discussed.
- The physical implementation of SSD on the OMEGA laser system requires the design, engineering, and testing of several complex subsystems. Each subsystem and its introduction into the OMEGA laser system is discussed in detail.

CONTENTS

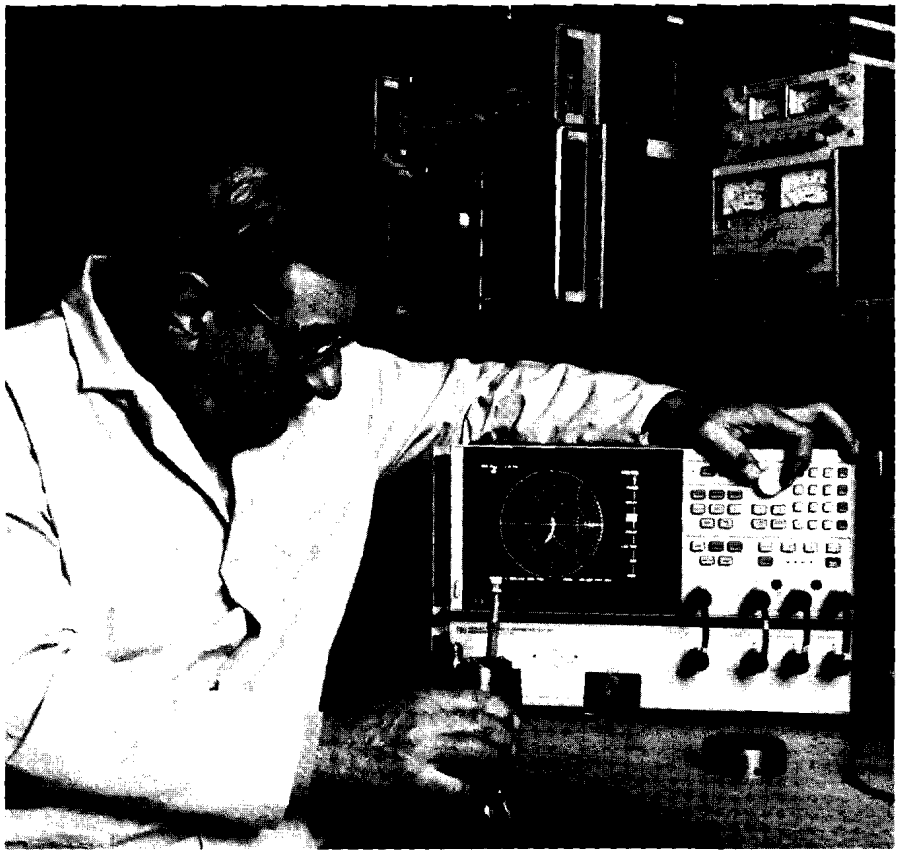

Carl Petras, a research engineer in the Diagnostics Development Group, is shown testing the high-Q, microwave cavity used to drive the lithium niobate phase-modulator employed in the smoothing by spectral dispersion (SSD) scheme on the OMEGA laser system.

Section 1
UNIFORMITY CONSIDERATIONS ON OMEGA

Introduction

To propagate a sustained thermonuclear burn, thereby obtaining useful energy production from an inertial confinement fusion (ICF) implosion, spherical pellets containing deuterium-tritium (DT) fuel must be compressed to ~1000 times their liquid density (XLD) and reach central temperatures of ~5 keV.[1] Two approaches to ICF are presently under active research. The first—indirect drive—uses "hohlraum" targets,[2] converting the incident energy of a driver into x rays that in turn drive the pellet implosion. The second approach—direct drive—directly illuminates a pellet with multiple overlapping laser beams, driving the implosion via electron thermal conduction.

It has been generally recognized in the ICF community that the direct-drive approach to inertial fusion offers the potential for greater pellet gain (the ratio of the thermonuclear energy out to the incident driver energy) at lower incident driver energies than the indirect-drive approach.[2] However, it has been claimed that indirect-drive pellets can obtain better drive uniformity than direct-drive pellets without having the driver be uniform or symmetrically arranged.[2] Therefore, only when the more stringent requirements on illumination and drive uniformity for direct-drive pellets are met can the potential for higher gain be obtained.[3] It is this potential, and its associated cost savings in terms of driver-energy requirements, that makes the study of a direct-drive option to ICF important.

1.A Effects of Illumination Nonuniformities on Direct-Drive ICF Implosions

As an introduction of the effects of illumination nonuniformity on pellet performance, we present results from a direct-drive pellet implosion. Next, the potential role that illumination nonuniformities will play in direct-drive pellet implosions is identified. We have divided the discussion into two broad categories: (1) long-wavelength illumination nonuniformities (those wavelengths for which potential Rayleigh-Taylor unstable growth during the implosion would be small); and (2) short-wavelength nonuniformities (wavelengths for which the potential for exponential growth development during the acceleration phase of the implosion exists). The discussion will show that, although ICF targets are relatively insensitive to isolated long-wavelength (Legendre modes <4) nonuniformities, it is the combination of all modes and their potential mode-mode interactions that must be considered to ensure the success of ICF implosions.

Direct-Drive Pellet Implosion

For this discussion we use a pellet design similar to those used in the recent OMEGA high-density cryogenic implosion experiments.[4] While not all of the conditions required for a low-adiabat, nearly isentropic compression (required for high-gain pellet designs) are met with this target, it is still susceptible to drive distortions and fluid instabilities important to future high-gain designs and, as such, represents an important step in our understanding of future implosions. The pellet, shown schematically in Fig. 37.1, is composed of a 5-μm-thick glass shell with a 125-μm inner radius. The glass shell surrounds a levitated, ~ 4.10-μm-thick cryogenic DT fuel layer (100 atm at room temperature), which in turn surrounds an inner gaseous region of D and T whose density and composition is given by the temperature at which the cryogenic fuel layer is maintained. This type of pellet design is referred to as a "single-shell" design and is similar in nature to future high-gain, direct-drive designs; the main difference being the replacing of the glass ablator with a low-atomic-number (Z) material, such as LiD, CH, or Be.[5] (Due to present target fabrication limitations, experiments have been limited to glass ablators only. The use of low-Z ablators in the cryogenic environment of OMEGA is an area of active research at this time.) The pulse shape used for this simulation was a 650-ps (FWHM) Gaussian with peak power at ~ 1.02 ns from the start of the simulation and 1500 J in the UV (351 nm). The laser-beam spatial profile used was an azimuthally averaged, distributed-phase-plate (DPP) profile.[6] The simulation was performed with the one-dimensional (1-D) hydrodynamics program *LILAC*.

The processes associated with the implosion of this pellet can be outlined as follows. Initially the laser pulse is incident on the outer surface of the glass ablator. The outer layers of the pellet begin to heat, melt, ionize, and ablate from the pellet surface resulting in an

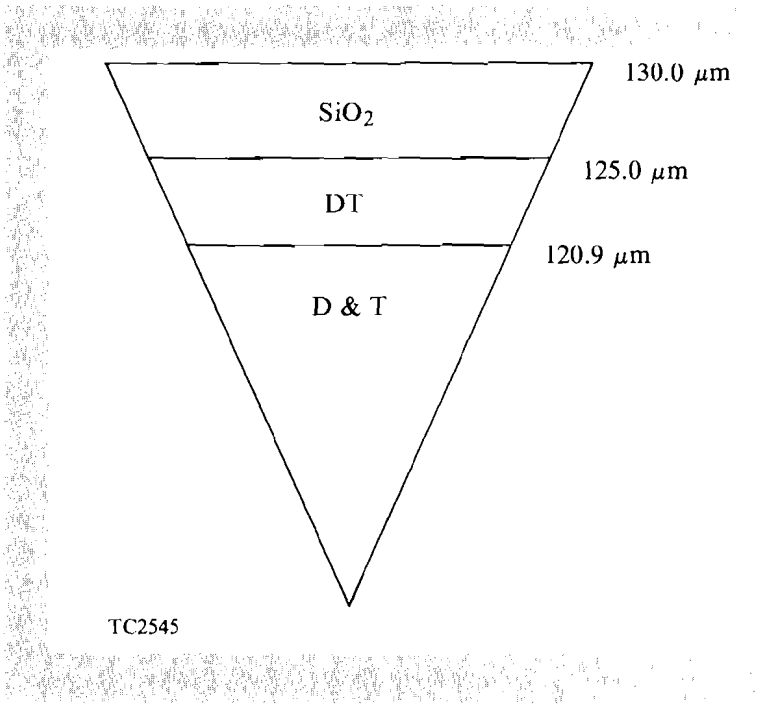

Fig. 37.1
Schematic of single-shell, glass-ablator, OMEGA cryogenic pellet.

outward-expanding, low-density, high-temperature coronal region and an inward-propagating shock wave. The laser energy continues to be deposited, predominantly by inverse bremsstrahlung, in the underdense coronal region. As the laser energy is deposited, energy is transported from the region of deposition (near the critical density region for this implosion) to the unablated pellet material (ablation surface) via electron thermal conduction and, to a lesser extent, ion thermal conduction and radiation transport (x rays generated in the less dense coronal region). This radially inward-conducted energy continues to cause material to ablate from the pellet surface, which results in driving the remaining unablated material inward, acting like a spherical rocket. Figure 37.2(a) displays the radius-versus-time plot for this implosion. The lines in Fig. 37.2(a) represent the motion of Lagrangian fluid markers used in the simulation as a function of time. Those lines that increase in radius as a function of time represent ablated material, while those that decrease represent imploded material. Figure 37.2(b) displays the radius-versus-time history of particular surfaces of interest during the implosion. Figure 37.2(c) displays the in-flight aspect ratio versus time and Fig. 37.2(d) the overdense shell thickness $\Delta R(t)$ as a function of time. [The in-flight aspect ratio $A(t)$ is defined as the time-dependent radius of the overdense shell material $R(t)$ divided by its thickness [i.e., $A(t) = R(t)/\Delta R(t)$]. The shell thickness is determined by locating the peak density in the unablated imploding pellet and then finding the $1/e$ density locations radially outward and inward from this peak density location.[7] The separation of the $1/e$ points determines $\Delta R(t)$ and their average determines $R(t)$. The in-flight aspect ratio and shell thickness are a measure of the susceptibility of a pellet design to unstable hydrodynamic growth development during the implosion. Further discussion appears later in this article.]

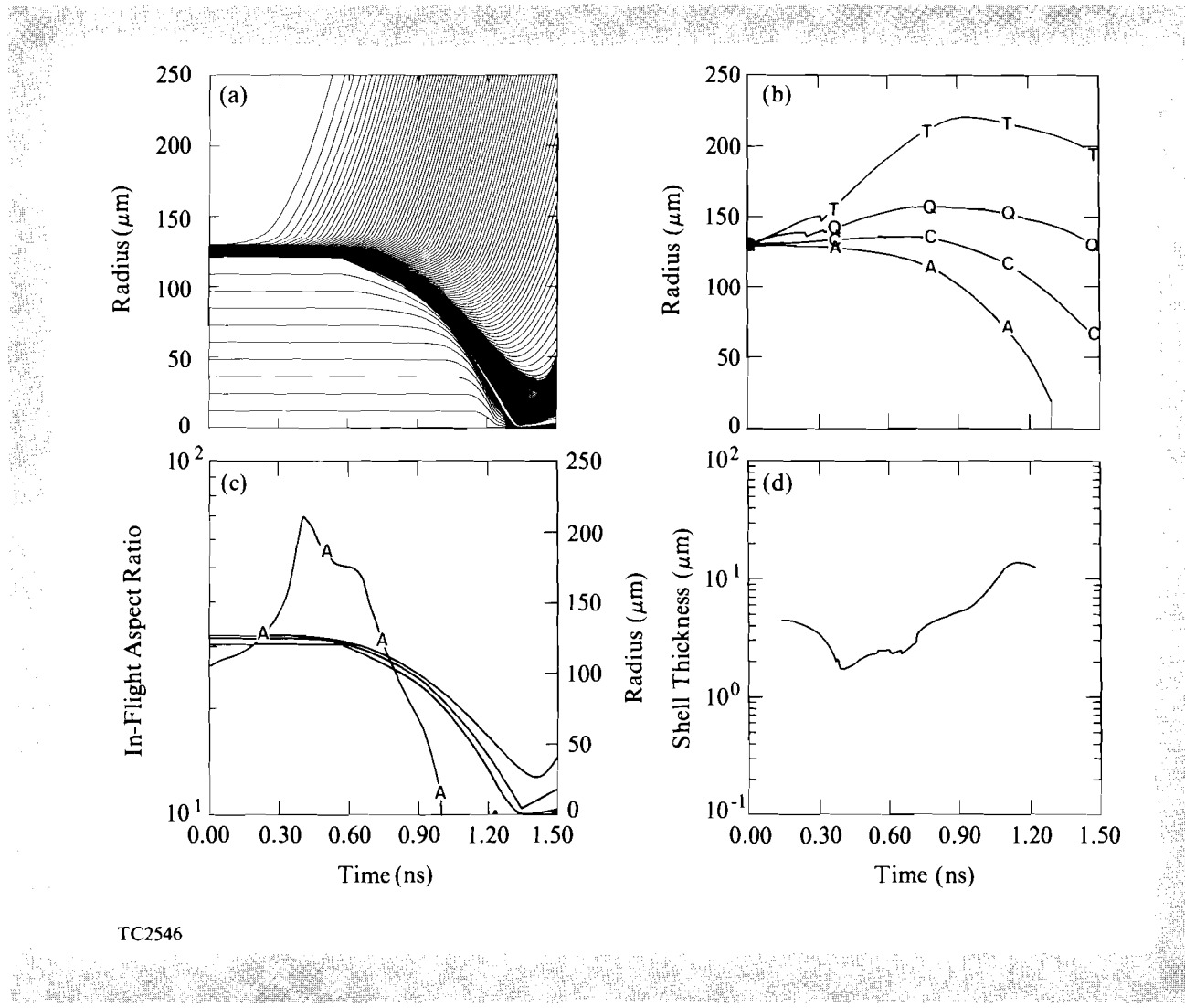

Fig. 37.2
One-dimensional (*LILAC*) hydrodynamics simulation of implosion of the single-shell OMEGA cryogenic target shown in Fig. 37.1.

(a) Radii-versus-time history.
(b) Radius-versus-time history for: A-ablation surface, C-critical surface, Q-quarter-critical surface, and T-tenth-critical surface.
(c) In-flight aspect ratio (curve labeled A) and layer-interface radii versus time.
(d) Overdense shell thickness versus time.

The stagnation phase of this implosion begins to occur at ~1.20 ns. The imploding shell of DT fuel and remaining unablated ablator material are moving inward at $\sim 2.50 \times 10^7$ cm/s at this time. The conversion of shock and kinetic energy and pressure-volume work associated with the continued shell convergence goes into increasing the internal energy of the inner DT-fuel region. The resulting rise in DT-fuel pressure eventually brings the inward motion of the imploding material to a halt at a time referred to as a peak compression. After this time, as shown by the increasing radius trajectories in Fig. 37.2(a) at ~1.40 ns, the pellet begins to disassemble. The minimum radius of the fuel-ablator interface for this example was ~5.50 μm. This represents a radial convergence ratio (C_R), defined as the initial fuel-ablator interface radius divided by its minimum radius during the implosion, of ~25 (high-gain, direct-drive pellet designs have hot-spot convergence ratios of ~25). The peak final core conditions obtained from this simulation were mass-averaged fuel density (ρ) of ~1300

XLD; mass-averaged ion temperature (T_i) of ~0.50 keV; neutron-averaged ion temperature $<T_i>_n$ of ~1.90 keV; neutron-averaged fuel areal density (ρR) of ~98 mg/cm^2; and neutron-averaged ablator areal density ($\rho \Delta R$) of ~59 mg/cm^2.

As shown in the above discussion, the efficiency of conversion of the shock and kinetic energy to internal energy of the central fuel region and the need for large radial convergence to obtain high final fuel densities are critical for successful ICF implosions, whether driven directly or indirectly, and serve to place strict constraints on the drive nonuniformity that a pellet can tolerate during the implosion. There are two important classes of distortions that can be caused by illumination nonuniformities. The first, commonly referred to as secular distortions, can grow linearly in time (t) and/or as t^2. The second, similar to the classical Rayleigh-Taylor fluid instability at an interface of two inviscid fluids,[8-10] can potentially result in the exponential growth in time of initial distortions.

During the inward acceleration phase of an ICF pellet implosion, the cold, dense shell material is being accelerated by the hot, less-dense ablated material. This situation is analogous to the classical Rayleigh-Taylor fluid instability. Numerical simulations have shown that ablation processes act to modify the linear growth rates and nonlinear mode development from those expected from classical fluid simulations.[11-13] This instability is often referred to as the acceleration phase or outside surface instability. The distinction here is made because, during the stagnation phase of the implosion, the dense imploding shell material is decelerated by the hot, less-dense fuel region. Again this situation closely resembles the classical Rayleigh-Taylor instability at an interface for which the Atwood number[10] $\{[(\rho_h - \rho_l)/(\rho_h + \rho_l)]$, where ρ_h is the density of the dense or heavy fluid and ρ_l is the density of the light fluid$\}$ is less than 1 or where the linear growth is modified by the presence of a density scale length.[10,14] This phase of potentially unstable growth development is referred to as the deceleration phase or inside surface instability.

Long-Wavelength Illumination Nonuniformities

For direct-drive laser fusion, long-wavelength illumination nonuniformities can arise from a number of different sources.[15] The dominate sources are (1) the number and placement of individual beams about the target; (2) individual beam mispointing and/or misfocusing; (3) energy balance between individual beams; and, (4) pulse-shape differences between individual beams. Simulations of the contributions to illumination nonuniformity due to the first two sources show that these effects lead to long-wavelength nonuniformities that can change in amplitude during the implosion [due to the motion of the critical surface and coronal plasma formation during the implosion, see Fig. 37.2(b)].[16,17] However, most often they do not result in changes in the phase of the nonuniformities during the implosion. For frequency-tripled glass laser systems, items (3) and (4) have been found to be closely coupled. Energy differences between individual IR (1054-nm) beams can result in not only energy differences in the frequency-tripled UV beams but beam-to-beam pulse-shape variations

due to the nonlinear crystal conversion processes.[18,19] This combined effect of different IR beam energy and the conversion from IR to UV can potentially lead to large-amplitude, long-wavelength modes that can change both in amplitude and phase during the implosion. (The combined effects of items (3) and (4) are referred to as power balance.)

Growth of Rayleigh-Taylor long-wavelength modes should be small. Therefore, constraints on the magnitude of a long-wavelength perturbation that a pellet can tolerate can be obtained from simple dynamics arguments. It can be shown that for secular distortions growing as t^2, the final core distortion δ_F is given by

$$\delta_F = (C_R - 1)\, \Delta a / \bar{a},$$

where C_R is the radial convergence ratio, Δa is the angular variation in the radial acceleration, and $\bar{a}$ is the average radial acceleration. Figure 37.3 displays the calculated-core distortions versus radial-convergence ratio for a number of peak-to-valley acceleration varieties.

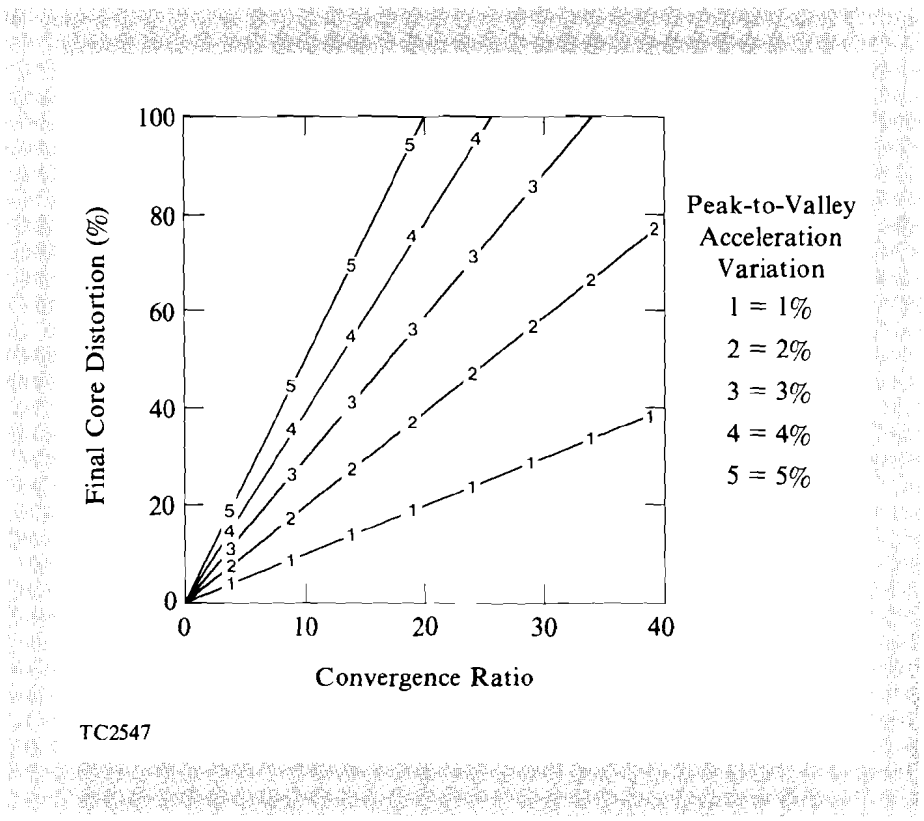

Fig. 37.3
Final core distortions versus radial convergence ratio for various peak-to-valley acceleration variations assuming secular (t^2) distortion.

Depending on the type of target implosion being considered, this figure could be used to estimate the acceleration (drive) nonuniformity that a pellet could tolerate. (For example, for the implosion considered here, an acceleration uniformity of $<3\%$ peak to valley is required to avoid fuel-core distortions $>50\%$.) How this value of drive (acceleration) uniformity relates to illumination uniformity is more complicated and depends on the modeling of the processes associated

with thermal transport and energy deposition.[20,21] The acceleration nonuniformity will be caused by a temperature nonuniformity at the ablation surface resulting from a temperature nonuniformity near critical due to illumination nonuniformities. One simple model for estimating the attenuation of temperature nonuniformities between critical and ablation shows that, classically, the temperature nonuniformity will attenuate as exp $(-k\Delta R_s)$, where ΔR_s represents the separation distance between the critical and ablation surfaces and k is the wave number of the temperature perturbation given by $2\pi/\lambda$ (λ being the perturbation wavelength).[20] In spherical geometry, however, it is useful to refer to nonuniformities in terms of spherical harmonic modes (ℓ). The spherical harmonic modes are not, however, simple waves. Therefore, they can not be defined in terms of a simple wavelength. For purposes of this discussion, however, the planar wave number k and the spherical harmonic number ℓ will be related by the eigenvalue of the two-dimensional (2-D) part of the Laplacian operation resulting in $k^2 = \ell(\ell + 1)/R^2$ where R is the target radius. (For $\ell >> 1$ and a position not near the pole on the sphere $\ell \simeq 2\pi R/\lambda$.) The simple expression for the temperature attenuation becomes exp $\{-[\ell(\ell + 1)]^{1/2}\ \Delta R_s/R\}$ in spherical geometry. By knowing $\Delta R_s/R$ (the "smoothing ratio") one can estimate the required illumination uniformity to assure a given drive uniformity. Since simulations indicate that long-wavelength modes do not change phase during the implosion, if an average value of the time-dependent quantity $\Delta R_s/R$, shown in Fig. 37.4, is used ($\sim$0.35), attenuations of $\sim$0.42, $\sim$0.30, and $\sim$0.21 would result for modes ℓ = 2, 3, and 4, respectively. Therefore, a 3% peak-to-valley drive nonuniformity requires $\leq$7% peak-to-valley illumination nonuniformity.

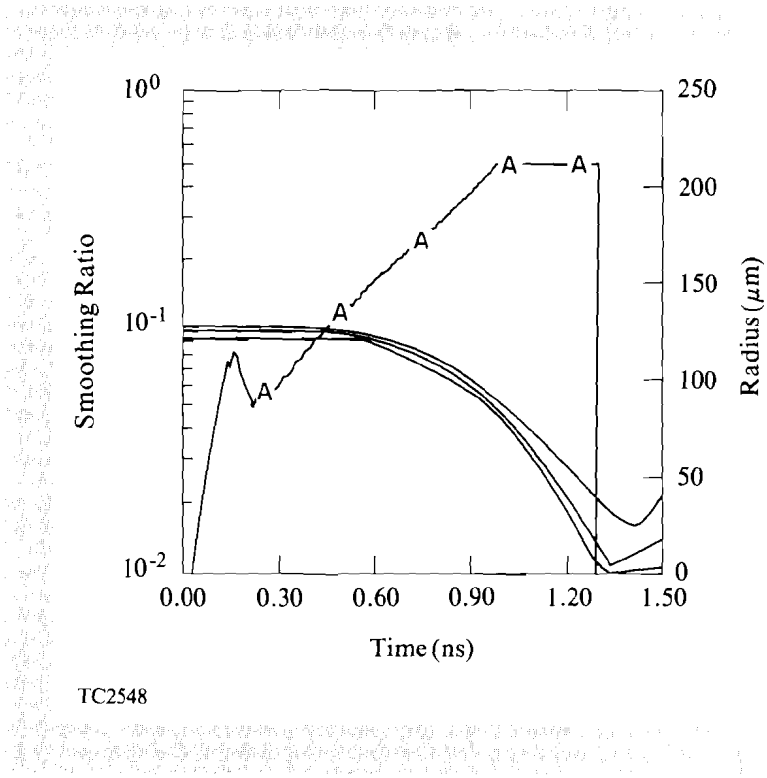

Fig. 37.4
Smoothing ratio ($\Delta R_s/R$) and pellet-interface radii versus time for the single-shell OMEGA cryogenic implosion shown in Fig. 37.1.

The above analysis, while allowing for quick estimates of the illumination uniformity required for long-wavelength modes, is potentially an over-simplification. It does not consider the full time-dependent nature of the problem, the fact that multiple-wavelength nonuniformities may be present, or the possibility of large-amplitude, long-wavelength, nonlinear, mode-mode interactions resulting in shorter-wavelength perturbations during the implosion. Moreover, the effect of long-wavelength nonuniformities on pellet performance is highly dependent on the pellet design. To give an example of the effects of long-wavelength nonuniformities on a pellet implosion, 2-D hydrodynamic simulations were performed using the program *ORCHID*. In these simulations, Legendre modes 1-4 were applied with total peak-to-valley variations of 10%-45%. (The upper end of this range is characteristic of the long-wavelength illumination nonuniformity potentially present because of power imbalance on the first high-density cryogenic implosion experiments carried out on OMEGA.) For the ~45% peak-to-valley case, Fig. 37.5(a) shows the illumination nonuniformity pattern applied for this simulation, while Fig. 37.5(b) displays the density contours at a time when the experimental yield equals the calculated yield.[22] Note that although only long-wavelength modes were initialized, their nonlinear interaction during the final stages of convergence resulted in the evolution of shorter-wavelength perturbations. When the same modes were applied with only ~10% peak-to-valley variations, the mode-mode interactions were minimized and the dominate distortions remained in the mode structure applied. The 2-D simulations have shown that another important consequence of long-wavelength perturbations is that a large fraction of the imploding materials' energy remains in the form of kinetic energy associated with large-scale motion.

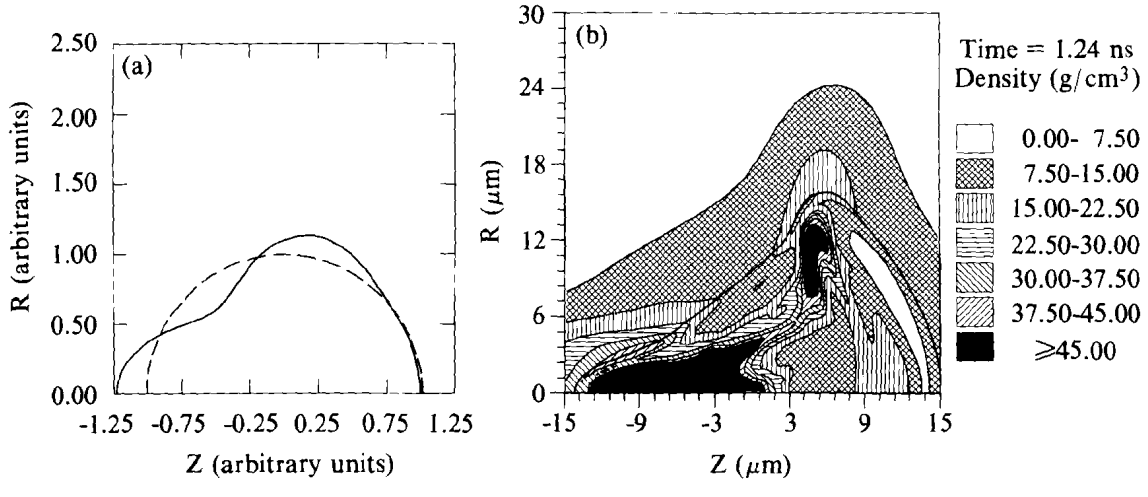

Fig. 37.5
Two-dimensional (*ORCHID*) hydrodynamics simulation of implosion of pellet shown in Fig. 37.1 subjected to long-wavelength nonuniform illumination.
(a) Illumination-nonuniformity pattern placed on target (solid line) modes $1 \leq \ell \leq 4$, peak-to-valley of ~45%.
(b) Density contours (g/cm^3) at the time when the simulation yield equaled the observed experimental yield.

The overall effect on this type of pellet implosion is reduced DT temperatures because of the lower efficiency of kinetic-to-internal energy conversion and longer stagnation times (i.e., the final stagnation phase lasts longer than that predicted from 1-D simulations because of the large-scale mass motion of the core and ablation material during the final stagnation phase of the implosion). These 2-D simulations have shown that, for the pellet considered, the effects of long-wavelength illumination nonuniformities alone can reduce the neutron yield by a factor of ~ 2 in the $\sim 10\%$ peak-to-valley case and by a factor of ~ 15 in the $\sim 45\%$ peak-to-valley case. This does not take into account the potential effect of ablation material (SiO_2) mixing into the fuel because of shear and/or vortex-like flows that develop near the fuel-ablator interface. If these effects were included in the numerical simulations, it would be expected that the neutron yield would be reduced even further due to radiative cooling.

As stated, the effects of long-wavelength perturbations on pellet performance are highly dependent on the pellet design. The example given was a pellet implosion for which even large amounts of long-wavelength nonuniformities resulted in approximately a factor-of-10 reduction in neutron yield. However, simulations performed for high-gain direct-drive designs show that these nonuniformities must be kept below a few percent peak-to-valley to assure good pellet performance.[5] (For these designs, energy of the fuel in the form of kinetic energy associated with large-scale motion resulted in the failure of the central hot spot to ignite.) Therefore, it is very important for direct-drive fusion to be able to identify and control the sources of long-wavelength illumination nonuniformities. (As will be discussed in the next section, when long-wavelength modes coupling with short-wavelength modes is considered, the importance of the long-wavelength modes increases due to the presence of the short-wavelength perturbations.)

The next article in this edition of the LLE Review identifies a major source of long-wavelength nonuniformities for frequency-tripled glass laser systems and describes the progress that is underway to understand and control it on the OMEGA laser system. (Simulations have shown that because of the limited number and placement of individual beams on OMEGA, residual, long-wavelength nonuniformities will always be present on experiments carried out on the OMEGA laser system.)[15]

Short-Wavelength Illumination Nonuniformities

For direct-drive pellet implosions, short-wavelength nonuniformities arise mainly from individual beam profiles and their overlap on target.[15] The amplitudes and phases of these modes can change during the pellet implosions because of the motion of the critical surface and coronal plasma changes during the implosion [see Fig. 37.2(b)].[17]

Understanding the effects of short-wavelength illumination nonuniformities on pellet performance is an area of active research for all approaches to ICF. These modes are important because they can potentially drive secular distortions, and, more importantly, act as initial amplitude "seeds" for Rayleigh-Taylor unstable growth.

Numerical simulations have shown that the ablation process affects both the linear and nonlinear growth evolution of this instability.[11-13] To estimate the importance associated with short-wavelength illumination nonuniformities, a model is required for the development of the outside-surface Rayleigh-Taylor unstable growth and its potential feed through to the inside surface of the shell. In the past, many authors have presented estimates of the consequence of Rayleigh-Taylor unstable growth on pellet performance based on a "worst-wavelength" analysis (i.e., the mode for which $\lambda_w \approx 2\pi\Delta R$, where λ_w is the "worst" mode wavelength and ΔR is a characteristic shell thickness during the implosion). Linear growth rates were obtained for this mode using perturbation methods or full 2-D simulations. Based on the growth rates obtained, the number of e-foldings expected during the implosion could be estimated. If the analysis showed that the shell could potentially rupture (the perturbation amplitude becomes comparable to the shell thickness during the implosion), then the pellet design was considered suspect. If, however, this analysis showed that the growth of this worst mode was not a problem, it was assumed that the target design was "safe" with respect to Rayleigh-Taylor unstable growth. Recently a number of important studies, both experimental[23] and theoretical,[24,25] have shown that these conclusions may have been overly optimistic. These studies now show that it is the contribution of all the unstable modes and their potential mode-mode interactions, and not just a single wavelength, that must be considered.

At this time, the treatment of all potentially unstable modes, including both linear and nonlinear evolution, during an ICF pellet implosion is beyond the capabilities of most ICF simulation programs. Therefore, models have been developed that estimate the unstable growth and its potential effect on pellet performance. These models use perturbation calculations to determine linear growth rates for the appropriate spectral range (or 2-D simulations of single-mode evolution to determine linear growth rates and nonlinear evolution information) and zeroth-order hydrodynamic information from 1-D simulations of the pellet implosion of interest. The evolution of the unstable growth development is carried out on a noninterfering (no self-consistant hydrodynamics) basis. The results can then be used to estimate the amount of shell distortion and ablator-fuel mixing that could take place during the implosion. These estimates are then used to determine the susceptibility of a given pellet design to failure due to mixing, or identify a limited region in wavelength space that is of particular importance during the implosion that can be simulated with present 2-D hydrodynamics codes. A model has been developed based on these ideas, but it treats the nonlinear saturation of unstable modes based on the interaction of a number of modes about a particular mode of interest,[25] as opposed to using results from single-mode calculations showing that a mode transits from linear to nonlinear growth when the amplitude-to-wavelength ratio becomes approximately 0.10 to 0.20.[13] A model similar to that developed in Ref. 25 will be used to obtain estimates of the importance of short-wavelength illumination nonuniformities on the cryogenic pellet implosion considered here.

Zeroth-order dynamics were obtained from the 1-D *LILAC* simulation. In this discussion, we will use the linear growth rate relation found in Ref. 11: $\gamma = \alpha \sqrt{ka} - \beta k V_a$, where $\alpha = 0.90$, $\beta \approx 3$–4, k is the wave number, a is the acceleration, and V_a is the ablation velocity that is determined from $\dot{m}/\hat{\rho}$ ($\dot{m}$ is the mass-flux rate and $\hat{\rho}$ is the peak density). This model tracks the growth of individual ℓ-modes using linear growth rates until a saturation amplitude is reached. For the outside surface instability, we are interested in the development of the bubble; therefore, once the mode goes nonlinear, the bubble grows linearly in time.[26–28] (Recent studies of finite fluid layers show that the nonlinear bubble evolution departs from this expression when the layer thickness gets small.[13,29] However, this model is used only to illustrate the potential effects of the instability; therefore, no attempt has been made to try to treat the nonlinear stages more accurately.) The model also tracks the inside-shell perturbations during the implosion. During the acceleration phase this is given by the classical feedthrough result of $\exp(-k\Delta R)$.[8] Once the inside surface begins to decelerate, this amplitude serves to seed the inside unstable growth that is evolved using the growth rate found in Ref. 14 and the density scale length of interest obtained from the *LILAC* simulation. If the mode evolves into the nonlinear region during the deceleration phase, nonlinear evolution is assumed proportional to $\delta a t^2$ in an attempt to follow the spike development, where δ is $\leq \frac{1}{2}(\delta = \frac{1}{2}$ for an Atwood number equal to 1) and is obtained from 2-D simulations. There are a number of limitations associated with this kind of model; the reader is referred to Ref. 25 for a detailed discussion of these limitations and their possible consequences. (According to Ref. 25, these models can be "normalized" against the work provided by Refs. 23 and 24 as a guidance for their use at this time.)

Two model calculations are presented. The first assumes an initial amplitude of modes that is random in phase and of uniform amplitude equal to 0.01 μm for $1 \leq \ell \leq 250$. (The DPP's now in use on OMEGA have individual small-scale sizes of the order of 3 to 5 μm, and simulations of the resulting overlap pattern show that structures comparable to this size exist.)[6] This assumes that the overlap-DPP pattern imprints itself on the target uniformly. The second example assumes that some thermal smoothing of the DPP-overlap pattern has taken place before the distortions imprinted themselves on the target and was taken to be $\xi(\ell) = 0.01 \exp\{-0.01\,[\ell(\ell+1)]^{1/2}\}$, where 0.01 represents a minimal thermal smoothing ratio (see Fig. 37.4). Figures 37.6(a) and 37.6(b) show the results of these two model cases for the predicted distortions on the outside surface (solid line) and inside surface (dashed line) during the acceleration phase. It can be seen from these figures that if, as in Refs. 23 to 25, it is the amplitude of all of the unstable notes that are of importance, the reduction and/or removal of modes $\gtrsim 25$ is extremely important to pellet performance (accomplished in the second example by assuming some thermal smoothing). Figures 37.6(c) and 37.6(d) show the results for the inside unstable growth for the two cases. From these figures it can be seen that, while the assumed thermal smoothing would have an important

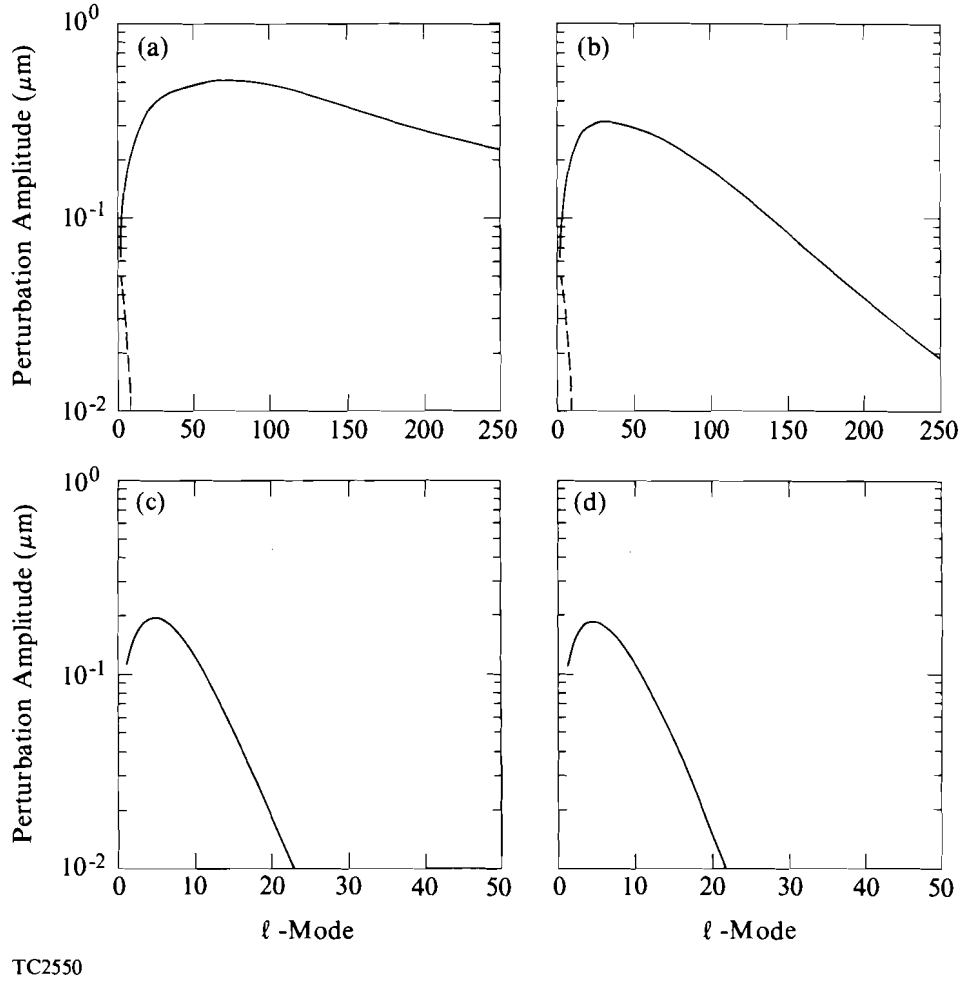

Fig. 37.6
Rayleigh-Taylor growth (model) calculations for single-shell OMEGA cryogenic pellet shown in Fig. 37.1. Two initial amplitude cases are shown. The first is for an initial amplitude of 0.01 μm for $1 < \ell < 200$. The second is for initial amplitudes given by $0.01\ e^{-0.01\ [\ell(\ell+1)]^{1/2}}$.
(a) Ablation surface (solid line) and shell inside-surface (dashed line) growth for acceleration phase with initial amplitudes given by case 1.
(b) Same as Fig. 37.6(a) except initial amplitudes given by case 2.
(c) Inside-surface growth for case 1.
(d) Inside-surface growth for case 2.

effect on the outside unstable growth, the development of the inside instability is virtually the same for both cases.

A 2-D *ORCHID* simulation was performed to examine the behavior of this pellet when subjected to modes of nonuniformity in the range 2 through 20, which the model runs identified as important during the deceleration phase. The amplitudes of the modes were obtained from calculations of the σ_{rms} associated with the individual modes assuming perfect energy balance and the use of 24 identical DPP beams on OMEGA.[6] (The phases were randomly determined for each mode.) Both the illumination-uniformity pattern for this simulation and a density contour near the time when the simulation yield equals the experimental yield[22] are shown in Figs. 37.7(a) and 37.7(b), respectively. The large distortions in the material density in Fig. 37.7(b) are confined mainly to the inner DT-fuel region. (The glass ablator has also become distorted; however, its density variations are not apparent due to the choice of contour levels used in the figure.)

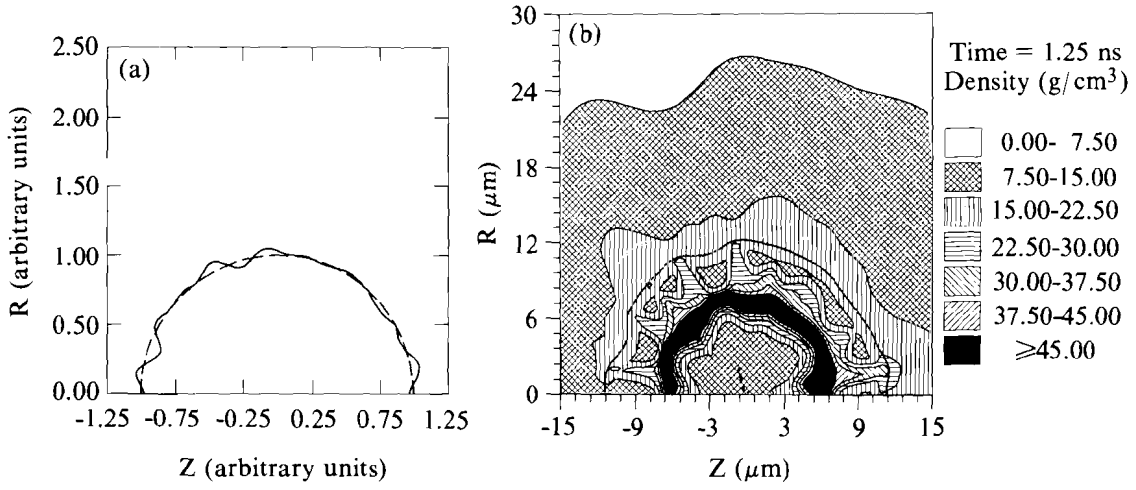

Fig. 37.7
Two-dimensional (*ORCHID*) hydrodynamics simulation of implosion of pellet shown in Fig. 37.1 subjected to nonuniform illumination in modes $2 \leq \ell \leq 20$.

(a) Illumination-nonuniformity pattern placed on target (solid lines) modes $2 \leq \ell \geq 20$ with a total peak-to-valley of $\sim 15\%$.

(b) Density contours (g/cm^3) at the time when the simulation yield equaled the observed experimental yield.

This simulation showed that (1) the final neutron yield was reduced by approximately a factor of 10 from the 1-D simulation; (2) mixing of fuel and ablator material was confined to a region near the fuel-ablator interface; and (3) the modes were initially imprinted by the illumination-nonuniformity pattern before growing exponentially. (The Rayleigh-Taylor unstable growth is actually more complicated than the simple model examples discussed previously: Simulations show that there are actually two Rayleigh-Taylor unstable surfaces during the pellet implosion phase. The first is located at the ablation surface; the second at the DT-ablator interface where, when this interface is approximately 90 μm away from the origin, an unstable interface configuration arises with an Atwood number of ~ 0.20.) Other single-mode simulations of shorter-wavelength perturbations (ℓ = 48, 60) on this pellet have shown Rayleigh-Taylor unstable growth during the acceleration phase. However, their effect on the inside unstable development is smaller than those for $\ell \leq 20$ as predicted from the simple Rayleigh-Taylor growth model. These simulations also indicate that growth is taking place over the range of modes considered to date ($\ell \leq 60$). If the estimates of Rayleigh-Taylor unstable growth predicted by the simple model are correct, the treatment of all of the unstable short-wavelength modes to determine the effect on pellet performance would be required and may explain the larger departure of observed experimental yields from those which have been simulated to date. (Two-dimensional simulations are in process to more accurately determine the initial amplitude seeds potentially imposed on these implosions and their resulting linear growth rates in order to predict the potential effects of Rayleigh-Taylor unstable growth on these pellets. Once these seed amplitudes and growth rates are determined, the simple model could be used to determine if a particular region in wavelength space could be identified to examine the effect of potential fuel-ablator mixing during the implosion phase.)

The removal and/or reduction of short-wavelength illumination perturbations in direct-drive pellet implosions is extremely important. Methods to reduce these illumination modes are under study and development at a number of ICF laboratories.[30-35] At LLE, we are studying and implementing on the OMEGA laser system a method to reduce these modes—smoothing by spectral dispersion (SSD).[36] This theoretical and experimental program is presented and discussed in the third and fourth articles in this review.

In summary, we have attempted to show the potential effects of illumination nonuniformities on direct-drive pellet implosions. We have done this by breaking their effects into two relatively arbitrary categories for purposes of discussion. In reality, it is the combination of all the illumination nonuniformity modes and their potential mode-mode interactions that must be considered. (Two-dimensional simulations of the combination of large-amplitude, long-wavelength modes $\ell \leq 4$ in conjunction with short-wavelength modes $\ell \leq 20$ show that the short-wavelength modes are "carried" on the long-wavelength modes into regions in the core where they would not have been expected if only the short-wavelength modes were present.) Work is presently underway at LLE on the OMEGA laser system to address improvements over the entire range of illumination nonuniformities and experimentally investigate the effects of the residual illumination nonuniformities on direct-drive pellet implosions.

ACKNOWLEDGMENT

This work was supported by the U.S. Department of Energy Office of Inertial Fusion under agreement No. DE-FC03-85DP40200 and by the Laser Fusion Feasibility Project at the Laboratory for Laser Energetics, which has the following sponsors: Empire State Electric Energy Research Corporation, New York State Energy Research and Development Authority, Ontario Hydro, and the University of Rochester. Such support does not imply endorsement of the content by any of the above parties.

REFERENCES

1. J. H. Nuckolls, L. Wood, H. A. Thiessen, and G. Zimmerman, *Nature* **239**, 139 (1972).
2. J. H. Nuckolls, *Phys. Today* **35**, 24 (1982).
3. Lawrence Livermore Laboratory Laser Program Annual Report, UCRL-50021-86, 2-1 (1986).
4. R. L. McCrory, J. M. Soures, C. P. Verdon, F. J. Marshall, S. A. Letzring, S. Skupsky, T. J. Kessler, R. L. Kremens, J. P. Knauer, H. Kim, J. Delettrez, R. L. Keck, and D. K. Bradley, *Nature* **335**, 225 (1988).
5. LLE Review **23**, 125 (1985).
6. LLE Review **33**, 1 (1987).
7. J. D. Lindl (private communication).
8. G. J. Taylor, *Proc. R. Soc. London, Ser. A*, **201**, 192 (1950).
9. D. J. Lewis, *Proc R. Soc. London, Ser. A*, **202**, 81 (1950).

10. S. Chandraskhar, *Hydrodynamic and Hydromagnetic Stability* (Clarendon Press, Oxford, England, 1961), Chap. 10.

11. H. Takabe, K. Mima, L. Montierth, and R. L. Morse, *Phys. Fluids* **28**, 3676 (1985).

12. M. H. Emery, J. H. Gardner, and J. P. Boris, *Phys. Rev. Lett.* **48**, 677 (1982).

13. C. P. Verdon, R. L. McCrory, R. L. Morse, G. R. Baker, D. I. Meiron, and S. A. Orszag, *Phys. Fluids* **25**, 1653 (1982).

14. R. LeLevier, G. Lasher, and F. Bjorklund, Lawrence Livermore National Laboratory Report UCRL-4459 (1955).

15. S. Skupsky and K. Lee, *J. Appl. Phys.* **54**, 3662 (1983).

16. A. J. Schmitt and J. H. Gardner, *J. Appl. Phys.* **60**, 6 (1986).

17. P. W. McKenty, S. Skupsky, C. P. Verdon, and R. L. McCrory, *Bull. Am. Phys. Soc.* **32**, 1740 (1987).

18. W. Seka, S. D. Jacobs, J. E. Rizzo, R. Boni, and R. S. Craxton, *Opt. Commun.* **34**, 469 (1980).

19. R. S. Craxton, *Opt. Commun.* **34**, 474 (1980).

20. S. E. Bodner, *J. Fusion Energy* **1**, 221 (1981).

21. LLE Review **36**, 172 (1988).

22. LLE Review **35**, 97 (1988).

23. K. I. Read, *Physica* **12D**, 45 (1984).

24. D. L. Youngs, *Physica* **12D**, 32 (1984).

25. S. W. Haan, Lawrence Livermore National Laboratory Report, UCRL-98206 (1988).

26. G. Birkhoff and D. Carter, *J. Math. Mech.* **6**, 769 (1957).

27. P. R. Ganabedina, *Proc. R. Soc. London A* **241**, 423 (1957).

28. G. R. Baker, D. I. Meiron, and S. A. Orszag, *Phys. Fluids* **23**, 1485 (1980).

29. G. R. Baker, R. L. McCrory, C. P. Verdon, and S. A. Orszag, *J. Fluid Mech.* **178**, 161 (1987).

30. Y. Kato *et al.*, *Phys. Rev. Lett* **53**, 1057 (1984).

31. R. H. Lehmberg and S. P. Obenschain, *Opt. Commun.* **46**, 27 (1983).

32. S. P. Obenschain *et al.*, *Phys. Rev. Lett.* **56**, 2807 (1986).

33. R. H. Lehmberg, A. J. Schmitt, and S. E. Bodner, *J. Appl. Phys.* **62**, 2680 (1987).

34. R. H. Lehmberg and J. Goldhar, *Fusion Tech.* **11**, 532 (1987).

35. D. Veron *et al.*, *Opt. Commun.* **65**, 42 (1988).

36. LLE Review **36**, 158 (1988).

1.B Implementation of Power Balance on OMEGA

The stringent requirements for the irradiation uniformity for laser fusion, as reviewed in the previous article, have been known for quite some time. We have spent a significant effort on improving the irradiation patterns of the individual laser beams at the target surface as well as their energy balance and various geometrical effects due to beam disposition, pointing, and focusing.[1] In the process we have shown significant improvement in the laser performance with respect to overall (time-integrated) intensity distributions on target. In the area of irradiation patterns on target, the implementation of distributed (random) phase plates in each of the 24 high-power laser beams on OMEGA has shown, through the evaluation of equivalent-target-plane distributions, a decrease in the on-target nonuniformities by about a factor of 5.[2] In balancing the energy of the incident beams, which requires compensating for the varying performance of each of the 24 third-harmonic conversion crystals by adjusting the incident, 1054-nm laser energy, we have traditionally been able to maintain an on-target UV energy balance of ~6% rms. Regardless of these accomplishments, computational analysis of our recent high-density campaign has shown that there must be additional sources of nonuniformity that had not been previously considered.

We now believe that an important factor has been a time-varying illumination nonuniformity on target resulting from an inadequate power balance, i.e., the requirement that the instantaneous 351-nm power produced by the crystals balances at all times during the laser pulse. It is important to realize that good energy balance does not guarantee good power balance; for example, when the UV energy balance on previous targets was measured to be a modest 6% rms, the actual power imbalance, as will be shown later in this article, could have easily been in excess of 20%–30% rms. (Furthermore, power balance out of the crystals will not ensure intensity balance on target if the spot sizes of the individual beams are not the same. Strong air turbulence in the beam path or large, laser *B*-integral effects are examples that can lead to intensity imbalance on target, even when the power out of the crystals is balanced. However, our use of distributed phase plates reduces the sensitivity to spot-size changes and changes in intensity distribution in the target plane compared to experiments carried out without phase plates.)

After realizing the possibility of large power imbalance on the OMEGA laser system, a system review identified two areas of concern. The first was the state of polarization in each beam upon entry into the third-harmonic conversion crystals. It was found that, on average, each beam behaved as if it was detuned by ~200 μrad. This problem was solved with the insertion of output polarizers after the final 90-mm rod amplifiers. The second problem was found in the manual procedure for obtaining energy balance. The alleviation of this problem required the installation of a system of photodiodes to monitor

the oscillator energy and a series of computer-controlled, motorized splitter wave plates to allow the movement of all wave plates to within 0.05°. The improved polarization into the third-harmonic conversion crystals and improved tuning procedures now allow for a 2%-rms deviation from the optimum performance (worst beam ~100 μrad detuned) and with the computerized wave-plate system in place, the OMEGA laser system can now routinely obtain UV energy balance in the range of 2%–3% rms.

Origins of Power Imbalance

Power imbalance due to different temporal pulse shapes of the individual beams can arise from beam-to-beam differences in nonlinear processes such as frequency conversion[3] and saturation of the laser amplifiers.[4] For our laser the latter is of minor importance. However, the time-integrated, as well as the time-dependent, third-harmonic conversion efficiencies are very sensitive to crystal alignment, polarization (angle of linearly polarized light relative to the crystal axes and the uniformity of polarization across the beam), phase front, crystal thickness, and intensity distribution at the input to the crystals, and, as such, influence the temporal shape of the UV output pulses. The problem is exacerbated if such imperfect crystal performance is compensated for by increasing the IR laser energy incident on the crystal.

The well-known dependence of the time-integrated third-harmonic energy conversion efficiency as a function of peak input intensity to the conversion crystals is shown in Fig. 37.8. In this figure we have assumed 16-mm-thick KDP crystals for the doubler and the tripler, an idealized "top-hat" near-field intensity distribution, and a Gaussian temporal pulse shape. Also shown in this figure are conversion efficiencies for different values of the tuning and polarization angles. The effects of these conversion curves on the output temporal pulse shapes have been recognized for a long time, but their full impact on actual laser-fusion experiments has become obvious only recently. Figures 37.9(a) and 37.9(b) show typical examples of the calculated output pulse shapes for different detuning angles on linear and logarithmic scales, respectively. Only the rising parts of the Gaussian pulses are shown in the figures; the IR input energies to the crystals were adjusted such as to yield constant blue output energies independent of the tuning conditions consistent with past experimental OMEGA practice.

From Fig. 37.8 we note that the conversion efficiencies for different 3ω tuning conditions differ significantly from each other only at incident IR intensities above a few tenths of a GW/cm^2. Temporal pulse-shape distortion due to crystal detuning occurs, therefore, only in this intensity regime (i.e., within approximately the top decade of the temporal pulse shape). In the small-signal conversion regime the UV pulse shape is always predictably narrowed relative to the input Gaussian pulse shape (i.e., the wings are steepened), while above the small-signal conversion regime detuned crystals always flatten the top of the UV pulse and in some cases can even lead to a dip near the peak-incident IR pulse.

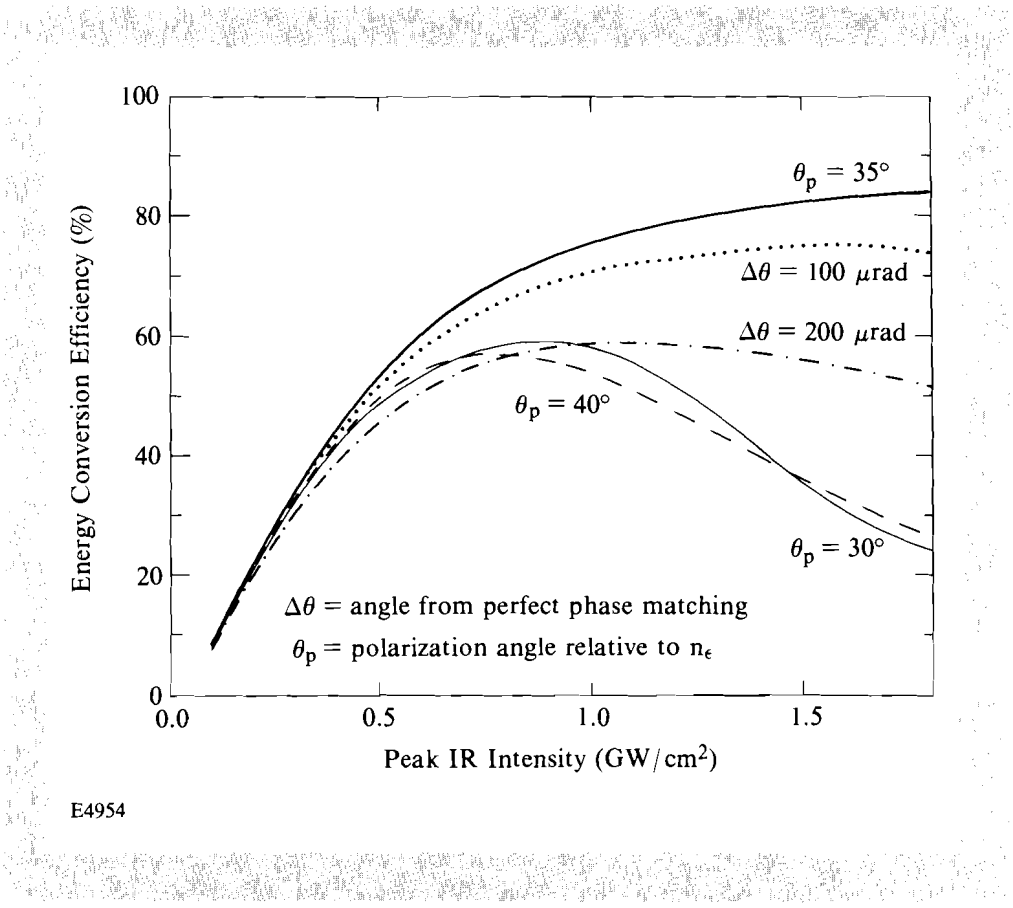

Fig. 37.8
Third-harmonic energy-conversion efficiency for type II-type II tripling in two 16-mm-thick KDP crystals for various tuning conditions: tripler tuning angle θ = 0, 100 μrad, and 200 μrad, and polarization angle θ_p = 30°, 33°, 35°, 37°, and 40° relative to the "*e*" axis of the input doubler crystal. [Note: the intensity axis scales as IL^2 and can therefore be applied easily to crystal pairs of different thicknesses provided the detuning angles are also scaled by θ_L.]

From Fig. 37.9(b) we see that while all the curves resemble each other at low intensities, they appear to be displaced in time. For laser fusion we require that the instantaneous deviations from the average intensity on target not differ by more than a few percent peak-to-valley at any time during the laser pulse. While OMEGA targets are illuminated by 24 beams, only four beams contribute significantly to the intensity on target at any particular point; thus, the 4% to 5% peak-to-valley illumination nonuniformity on target may relax to 8% to 10% peak-to-valley nonuniformity from beam to beam. Inspecting Fig. 37.9 one can easily see that, even for beams of equal energy, very large instantaneous intensity imbalances can occur between more-or-less perfectly frequency-converted beams. In Fig. 37.10 this is shown as $\Delta I/I$ as a function of time for the pulses shown in Fig. 37.9. The baseline for comparison in this figure was the perfectly tuned pulse (heavy line in Fig. 37.9); the worst instantaneous intensity deviation was determined for a crystal detuned by 200 μrad. Of course, larger detuning angles lead to even higher values of $\Delta I/I$. The bottom two curves in Fig. 37.10 are calculated for perfectly tuned tripling crystals but with 20% less IR input energy to the conversion crystals (~30% less UV crystal output). Curve 4 (second from bottom) has equal energy on target as a result of an assumed, rather extreme 30% difference in UV transport losses (Note: these do not represent OMEGA operating conditions). The bottom curve corresponds to a pulse whose energy on target is 30% less than nominal. The latter

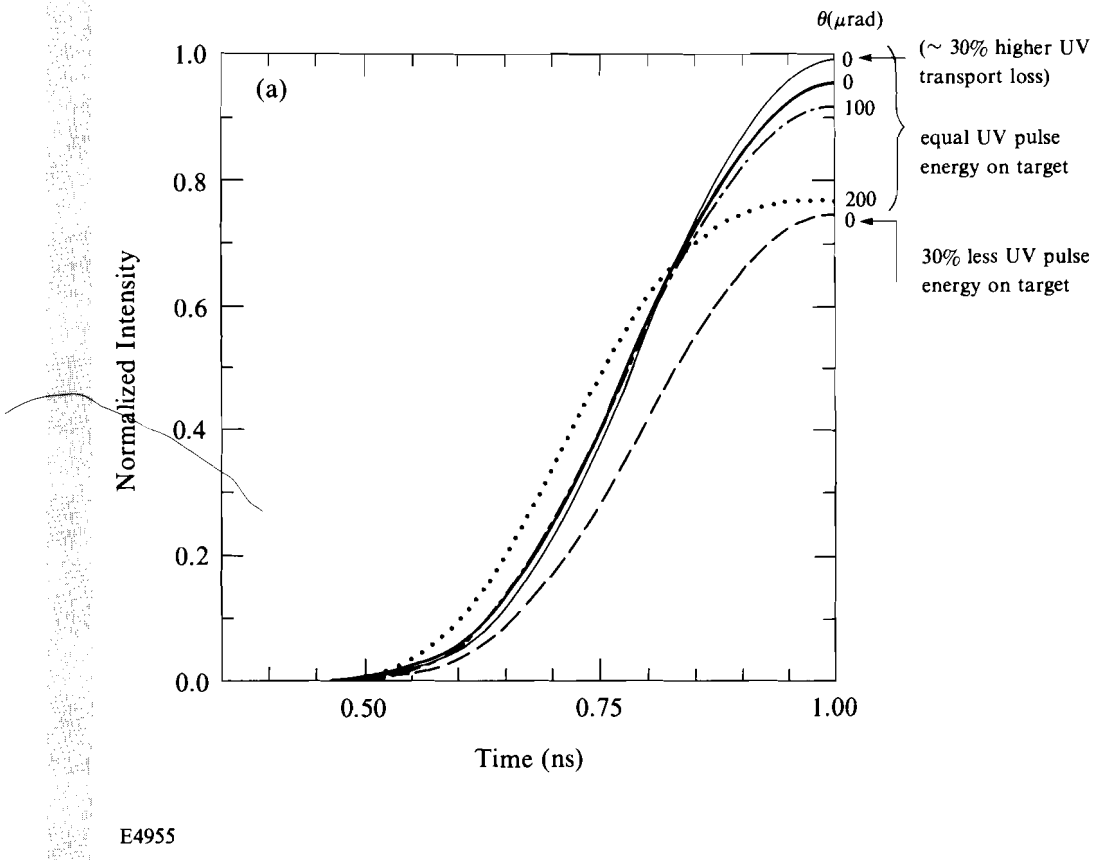

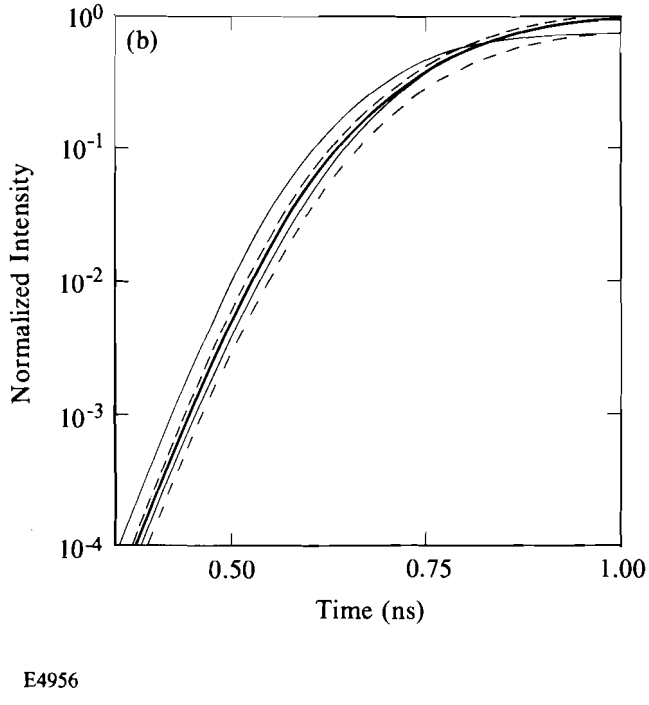

Fig. 37.9
Temporal pulse shapes of frequency-tripled Gaussian IR pulses of 500-ps FWHM and nominal IR peak intensity of 1 GW/cm^2. The angular detuning of the tripler crystal is indicated in μrad. All pulses (except the bottom curve) have been normalized to equal energy on target by compensating the IR input energy to the conversion crystals. The top curve for zero detuning is a mock-up for a beam whose transport losses between crystal and target area are arbitrarily assumed to be 30% less than for the other pulses while maintaining equal energy on target. The bottom curve in (a) has been calculated for 30% less UV energy on target, which is a typical peak-to-valley fluctuation in beam energy for a 6% to 8% beam-energy balance on target. In (b) the same pulse shapes are drawn on a logarithmic intensity scale.

pulse is consistent with a 5%- to 8%-rms beam-energy balance for which peak-to-valley excursions between individual beam energies typically reach 30%.

The $\Delta I/I$ curves of Fig. 37.10 show that the differential losses between the beam lines cannot be made up by simply adjusting the IR input energies to the crystals. This is, of course, a consequence of the changing third-harmonic conversion efficiency in the high-intensity regime rather than the transport losses that are relatively benign linear losses. On the other hand, large IR energy imbalances of ~20% peak-to-valley lead to instantaneous intensity imbalances in the UV of >50%, far in excess of the permissible levels for laser fusion. The situation becomes truly dramatic if one couples detuning problems with random beam energy fluctuations (5% to 8% rms has been typical for routine OMEGA operations) in which case instantaneous beam-intensity imbalances of several hundred percent can easily be realized.

Fig. 37.10
Time-dependence of the fractional intensity differences between the various pulses in Fig. 37.9. All curves are relative to the perfectly tuned case (second from top at the peak of the pulse in Fig. 37.9). We note that the maximum-intensity differences occur at about 1 FWHM from the peak of the IR pulse at a UV intensity of $\sim 10^{-3}$ of the peak.

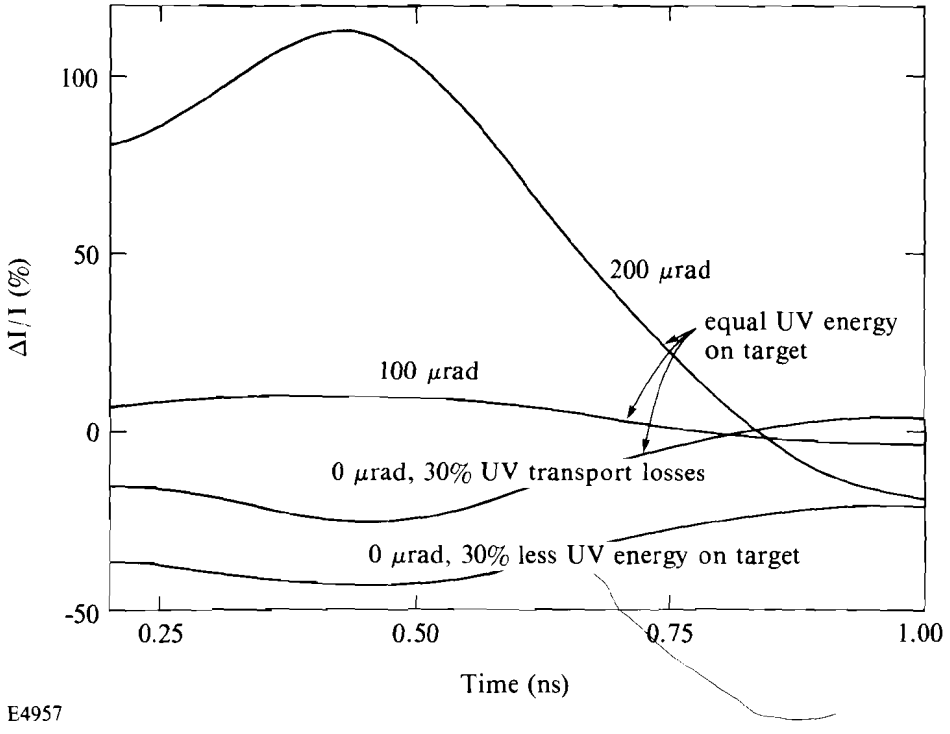

The worst instantaneous on-target intensity imbalance typically arises in the early part of the rising pulse (~1 IR FWHM from the peak of the pulse), at a time when the UV pulse intensity is $\sim 10^{-3}$ of its peak value (see Fig. 37.10). For laser fusion this corresponds to a time when only a small plasma corona surrounds the target, providing for little if any thermal smoothing to alleviate any on-target intensity

fluctuations. Hydrodynamic simulations of laser-fusion experiments have shown that targets nonuniformly irradiated at these early times with these low intensities never recuperate and consequently perform very poorly, even if the illumination uniformity improves later in the pulse.

In summary, careful examination of on-target $\Delta I/I$ values is essential for the success of laser fusion. Fortunately, most of the information concerning the pulse distortion can be obtained from examining the UV pulse shapes over the top one or two decades of intensity, provided that there are no beam-to-beam differences in the IR temporal pulse shapes. This is a relatively safe assumption for lasers using Gaussian temporal pulse shapes that do not operate too close to saturation. For other pulse shapes and lasers operating close to the saturated-gain regime, each beam has to be analyzed separately in the IR and UV unless a UV temporal-pulse diagnostic of very high dynamic range can be deployed on each beam.

OMEGA: Past Energy and Power Balance Performance

OMEGA's past approach to power balance was to achieve the best possible beam-to-beam energy balance. Typical values for the energy balance were 5% to 8% rms with peak-to-valley excursions roughly four times larger. As we have recently discovered, this limit on the energy balance was set by procedures and hardware as will be discussed later.

In order to analyze past OMEGA performance we have selected 70 shots from the high-density campaign, which ended in March 1988, where the selection criterion was an rms beam-energy balance of $\leq 8\%$. For this series of shots we have determined an average rms beam balance of $5\% \pm 1\%$ rms in the IR, with corresponding average peak-to-valley fluctuations of $20\% \pm 5\%$ rms. Interestingly, the average UV-beam-energy balance was only slightly higher at $6\% \pm 1\%$ rms with average peak-to-valley fluctuations of $24\% \pm 7\%$ rms.

Assuming perfectly tuned crystals, the preceding discussion on power balance indicates that the above peak-to-valley beam-energy excursions lead to intensity-dependent power imbalances far beyond the permissible limits for laser fusion. Including the actual frequency-conversion performance (actual/optimum conversion) of the crystals, the resulting peak-to-valley power imbalance for any of the analyzed OMEGA shots certainly exceeds 100% over a significant part of the pulse duration.

It is not possible to reconstruct exactly the values of the power imbalance on any one of these past OMEGA shots, but we can make reasonable estimates for the power imbalance from the known actual conversion efficiencies and the rather incomplete knowledge of pulse durations and shapes in either the IR or the UV. Thus, Fig. 37.11 shows a histogram of the relative conversion efficiencies for all these shots in terms of the differential percentage [(best conversion efficiency − worst)/best]. We note that on average the difference in conversion efficiencies between the best and worst converter is

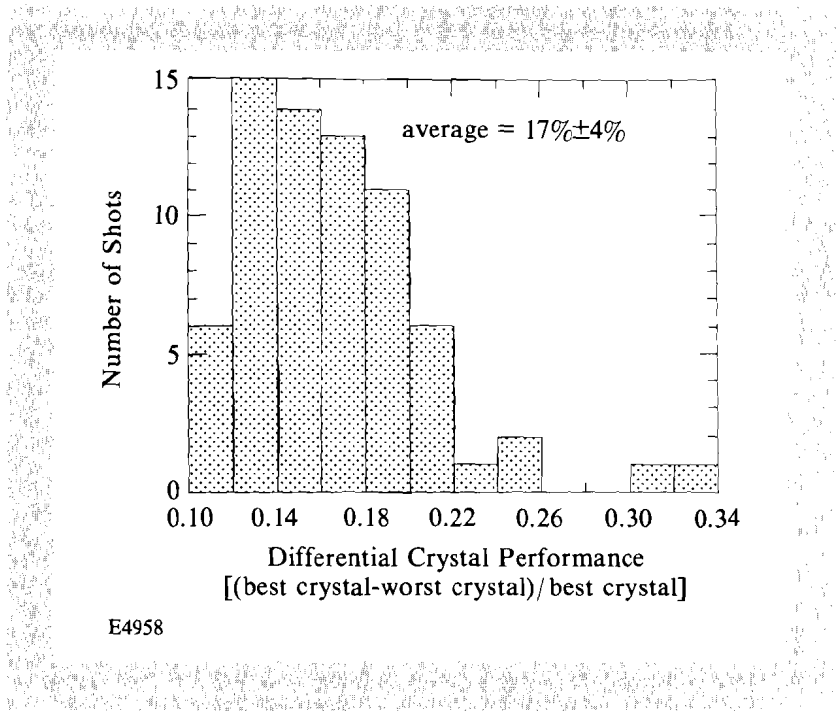

Fig. 37.11
Histogram of the fractional difference between the best and worst frequency converters in the 24-beam OMEGA system for a selection of 70 OMEGA shots of the high-density campaign. The selection criterion was better than 8%-rms beam-energy balance on target corresponding to 6%-average-rms energy balance. Assuming the best crystal to be perfectly tuned, a 20% difference in conversion performance corresponds roughly to 200-μrad detuning of the tripler crystal.

~17%. For 15% of the shots the differences in conversion efficiency were actually in excess of 20%. If we assume that the best converter corresponds essentially to a perfectly tuned crystal, Fig. 37.12 allows us to determine that the equivalent detuning angle for the average worst-performing crystal is 180 μrad$\pm$30 μrad. This angle is well beyond the standard 50-μrad angular-tuning accuracy for any of the crystals of OMEGA; but then it has long been noticed that the actual frequency-conversion performance of the crystals frequently lies 10% to 20% below the expected values. Simple polarization-angle detuning, as shown graphically in Fig. 37.13, could not explain this behavior as the angle of polarization was tuned to better than 1° for all crystals. However, scrutinizing the 70-shot series of OMEGA revealed an underestimate of the amount of depolarization across the beam area. This was caused by depolarization in the outer zones of the last 90-mm rod amplifier along with unrelated problems of input polarizers to the last amplifier, which were frequently removed for reasons of damage. In no case was there a final output polarizer directly preceding the conversion crystals.

Using Fig. 37.13 we can estimate the amount of depolarization, i.e., the amount of energy in the wrong (uncorrectable) polarization, needed to account for a 20% drop in conversion efficiency. Assuming the depolarization is spread uniformly across the beam area, a 3° rotation of the plane of polarization or approximately 0.3% (= $\sin^2 3°$) of the energy in the wrong state of polarization would suffice to account for the 20% decrease in frequency conversion. An alternative estimate is obtained if we concentrate the depolarization in the outermost 13% of the beam radius (25% of the beam area); in this case 4% of the beam energy in this area (polarization angle of ~24° instead of the optimum 35°) would be required to explain a 20% decrease in overall third-

Fig. 37.12
Angular tuning curves for the energy conversion to the third harmonic for different IR input intensities to the crystals (two 1.6-cm-thick KDP crystals).

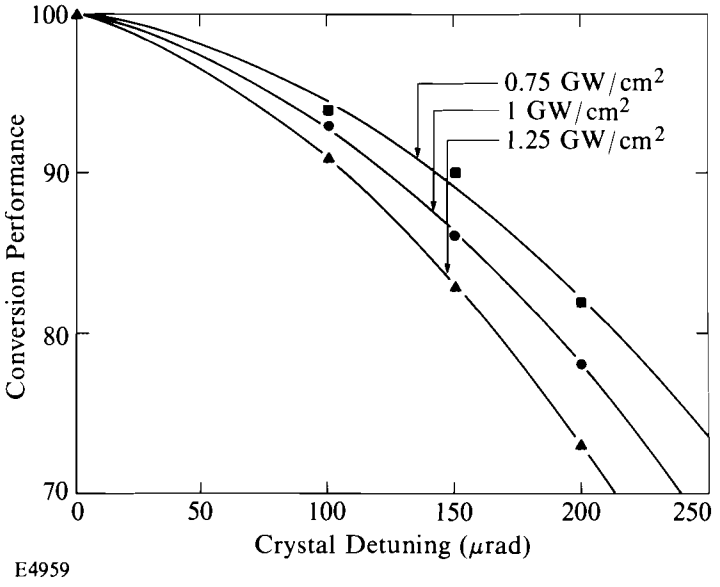

Fig. 37.13
Polarization-tuning curve for the third-harmonic energy-conversion efficiency at an IR input intensity to the conversion crystals of 1 GW/cm^2 (1.6-cm-thick KDP crystals). Also shown are the residual green at the output of the conversion crystals and the change in FWHM of the UV pulse as a function of the angle of the input polarization relative to the *e* axis of the frequency doubler. (Note that the UV pulse shape is a distorted Gaussian with the distortion increasing rapidly as the polarization angle is detuned from its optimum angle near 35°.)

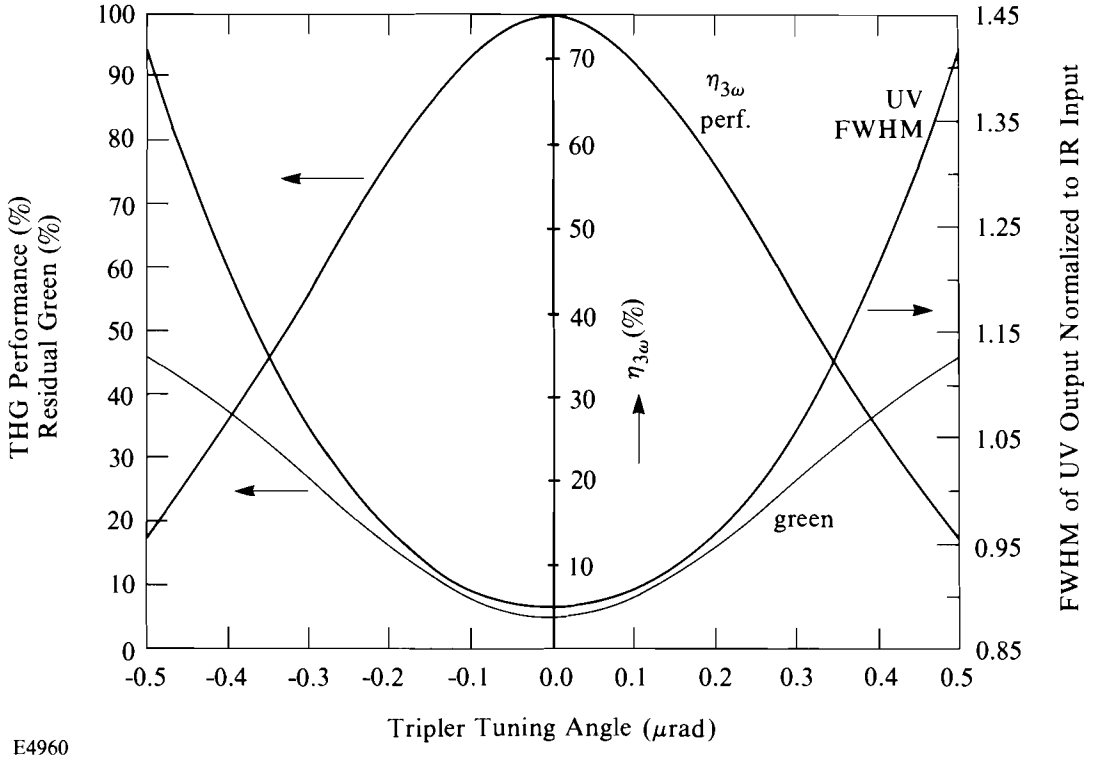

harmonic frequency conversion. If the depolarization were corrected through the introduction of a polarizer in the beam in front of the conversion crystals, the energy losses for these two model cases would be a negligible 0.3 and 1% overall!

The energy balance on OMEGA's 24 beams is carried out by manually rotating various half-wave and quarter-wave plates in front of polarization-sensitive beam splitters. The accuracy of these adjustments is now estimated to be $\sim 1°$ on average. Analysis of all the splitting areas has shown that the beam splitters do not behave like perfect polarizers but cause the output polarization from each beam splitter to be rotated significantly, requiring compensatory movements of subsequent wave plates. In addition, differential phase shifts between the "*s*" and "*p*" components lead to some ellipticity of the polarization after each beam splitter resulting in variable losses on subsequent polarizers in the beam. Imperfect knowledge of all these parameters and manual-setting accuracy of the 23 splitting wave plates in OMEGA made it impossible to achieve better than $\sim 5\%$-rms beam-energy balance as is easily verified through error propagation analysis.

To obtain a good estimate of the ultimate energy balance possible on OMEGA we have carried out a series of laser shots during which all laser parameters were held constant and a strict 30-min shot interval was maintained. The results are shown in Fig. 37.14 where the rms energy fluctuations for each beam are plotted along with their corresponding peak-to-valley excursions. We note that a 1%- to

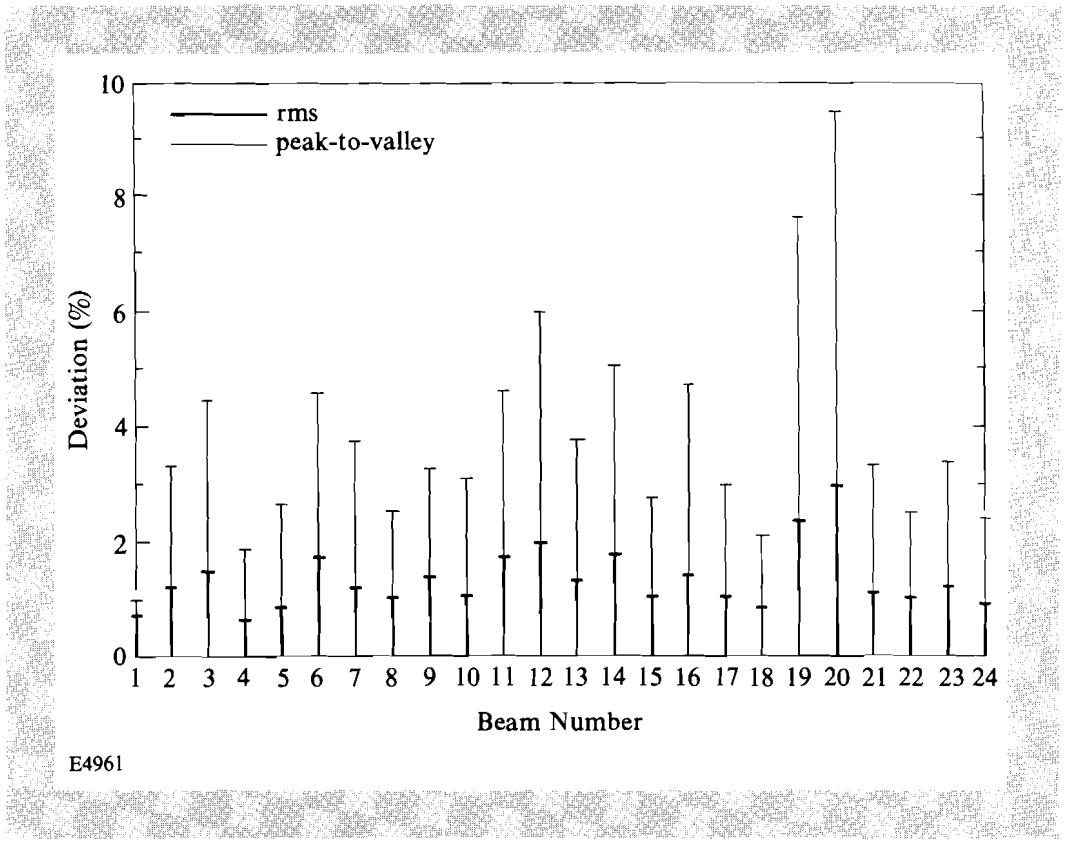

Fig. 37.14
Reproducibility of the beam energies in each of the 24 OMEGA beams for eight successive shots under identical operating conditions. No selection was made for misfires of individual flash lamps, which can probably account for some of the larger excursions (e.g., beam 20). The two error bars for each beam correspond to the percent rms and peak-to-valley fluctuations in each beam. From this data we estimate that the present limit to the beam balance lies around 1% to 1.5% rms or 4% to 5% peak-to-valley.

1.5%-rms beam-energy balance (3% to 4% peak-to-valley) should be obtainable on OMEGA. (The calibration accuracy and repeatability of the calorimetry system lies between 0.5% and 1%. Very stringent and frequent verification and control of the calorimetry as well as all the optics between the point of calorimetry and the target are required in order to maintain credible beam balance measurements.) However, such beam-energy-balance performance clearly cannot be obtained with past OMEGA practices.

OMEGA Improvements

1. Crystal Conversion

From the above discussion we concluded that the most important improvement regarding power balance comes from proper resetting of the polarization prior to frequency conversion. To this end we have now installed output polarizers after each of the final 90-mm rod amplifiers. The loss on these dielectric linear polarizers is expected to be mostly dominated by the residual 3% to 5% reflection of the transmitted "*p*" polarized light. We have also implemented improved methods for ascertaining proper tuning of the crystals through computerized performance checks. Our latest results indicate that it is now possible to keep the performance of the conversion crystals to within 2% rms (8% peak-to-valley) of the calculated optimum performance (further improvements are still possible). This implies that at present the worst-performing crystal could be detuned by ~ 100 μrad, or that the near-field intensity distributions of the various beams at the crystals cause the energy-conversion efficiencies to vary by up to 8%. Our present results are most likely due to a combination of both effects and the effects due to slight variations in crystal thicknesses.

2. Beam-Energy Balance

To improve the beam-energy balance on OMEGA we have implemented a system of photodiodes at the output of OMEGA that can monitor the oscillator output energy at that location. When these diode signals are normalized to high-energy, full-system shots, balancing the output energies of all 24 beams can proceed using only the oscillator. Furthermore, installation of motorized splitter wave plates allows the movement of all wave plates with accuracies of $\sim 0.05°$, well beyond the requirements. This system is now operational and yields 2%- to 3%-rms beam-energy balance within two iterations. A reduction of this value to 1% to 1.5% rms is possible provided failures of individual flash lamps are properly identified and eliminated.

Summary

The time-varying illumination nonuniformity caused by power imbalance has been identified as a problem on the OMEGA laser system. Correction of power imbalance required the insertion of output polarizers in each beam and the implementation of computer-controlled motorized splitter wave plates throughout the system. With these modifications in place, we are able to control the third-harmonic conversion in each beam to within 2% of the calculated optimum and can routinely maintain beam-energy balance at 2% to 3% rms.

Appendix

During the course of analysis of the data presented here we have found some convenient analytic approximations to a number of second- and third-harmonic energy conversion and tuning curves. This has significantly facilitated the tuning of the 24 pairs of conversion crystals in OMEGA and may help others doing research in the field of frequency conversion. These analytic approximations were based on computer calculations (MIXER[5]) for the harmonic conversion assuming a Gaussian temporal pulse shape and a top-hat spatial-intensity profile incident on the conversion crystals.

Figure 37.15 shows the calculated points and the analytic approximations for the second- and third-harmonic energy-conversion curves, while Figs. 37.16 and 37.17 show the second- and third-harmonic tuning curves and their best-fit Gaussian approximations. The Gaussian fits are accurate down to $<10\%$ of the peak of the conversion curves. The half-widths of the Gaussian are intensity dependent as shown in Fig. 37.18. Unfortunately, no satisfactory fits were found for the polarization tuning curves, with the best results shown in Fig. 37.19. Figures 37.16, 37.17, and 37.19 are all normalized to unity corresponding to our earlier definition of crystal performance. The actual value of the conversion at the peak of the tuning curves can be read from Fig. 37.15. The abscissae in these figures have been adapted to conveniently reflect the applicable scaling laws for the conversion efficiencies. The third-harmonic conversion and tuning curves assume equal crystal thicknesses for the second-harmonic and third-harmonic (MIXER) crystals.

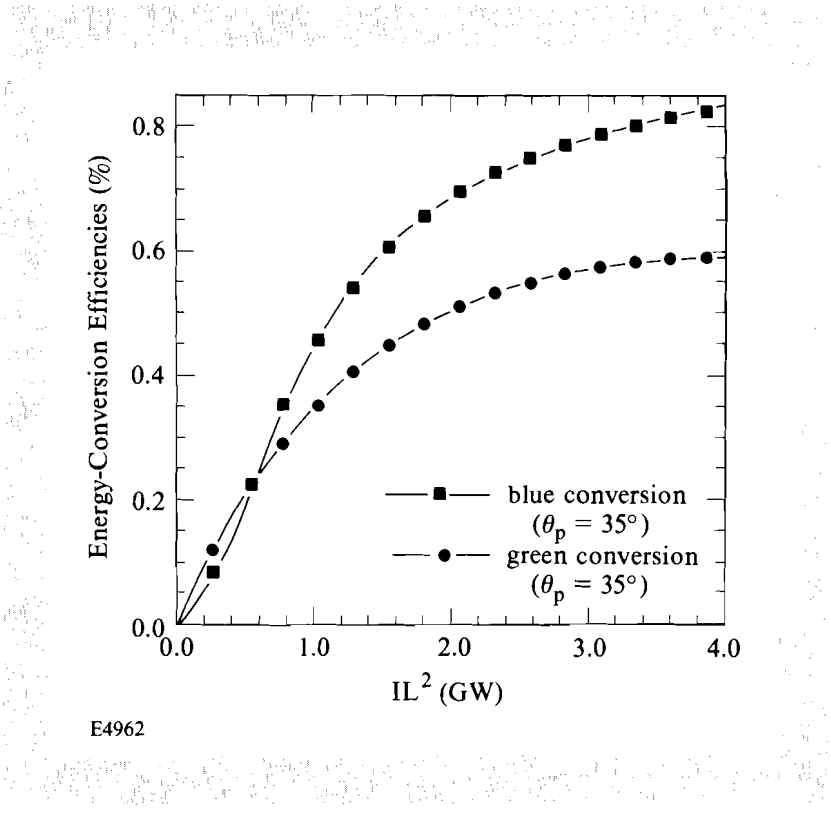

Fig. 37.15
Second- and third-harmonic energy-conversion curves for Gaussian temporal pulses and top-hat spatial intensity profiles as calculated by the simulation code MIXER[5] and their analytical best-fits. $\eta_{sh} = 82.94\ [1 - \exp(-0.624x + 0.0785x^2)]$; $\eta_{th} = 85.91\ [1 - \exp(-1.41x^2 + 0.869x^3 - 0.223x^4 + 0.0202x^5)]$, where $x = IL^2$ in GW, I is the IR intensity at the crystal input face, and L is the length of each of the two conversion crystals. The choice of IL^2 for the abscissa reflects the scaling law for the conversion efficiencies. The polarization at the input to the crystals is assumed to be at 35° with respect to the e axis of the doubler.

Fig. 37.16
Second-harmonic tuning curves for the energy-conversion efficiency as calculated by the simulation code MIXER[5] for Gaussian temporal pulses and top-hat spatial-intensity profiles. The x axis reflects the θ_L scaling law for the conversion efficiency. The best-fit curves are Gaussians [$\eta_{sh} = \exp(-A_{sh}\, x^2)$, $x = \theta_L$ in μrad.cm], with the intensity-dependent parameter A_{sh} given in Fig. 37.18.

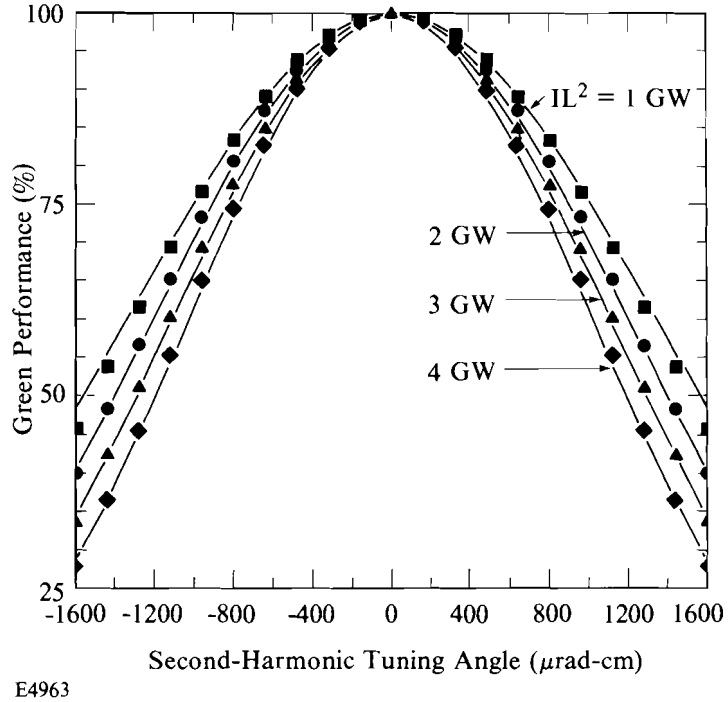

E4963

Fig. 37.17
Third-harmonic tuning curves for the energy-conversion efficiency as calculated by the simulation code MIXER[5] for Gaussian temporal pulses and top-hat spatial-intensity profiles. The x axis reflects the θ_L scaling law for the conversion efficiency. The best fit curves are Gaussians [$\eta_{th} = \exp(-A_{th}\, x^2)$, $x = \theta_L$ in μrad.cm], with the intensity-dependent parameter A_{th} given in Fig. 37.18.

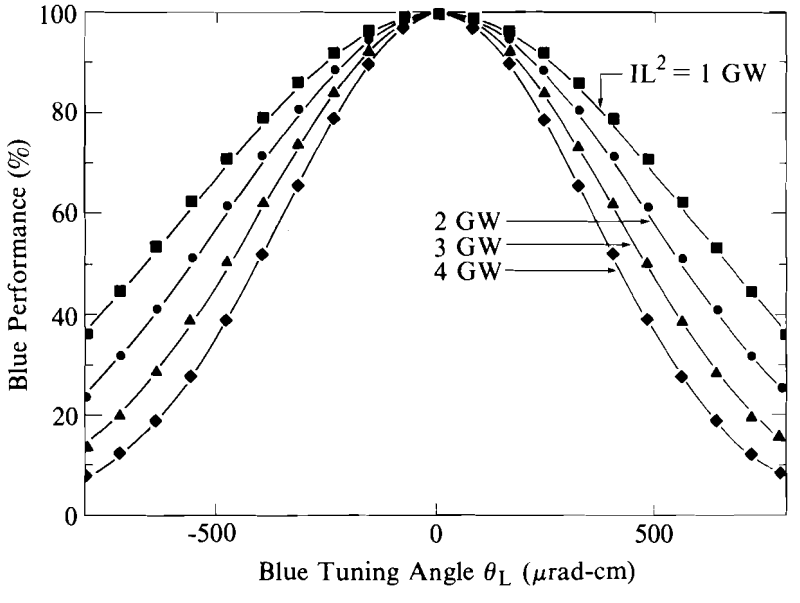

E4964

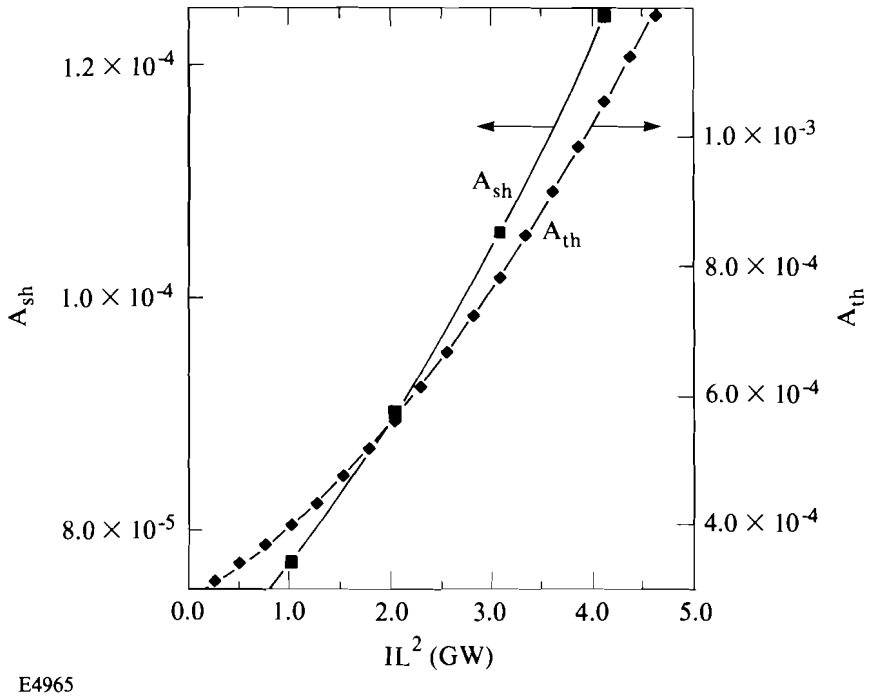

Fig. 37.18
Intensity dependence of the parameter A ($1/e$-widths = $1/\sqrt{A}$) of the Gaussian best fits for the second- and third-harmonic tuning curves of Figs. 37.16 and 37.17. $A_{sh} = 3.38 \times 10^{-6}x^2 + 8.59 \times 10^{-6}x + 2.62 \times 10^{-5}$, $A_{th} = 6.09 \times 10^{-4}x^2 + 8.93 \times 10^{-4}x + 1.11 \times 10^{-4}$, where $x = IL^2$ in GW as in Fig. 37.15.

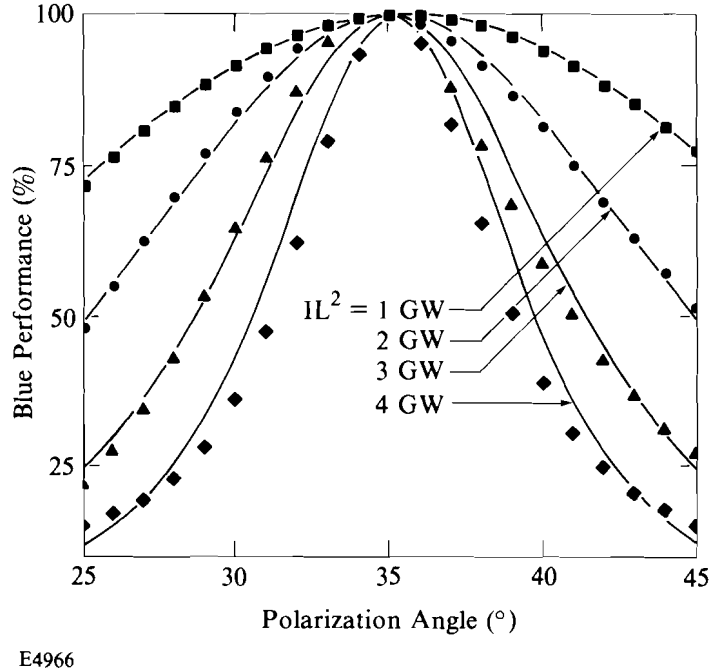

Fig. 37.19
Polarization-tuning curves for third-harmonic generation as calculated by the simulation code MIXER[5] for Gaussian temporal pulses and top-hat spatial-intensity profiles. The fitted curves shown in this figure are relatively poor fits but they are useful in certain applications. The analytic form of the best fits shown is $\eta_{th} = \exp(1/\{1+[(x-35)/x_p]^2\})$, where $x_p = 2.47x^2 - 21.5x + 57.5$, $x = IL^2$ in GW.

6. R. S. Craxton, S. D. Jacobs, J. E. Rizzo and R. Boni, *IEEE J. Quantum Electron.* **QE-17**, 1782 (1981).

7. M. Born and E. Wolf, *Principles of Optics*, 6th ed. (Pergamon Press, New York, 1980), pp. 403-406.

8. Ref. 7, pp. 436–437.

9. R. C. Eckardt and J. Reintjes, *IEEE Journal of Quantum Electron.* **QE-20**, 1178 (1984).

1.D Broadband Phase Conversion Using SSD

The propagation, amplification, and frequency conversion of broadband light in the OMEGA laser requires several system modifications. Figure 37.26 schematically represents the evolution of a laser beam throughout the system. The implementation of SSD in the OMEGA laser system includes the constraints that the group-velocity delay, electro-optic phase modulation, and angular dispersion be compatible with the current design. The majority of modifications are contained within the driver line where the smaller beam size and reduced energy level allow greater design flexibility. Phase conversion with distributed phase plates occurs at the end of each of the beamlines.

Broadband-Phase-Conversion Implementation

Laser beam parameters are best exploited early in a multibeam system, where the modifications are made only once. The driver line is easily modified to include new optical elements, holographic diffraction gratings, and a microwave phase modulator. Figure 37.27 illustrates the various changes that have been made to the OMEGA driver line. Two sets of kinematic mirror pairs are inserted into the straight beam path; one within the predriver zoom-relay and one just before the final 64-mm laser amplifier. In the predriver, various optical elements are situated between the kinematic mirrors to achieve lateral beam delay and bandwidth broadening. The output of the oscillator is spatially filtered, collimated, and expanded by a 5X keplerian telescope to produce a beam diameter of approximately 58 mm. Beam polarization is converted to linear "*S*" for efficient transfer through a three-element arrangement that contains one polarizer, a 57° transmission grating, and a second polarizer. The grating produces a lateral beam delay that is similar to the pulse width of the oscillator (650-ps FWHM). The associated angular spectral dispersion is ineffective since the oscillator is a Fourier-transform-limited narrow-band pulse. A second 5X telescope compresses the beam back to the original diameter. With an auxiliary positive lens, the beam is returned

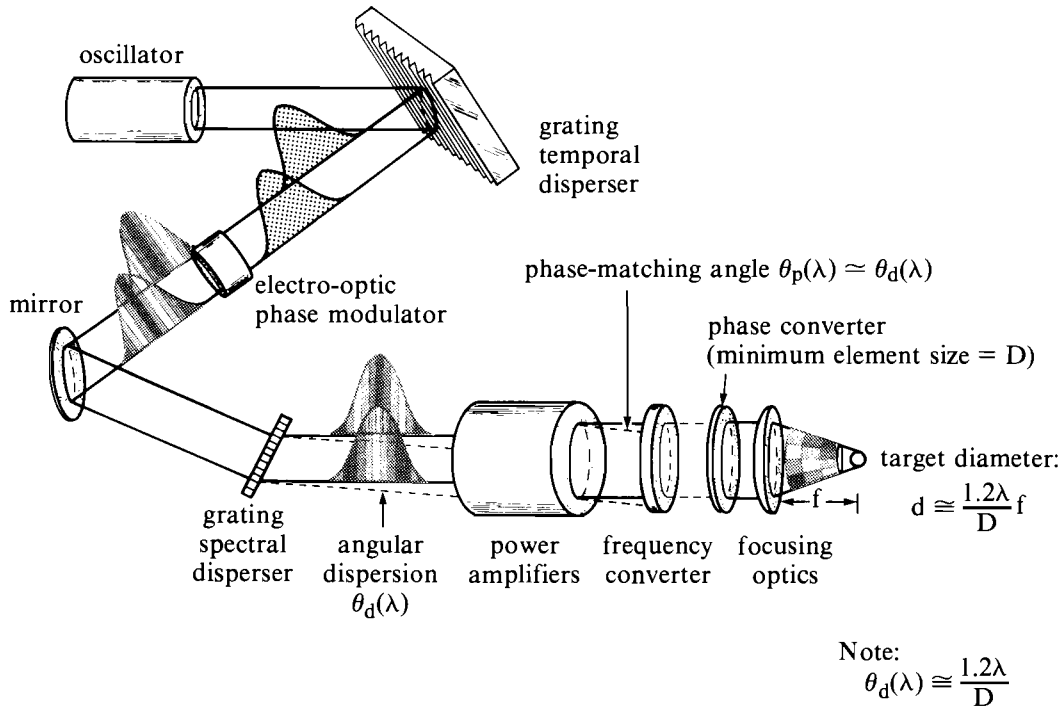

Fig. 37.26
A new beam-smoothing technique—smoothing by spectral dispersion (SSD)—provides uniform target illumination for frequency-converted laser systems. The key technologies required for SSD are high-power holographic gratings, microwave phase modulators, and distributed phase plates.

to the zoom assembly with the correct numerical aperture for injection into the amplifier chain. A microwave-cavity phase modulator is positioned between the auxiliary lens and the zoom lens. Axial translation of the modulator allows the phase modulation to be introduced either in the near-field or the far-field. The latter is desired when electric-field nonuniformities or optical inhomogeneities exist within the electro-optic crystal. Free-propagation from the far-field can eliminate certain phase nonuniformities and spatially average the induced bandwidth. Air breakdown and crystal damage are prevented by limiting the value of the intermediate numerical apertures.

Lateral beam delay causes a certain amount of whole-beam nonuniformity in the near-field intensity distribution. In addition, a multifaceted grating is a source of edge diffraction. Together, these two sources of beam diffraction produce a deterioration of the far-field intensity distribution. Although these effects are well masked during phase conversion with distributed phase plates, the intermediate foci at the spatial filter pinholes contain an unwanted energy spread. For this reason, the spatial filter pinholes are enlarged throughout the driver line to prevent pinhole closure and near-field modulation.

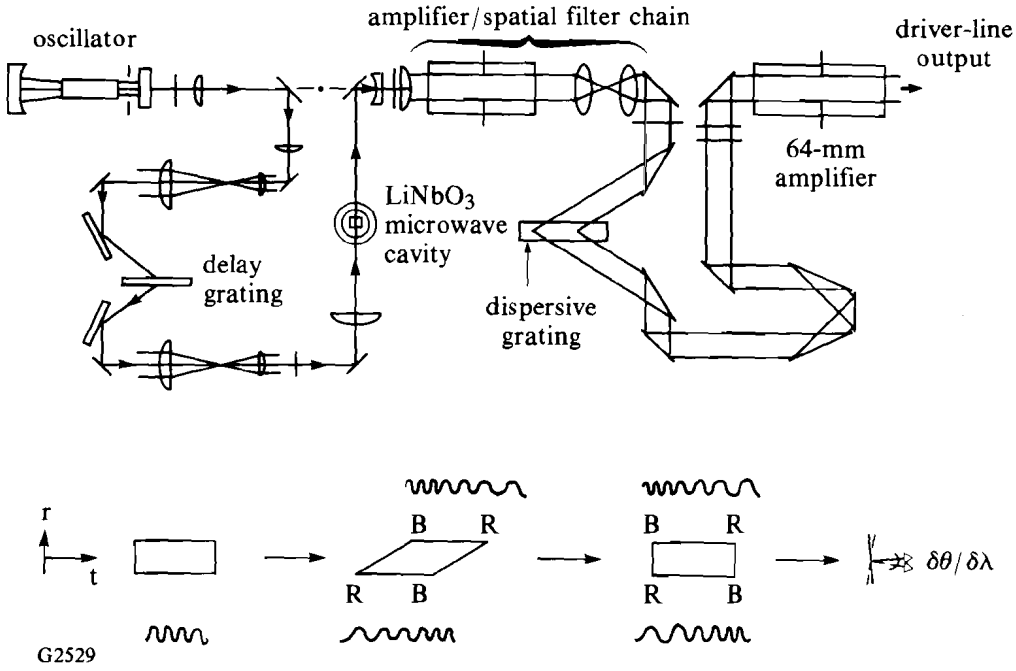

Fig. 37.27
Implementation of SSD on the OMEGA laser involves modification of only the driver line. Early in the driver line, one diffraction grating and the microwave phase modulator are appropriately positioned into an auxiliary beam path. The second grating is placed at the end of the driver line. Beam shaping, beam orientation, and polarization optical elements are included in both arms to achieve proper coupling of the beam parameters.

Removal of the lateral beam delay and addition of angular spectral dispersion are accomplished at the output of the driver line, just prior to the final 64-mm laser amplifier. As in the predriver, a polarizer-grating-polarizer arrangement is used to accommodate the relatively large angle of diffraction. The first diffraction grating is located at the hard-aperture image plane. The proper coupling of a Gaussian beam envelope with the high radial-gain profile from a series of rod amplifiers is preserved. Envelope distortion caused by diffraction is reduced with this choice of imaging. The second grating is located in a plane that is subsequently image relayed to a position outside the individual amplifiers throughout the 24 beamlines. Time-varying beam shifting occurs at these nonimage planes. It is anticipated that lateral beam shifting, on the spatial scale consistent with the peak growth for nonlinear beam-breakup, will offer a new mechanism for beam smoothing. Instantaneous nonlinear phase could be distributed over a spatial dimension to reduce the time-integrated intensity modulation below that which would occur if allowed to be spatially stationary.

As the beam propagates through the amplifier chain of the driver line, it has a constant lateral time delay and a time-varying spectrum

until it reaches the second grating. The angular spectral dispersion for this grating is set equal in magnitude but opposite in sign to the first grating to compensate for the lateral beam delay. This compensation restores the beam shape and creates a one-dimensional spectral gradient that also varies in time according to the modulation frequency of the microwave source. The two gratings must be oriented to provide the correct sign of angular spectral dispersion to the frequency-conversion crystals for proper phase matching of the individual spectral components. Angular demagnification between the driver line and the frequency-conversion cells is accounted for by over-dispersing the spectrum at the driver-line location.

The final step in broadband phase conversion is the propagation of broadband frequency-converted laser light through a distributed phase plate (DPP).[1] The time-varying spectral spread over one beam dimension samples the individual elements of the phase plates, thus producing a time-varying interference pattern. In addition, approximately 200 μrad of angular dispersion reaches the target chamber for a 2-Å spectral width. This translates to about a 10-mm ellipticity over a 165-mm-diameter beam for the extreme spectral components. Every point on the beam undergoes about a 10-mm sweep across the DPP at the rate of color modulation. The quickly varying interference pattern that results from this source of DPP sampling is another aspect of beam smoothing at the target plane.

Microwave Phase Modulator

The central device within the SSD system is a microwave phase modulator used to impress a time-varying bandwidth on the laser beam. Illustrated in Fig. 37.28, a resonant microwave cavity contains a rectangular crystal of lithium niobate. In order to achieve the modulation index required for SSD, between 4π to 6π, voltages of the order of tens of thousands of volts are required. A waveguide or stripline approach with matched impedance geometry would require a high level of RF power (2 MW) to achieve 10 kV across a crystal. Since this is an excessively high power level, an alternative solution is required. A resonant cavity with a sufficiently high "Q" can generate high voltages for low-to-medium input power (2 kW).

The "Q" factor reduces the required input power in the following way. An RF voltage V, at the resonant frequency of the cavity, is applied with magnetic field coupling. For a cavity with a given Q, then after Q/π cycles of the microwave applied to the cavity, the voltage inside the cavity is $Q \times V$. At the frequencies of interest, in the 2- to 3-GHz region, it is straightforward to build cavities with Q's of several thousand or several tens of thousands. With coupling efficiencies of several percent into the desired mode in the cavity, several tens of thousands of volts can be reached in several microseconds with power inputs of less than 2 to 3 kW.

In practice, the resonant frequency of the cavity depends heavily on the geometry of the crystal because of the very high dielectric constant of lithium niobate (23 at 2 GHz). This very high relative dielectric constant causes the lithium niobate to overwhelm the rest of the

$$E(t) = e^{(i\omega t + i\eta \sin\omega_o t)} = e^{i\omega t} \sum_{-\infty}^{\infty} J_n(\eta) e^{in\omega_o t}$$

$\omega_o = 2\pi\nu_o$
ν_o - modulation frequency
η = modulation index
$n_{max} \sim \eta$

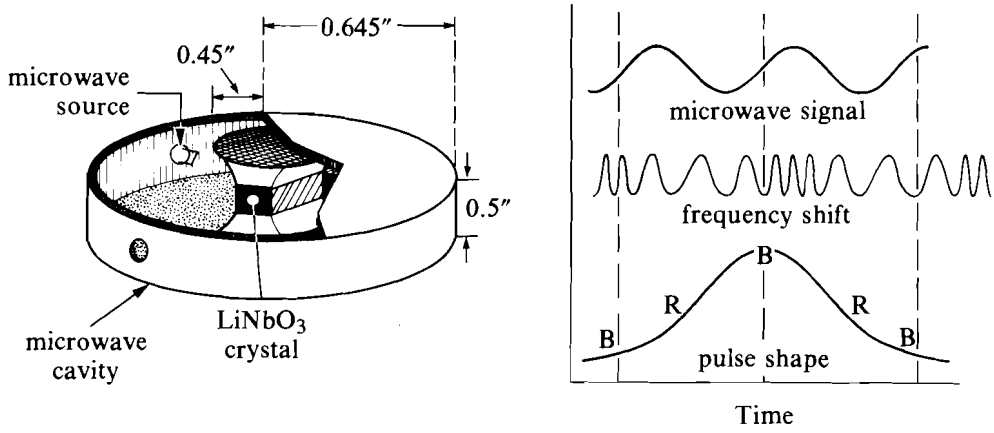

Fig. 37.28
Electro-optic phase modulation is the source of spectral broadening. The phase modulator consists of a resonant radial-line cavity containing a crystal of lithium niobate. The microwaves are coupled-in through the magnetic field, producing electric-field amplification at the location of the crystal. Both the electric field and light polarization orient along the z axis of the crystal (perpendicular to the disc) for maximum phase modulation.

capacitive elements of the cavity and leads to a resonance much lower than that of the empty cavity.

Two specific cavity designs were tried in this experiment. Both were re-entrant designs where the crystal was placed in the gap between the re-entrant capacitive portion of the cavity and the ground plane of the cavity. Both coaxial resonators and radial-line resonators were designed and built. Because of its smaller dimensions, the radial-line-resonator approach was finally chosen. Without the crystal in the cavity, the resonant frequency was >3 GHz (the limit of our measuring equipment). With the crystal centered under the re-entrant post of the cavity, the frequency was lowered to 2.46 GHz. The Q, as measured to be in half-power points of the resonant frequency, was measured to be in excess of 10,000. Power was fed into the cavity through a sidewall-mounted loop probe of very small dimensions so as not to spoil the Q. The probe size was determined through a trade-off

between Q and coupling efficiency. With such high Q's available, it was advantageous to use a very small probe with its attendant low coupling efficiency.

The RF power supply used to drive the cavity was a mechanically tuned, grid-pulsed, lighthouse tube cavity oscillator, which was capable of generating up to 5-kW pulses in 10-μs pulses. With Q's of the order of several thousand, complete voltage build-up occurred in the cavity (five e-folding times) in less than the pulse width. This allowed for some jitter in the rest of the timing electronics that synchronized the microwave pulser to the laser system.

Lithium niobate is oriented within the cavity with the Z-axis parallel to the re-entrant post axis. Phase modulation is achieved by polarizing the light parallel to these axes. The bandwidth is characterized with a Fabry-Perot interferometer. Figure 37.29 shows the spectral fringes before and after phase modulation. Bandwidth broadening is observed when the individual rings widen. In excess of 2 Å of bandwidth is reproducibly achieved for laser shots on the OMEGA laser.

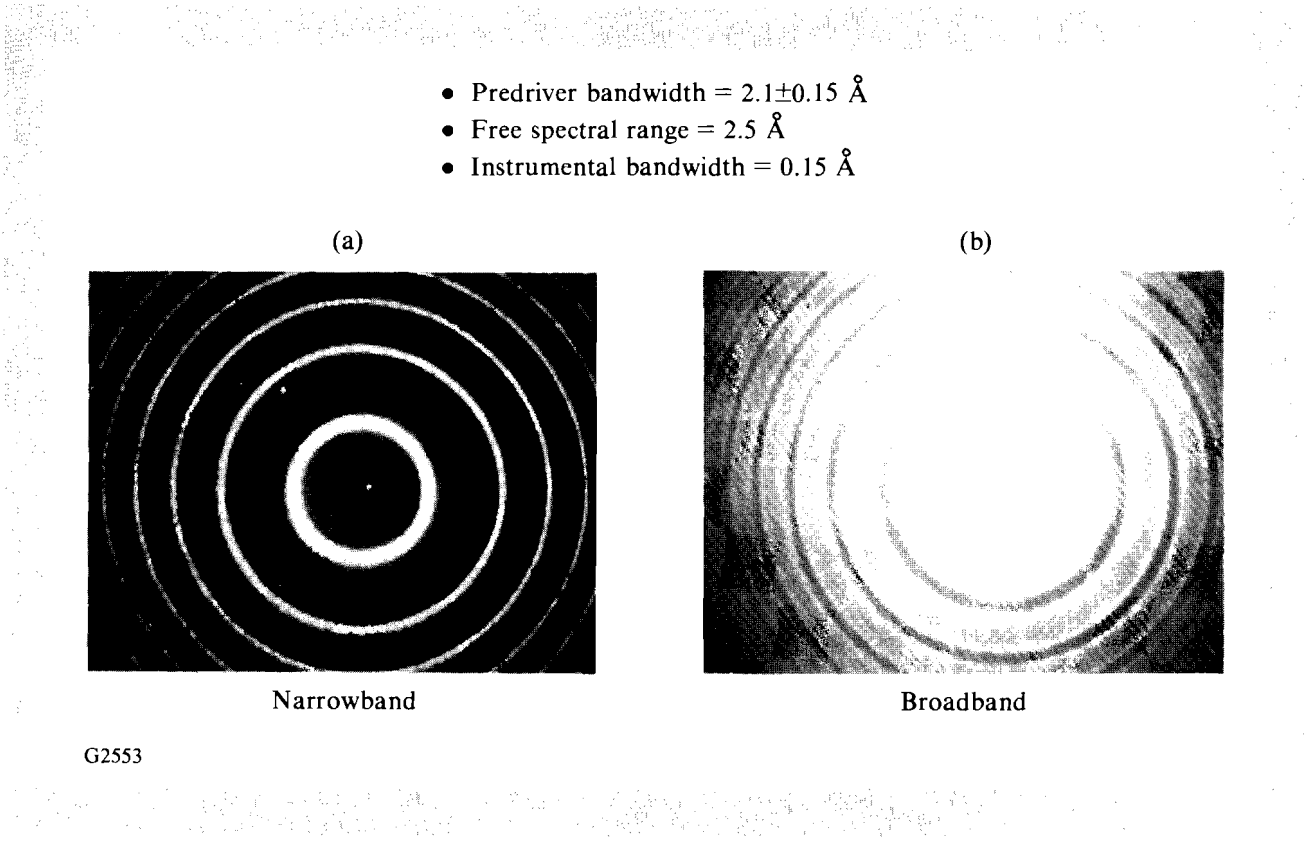

Fig. 37.29
Spectral measurements are made with a Fabry-Perot interferometer. Narrow-band radiation is characterized by narrow concentric rings whose separation represents the free spectral range. Bandwidth broadening is observed when the individual rings widen. A free spectral range of 2.5 Å indicates a bandwidth of ~2 Å for the data shown here.

High-Power Holographic Gratings

The base-line design, for the implementation of the simplified version of SSD, requires a group-velocity delay of about 600 ps both at the beginning and at the end of the driver line. An angular spectral dispersion of about 300 μrad/Å at the output of the driver line is also required. Diffraction gratings can provide the required delay and dispersion, but there are additional performance requirements that must be fulfilled. The damage threshold of the grating at the end of the driver line must be >300 mJ/cm^2 at a pulse width of 650 ps (FWHM) for it to survive in a position just prior to the final 64-mm amplifier. The projected clear aperture of the grating must be slightly larger than the beam diameter. At an incident angle of 57° and a beam diameter of 58 mm the required grating dimension is about 130 mm. In addition, the grating must have a diffraction efficiency of $>80\%$ while providing the correct angular dispersion.

Diffraction gratings can operate either in the reflection or transmission mode. Typically, a diffraction grating is characterized as a surface or volume and an amplitude or phase grating. A schematic of the surface-phase grating is shown in Fig. 37.30. A periodic, sinusoidal structure gives rise to diffraction according to the general grating equation,[2]

$$d\,[\sin(i) - \sin(\theta)] = m\lambda,$$

where d is the grating spacing, i is the angle of incidence, θ is the angle of diffraction, m is the diffraction order, and λ is the wavelength of light. The rate of change of the angle of diffraction with respect to wavelength, at a constant angle of incidence, is the definition of angular dispersion and is given by

$$\frac{\partial\theta}{\partial\lambda} = \frac{1}{d\cos(\theta)} .$$

The group-velocity path difference gives rise to the lateral-beam delay that is related to the beam diameter and the angle of incidence by

$$\Delta\tau = \frac{D[\tan(i) + \tan(\theta)]}{c} .$$

Table 37.I summarizes the diffraction grating design for the application of SSD in the OMEGA laser system.

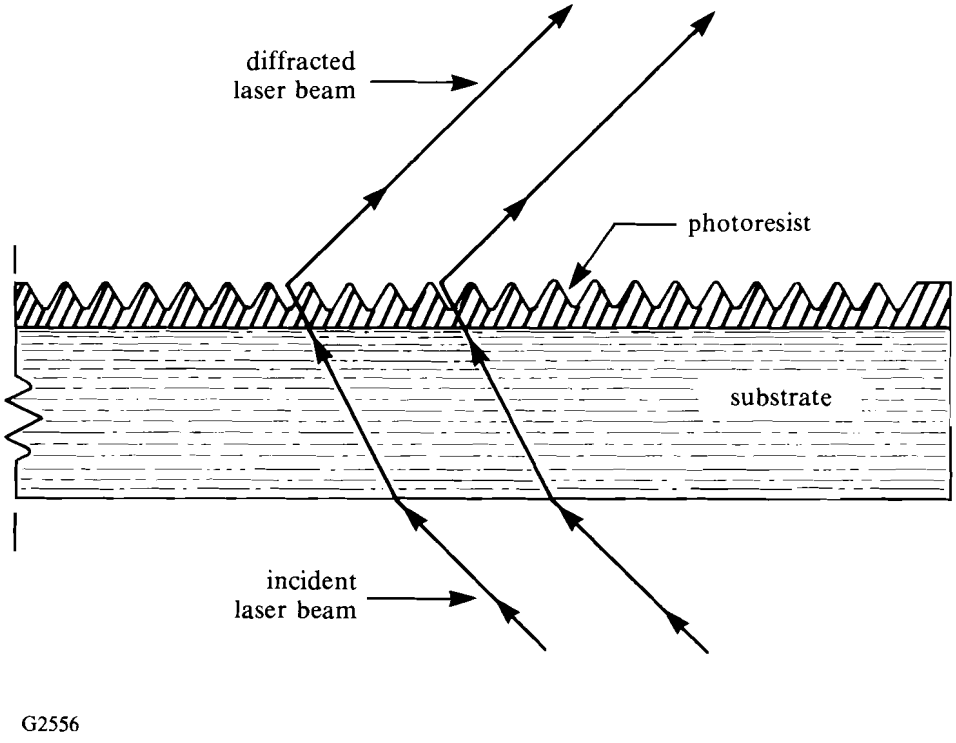

Fig. 37.30
Holographic diffraction gratings used for SSD on OMEGA consist of a surface-relief layer of photoresist. High-power, high-efficiency gratings have for the first time been demonstrated at large apertures. Holotek, Ltd. (Rochester, NY) participated in the project by providing the holographic gratings.

Table 37.I
Diffraction grating design

Grating structure (d)	628 nm
Incident angle (i)	57°
Diffraction angle (θ)	57°
Order (m)	1
Wavelength	1054 nm
Angular dispersion (driver line)	292 μrad/Å
Angular dispersion (conversion cells)	100 μrad/Å
Lateral delay	585 ps

G2554

Several candidate materials have been investigated for use as high-power diffraction gratings.[3] Ruled and holographic reflection gratings are generally overcoated with a metallic film to obtain high diffraction efficiency. However, metallic films intrinsically have a low damage threshold and cannot be used in high-power applications. Dichromated-gelatin, volume holograms have occasionally exhibited a high damage threshold, but this material is environmentally unstable and has not been scaled to a large-aperture, highly efficient optical component. There are several synthetic photopolymers that recently have been made available; however, very little is known about them with respect to high-power applications. Positive photoresist, the same material used in the manufacture of distributed phase plates, is currently the only successful material candidate. Holographic gratings made from photoresist are surface-relief phase gratings and therefore are used in the transmission mode.

High damage thresholds have been demonstrated for positive-photoresist master holograms that are fabricated at Holotek Ltd.[4] An average 1-on-1 damage threshold of 0.8 J/cm^2 had made photoresist an attractive material early in the development stages. However, continued research revealed a hardening process in which fluence ramping over several laser shots increased the damage threshold. The N-on-1 damage threshold varied between 1.0 and 6.0 J/cm^2 at a pulse width of 650 ps and a wavelength of 1054 nm. Damage sites could not be produced at maximum system energy. As a result, two orders of magnitude greater fluence can be achieved when using diffraction gratings with high-power radiation.

Surface-relief gratings made from photoresist provide several other design advantages. Transmission diffraction efficiencies of $>85\%$ at $\lambda = 1054$ nm at $i = 57°$ have been achieved with superior stability and very low noise. Furthermore, surface relief gratings possess a very broad angular response, providing alignment insensitivity and flexibility in selecting an angular spectral dispersion. Figure 37.31 shows the diffraction efficiency as a function of the incident angle for a grating that is sandwiched between antireflection-coated substrates. A full 10° angular range is available at negligible loss in efficiency. This performance applies only to "S" polarization, i.e., electric-field oscillation normal to the plane of incidence. Performance for "P" polarization can be increased, but only at the expense of S-polarization performance. Normally, obtaining high S-polarization efficiency is tantamount to achieving good polarization contrast.

In addition to beam smoothing by means of SSD, there are many applications for high-power diffraction gratings within a laser system. Gratings can be used as medium-contrast polarizers, multiwavelength beam splitters, spectroscopic elements, dispersive elements in an oscillator cavity, imaging elements, and spectral deflectors. Efficient frequency conversion, without requiring an angular dispersion to reach the target, can be achieved by placing diffraction gratings before and after the crystals. Another example involves the use of high-power gratings as the final optical element in several pulse-compression schemes.[5]

Further development of the surface-relief holographic grating, using either photoresist or photopolymer materials, can lead to higher diffraction efficiency at a larger clear aperture. Increasing the clear aperture of the grating is an important aspect of the current grating research. Size limitations depend primarily upon the deposition uniformity of the resist and the power and profile of the recording beams. Proper choice of the beam profiles can lead to successful continuous-wave or pulsed plane-wave holographic recording.[6]

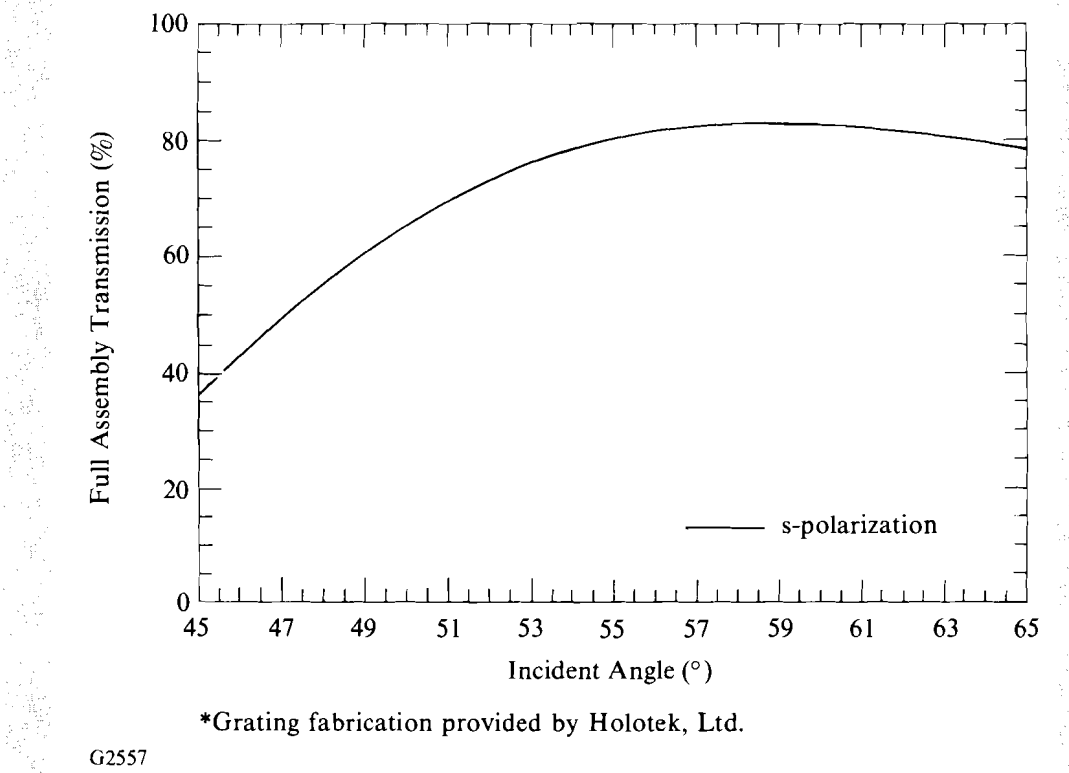

Fig. 37.31
The high-efficiency holographic gratings, provided by Holotek, Ltd., exhibit a broad angular response. The surface of the grating is sandwiched between two AR-coated glass plates for protection. The above curve shows a relatively constant diffraction efficiency for the assembly over 55°-65°.

Broadband Harmonic Conversion

In order to demonstrate that angular dispersion provides a means of frequency tripling broadband light, an experiment was performed using the setup illustrated in Fig. 37.32. The output of a Nd:YLF cw mode-locked laser was sent through 800 m of single-mode optical fiber to produce spectral broadening through self-phase modulation. Laser pulses exit the fiber at rate of 10^8 pulses per second, each pulse having a pulse width of 100 ps and a spectral bandwidth of ~25 Å. Due to the positive group-velocity dispersion in the fiber, the frequency components are dispersed in time in such a way that the

long wavelengths emerge from the fiber ahead of the shorter wavelengths. A single pulse from the fiber was then amplified in a Nd:glass regenerative amplifier. The amplifier cavity included a 50% reflecting-output coupler, producing a 15-pulse envelope that contained ~7 mJ. The entire pulse train was used for the broadband frequency-tripling experiment. The experiment consisted of two configurations: one with and one without angular spectral dispersion.

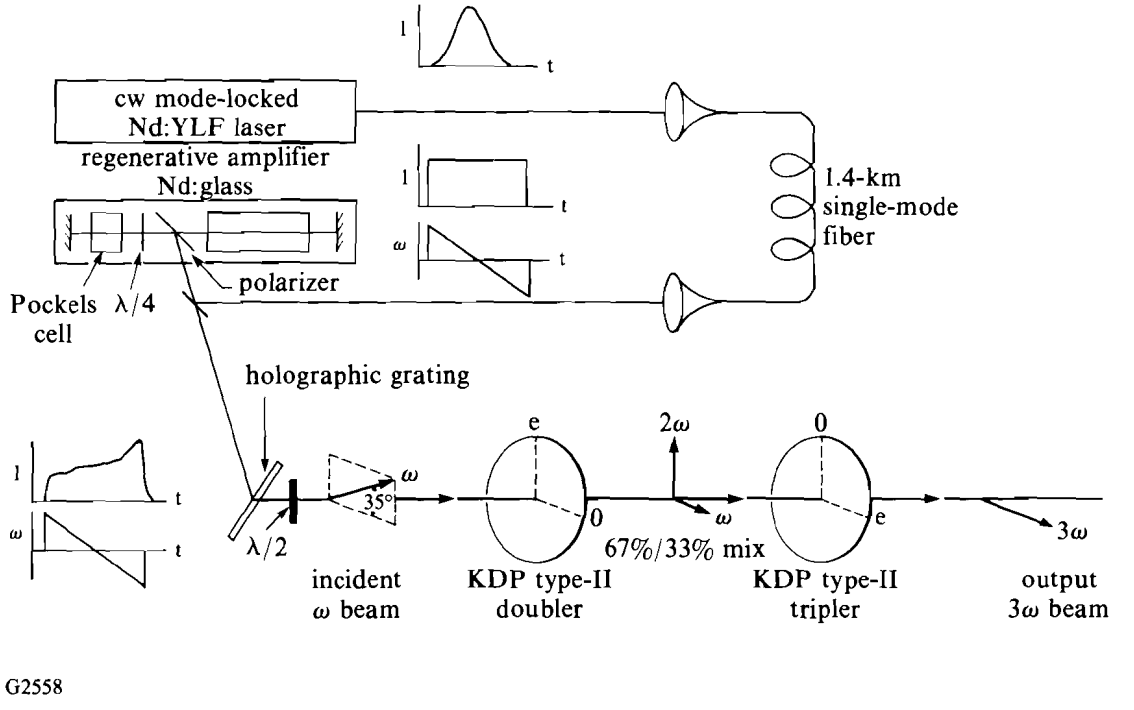

Fig. 37.32
The experimental setup used to study broadband frequency tripling included a cw mode-locked Nd:YLF laser source that was fiber-optically coupled to a Nd:glass regenerative amplifier. 25 Å of spectral broadening was generated through 800 m of fiber and maintained within the regenerative amplifier. The broadband radiation was harmonically converted through a KDP crystal, using the angular dispersion made available by the holographic gratings.

For the case when angular spectral dispersion was impressed on the input wave, the grating was oriented so that the plane of dispersion contained the *e*-axis of the tripling crystal. The source of dispersion was a Holotek[4] photoresist, holographic "Master" grating. The periodic structure of the grating had a spacing of about 1.1 μm and was used at 45° to produce an angular spectral dispersion of 137 μrad/Å. The beam was then passed through a polarizer to set the polarization required for optimum harmonic generation. The beam intensity was adjusted by way of a half-wave plate located before the polarization-sensitive diffraction grating. The second-harmonic converter was a 1.6-cm KDP crystal oriented with its optic axis in the *y*-*z* plane. The

optic axis of the doubling crystal was adjusted so that the phase-matching condition was satisfied by the center frequency of the input laser. Since the angular dispersion of the input wave was in the x-z plane, the frequency components of the input beam are effectively all o rays within the doubler and are insensitive to small angular changes. The second-harmonic signal then exits the crystal polarized in the y-direction and is mixed with the residual fundamental radiation in another 1.6-cm KDP crystal. The third-harmonic generation crystal was oriented with its optic axis in the x-z plane so that the angular dispersion impressed on the input wave matched the acceptance angle of the tripler (166 μrad/Å).

The experiment measured the intensity of the third-harmonic signal as a function of the tuning angle, with and without angular dispersion from the high-power grating. The results are displayed in Fig. 37.33. The intensity of the third-harmonic signal increased by greater than a factor of 2.5 for the case when angular dispersion was impressed on the input beam.

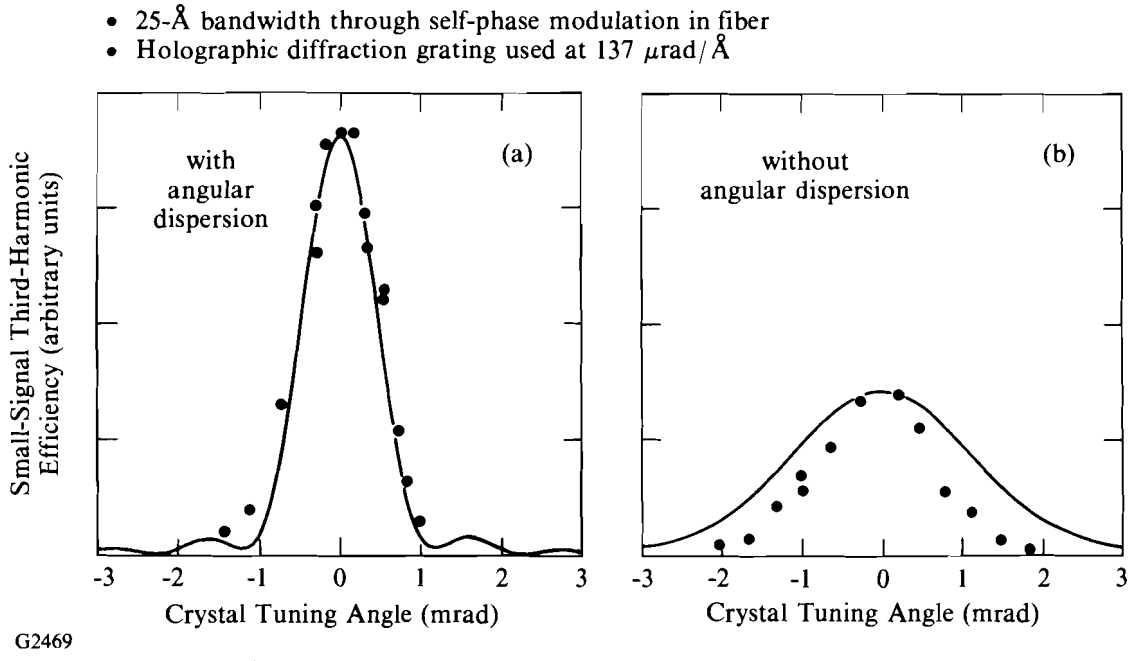

Fig. 37.33
For the first time, optimum third-harmonic generation of broadband light was demonstrated using angular spectral dispersion. Without angular dispersion, the tripler efficiency is relatively insensitive to tuning angle. Tripler efficiency substantially increases with the addition of an angular dispersion that approaches the wavelength mismatch in the KDP tripling crystal.

SSD Demonstration on OMEGA

Broadband phase conversion using SSD has recently been fully implemented on the OMEGA laser system. A wide range of diagnostics was deployed to demonstrate the benefits of SSD, both for

the fusion target and the laser system. Figure 37.34 is a comparison of the equivalent-target-plane intensity distributions for normal focusing (a), phase-converted focusing (b), and broadband phase conversion using SSD (c). Phase conversion with the distributed phase plates produces a well-defined envelope and shifts the intensity-power spectrum toward high spatial frequencies. SSD smooths these higher spatial frequencies and reduces the modulation of the lower spatial frequencies at the same time.

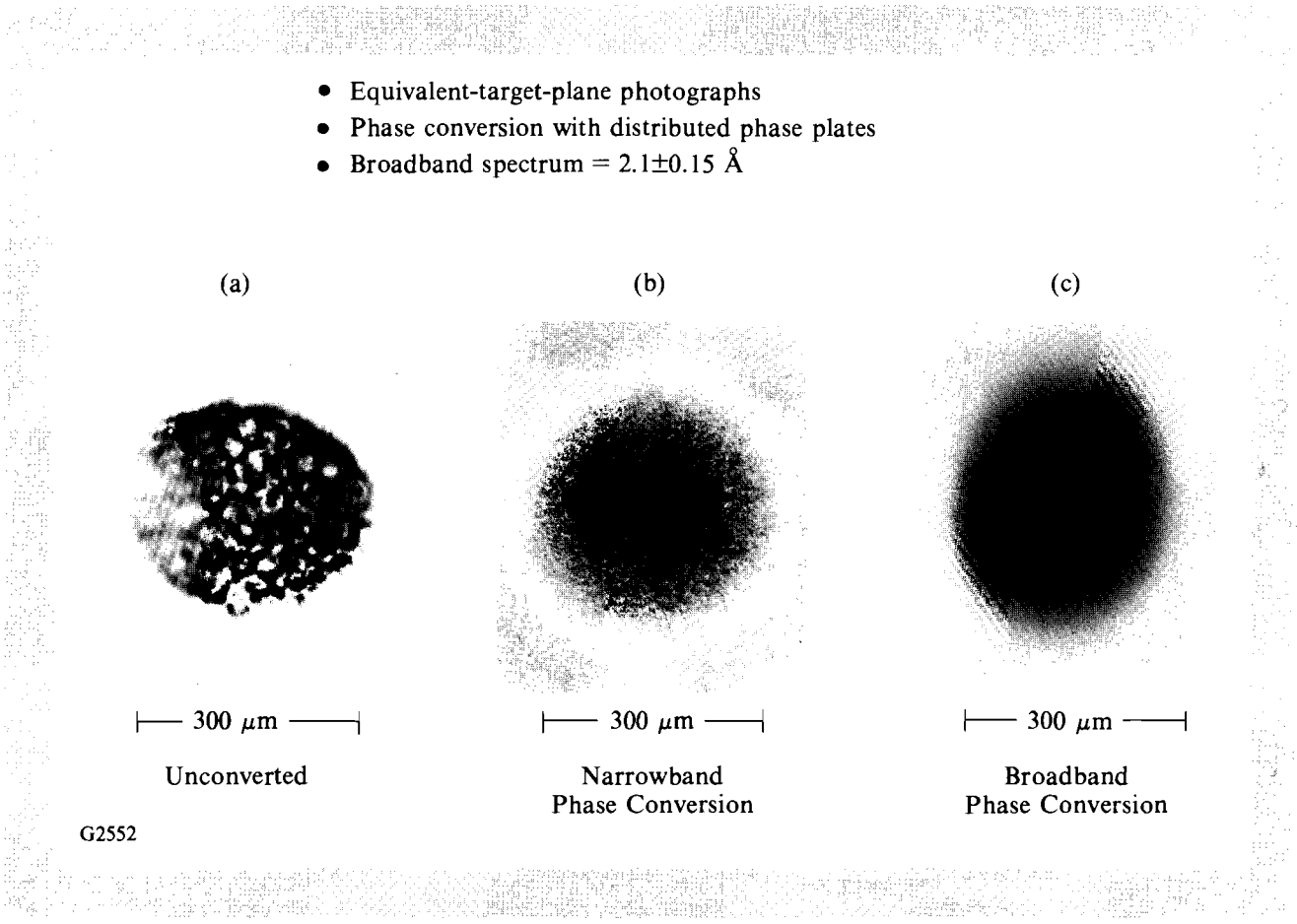

Fig. 37.34
Equivalent-target-plane photography shows dramatic improvements in the focal beam quality after implementing SSD on the OMEGA laser. Normal focusing of frequency-tripled laser light shows hot-spot intensity features (a). The distributed phase plates (DPP's) provide a well-defined envelope and an insensitivity to near-field wave-front errors (b). Spectral dispersion provides a substantial smoothing of the structure produced by the phase plate (c).

The resulting intensity distributions are smooth enough to require diligent cleaning and calibration of the photographic diagnostics. Figure 37.35 is a comparison of cross sections of intensity for phase conversion with and without SSD. The cut-off spatial frequency, corresponding to 3 μm, is fully sampled for the data. Therefore, no amount of smoothing is assumed for these representations of the equivalent target plane. It is clear from the comparison that substantial smoothing has been achieved in both directions: parallel and

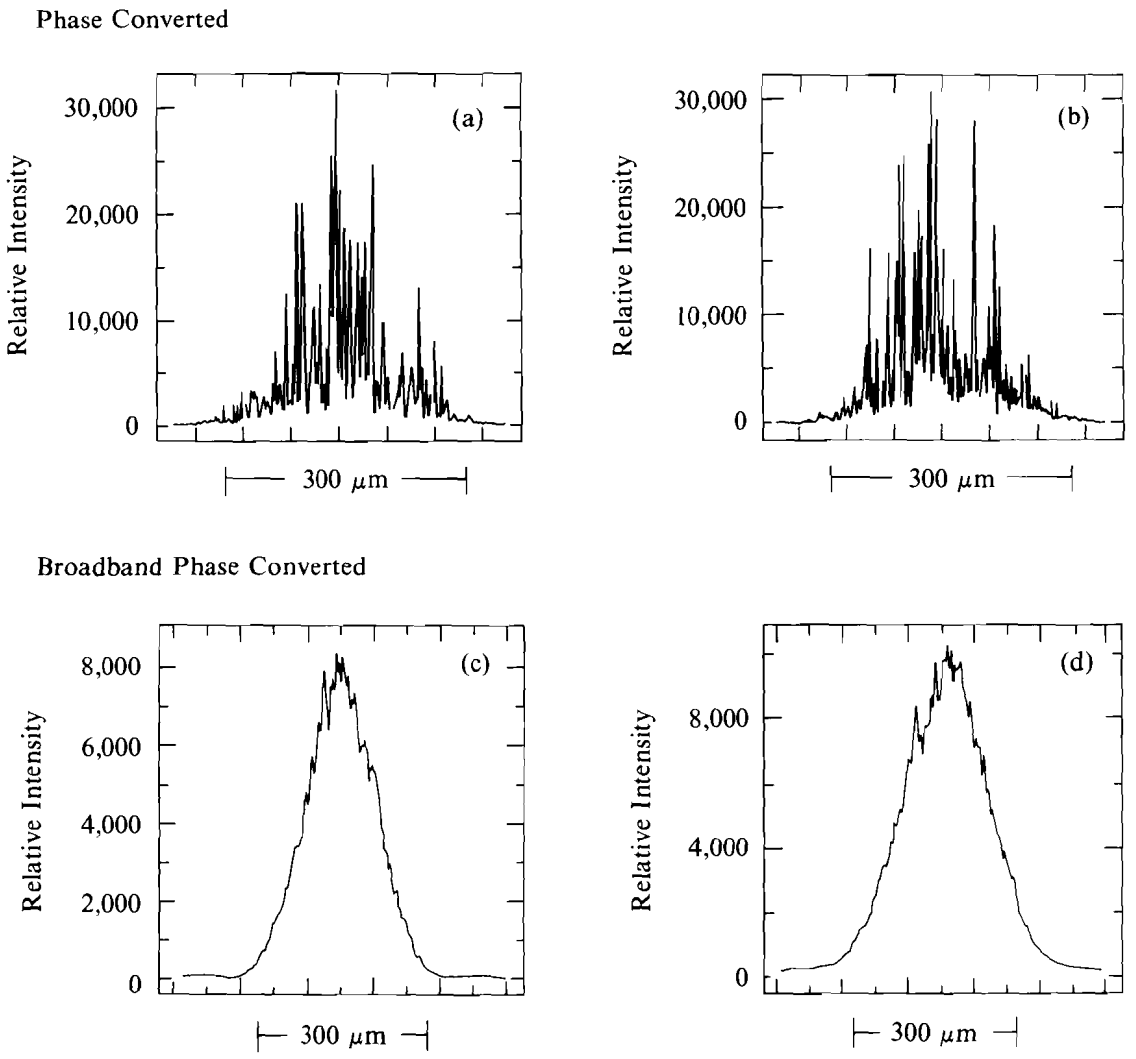

Fig. 37.35
Cross sections of the intensity distribution show a high level of beam smoothing by SSD. The cross sections are resolved to the limiting spatial frequency corresponding to 3 μm. Smoothing is observed in both dimensions: parallel and perpendicular to the direction of spectral dispersion.

perpendicular to the axis of spectral dispersion. Accurate assessment of the benefit from 24 smooth laser beams is obtained by a computer calculation that involves beam superposition about a sphere and an ℓ-mode decomposition of the resulting intensity distribution. Figure 37.36 shows a substantial decrease in the amplitude of all of the ℓ-modes, indicating a significant improvement in irradiation uniformity for the OMEGA laser system.

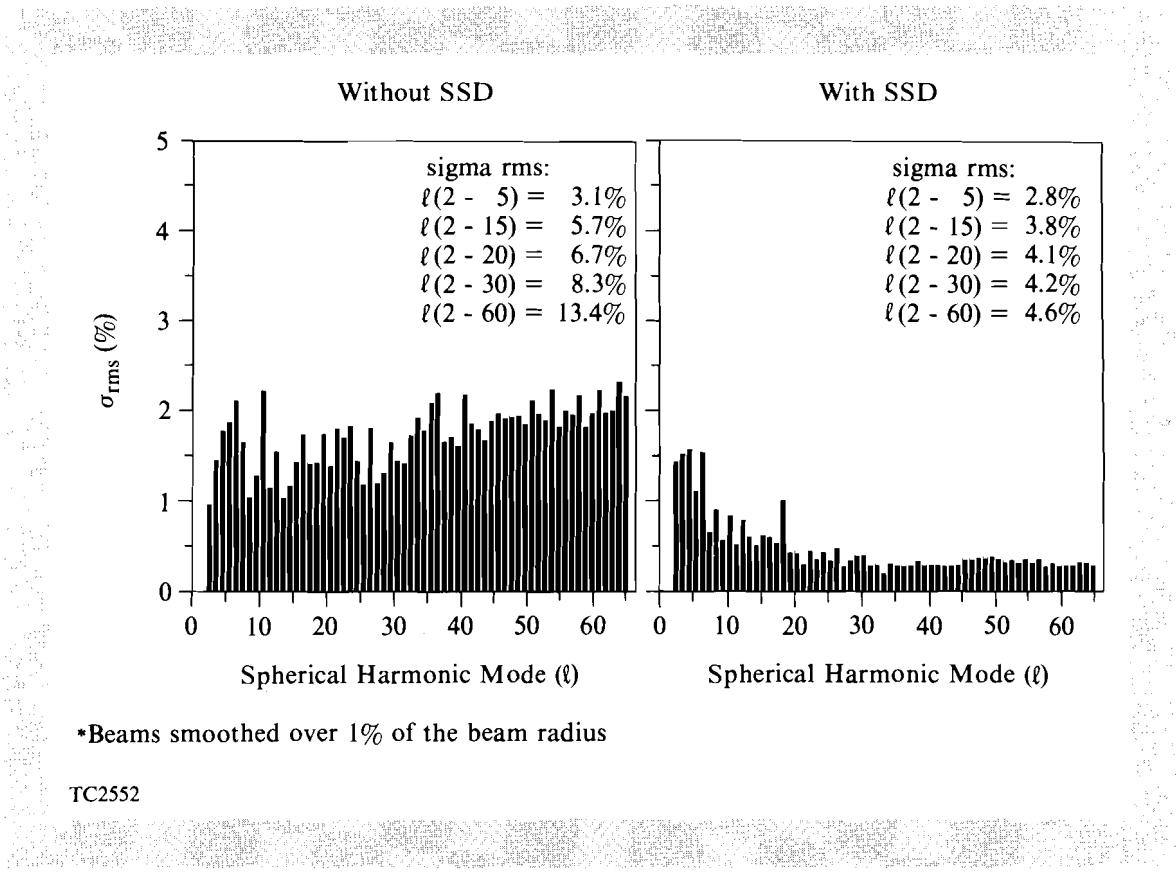

Fig. 37.36
Superposition of the 24 OMEGA focal distributions shows a substantial improvement in irradiation uniformity. The ℓ-mode decompositions show greater than a factor-of-4 times lower nonuniformity when using SSD.

Additional beam smoothing has been demonstrated from free-space propagation between the frequency-conversion crystals and the target chamber. Furthermore, a more optimum envelope from each of the individual laser beams is achieved by operating the distributed phase plates out of the exact Fourier plane.

Conclusion

A novel beam-smoothing technique—smoothing by spectral dispersion (SSD)—has been successfully implemented on the OMEGA laser system. The integration of a large-aperture, high modulation-index, microwave phase-modulator and high-power, high-efficiency, holographic diffraction gratings has made it possible to manipulate a beam's spectral distribution in time and space. Substantial improvement in the uniformity of irradiation from the OMEGA laser has been demonstrated.

ACKNOWLEDGMENT

This work was supported by the U.S. Department of Energy Office of Inertial Fusion under agreement No. DE-FC03-85DP40200 and by the Laser Fusion Feasibility Project at the Laboratory for Laser Energetics, which has the following sponsors: Empire State Electric Energy Research Corporation, New York State Energy Research and Development Authority, Ontario Hydro, and the University of Rochester. Such support does not imply endorsement of the content by any of the above parties.

REFERENCES

1. LLE Review **33**, 1 (1987).
2. M. Born and E. Wolf, Principles of Optics, 6th ed. (Pergamon Press, NY, 1980), pp. 401–414.
3. H. M. Smith, *Holographic Recording Materials* (Springer-Verlag, Berlin, 1977), pp. 209–226.
4. Holotek LTD., Holotek products literature, August 1984, pp. 4–5.
5. D. Strickland and G. Mourou, "Compression of Amplified Chirped Optical Pulses," *Opt. Commun.* **56**, 219 (1985).
6. T. J. Kessler, M. S. thesis, The Institute of Optics, University of Rochester, 1984.

ACKNOWLEDGMENT

This work was supported by the U.S. Department of Energy Office of Inertial Fusion under agreement No. DE-FC03-85DP40200 and by the Laser Fusion Feasibility Project at the Laboratory for Laser Energetics, which has the following sponsors: Empire State Electric Energy Research Corporation, New York State Energy Research and Development Authority, Ontario Hydro, and the University of Rochester. Such support does not imply endorsement of the content by any of the above parties.

REFERENCES

1. LLE Review **31**, pp. 106ff and 114ff (1987); S. Skupsky and T. Kessler (accepted for publication in *Opt. Commun*).
2. LLE Review **36**, pp. 158ff (1988); LLE Review **33**, pp. 1ff (1987).
3. W. Seka, S. D. Jacobs, J. E. Rizzo, R. Boni, and R. S. Craxton, *Opt. Commun.* **34**, 469 (1980); R. S. Craxton, *ibid.* **34**, 474 (1980).
4. J. B. Trenholme and K. R. Manes, Lawrence Livermore National Laboratory Report UCRL-51413 (1972).
5. R. S. Craxton, *IEEE J. Quantum Electron.* **J-QE-17**, 1771 (1981).

1.C Improved Laser-Beam Uniformity by the Angular Dispersion of Frequency-Modulated Light

A new technique is being examined to improve the quality of OMEGA laser beams beyond the level that has already been achieved with distributed phase plates (DPP's).[1] These phase plates break each beam into beamlets whose diffraction-limited size equals the size of the target.[2] However, superimposed on the smooth diffraction-limited intensity envelope is a rapidly varying intensity structure from the interference between the different beamlets (Fig. 37.20). Once a plasma atmosphere has been established around the target, much of the short-wavelength interference structure in the laser-energy deposition is expected to be smoothed by thermal conduction within the target as heat is transported from the place of energy deposition to the ablation surface. However, before thermal smoothing becomes effective, this structure could imprint itself on the target surface and "seed" the Rayleigh-Taylor instability, much like a target surface imperfection. The longer-wavelength interference structure will never be adequately smoothed and could drive a distorted implosion. The goal of the work described here is to develop a technique to reduce the magnitude of the interference structure, while retaining the smooth intensity envelope.

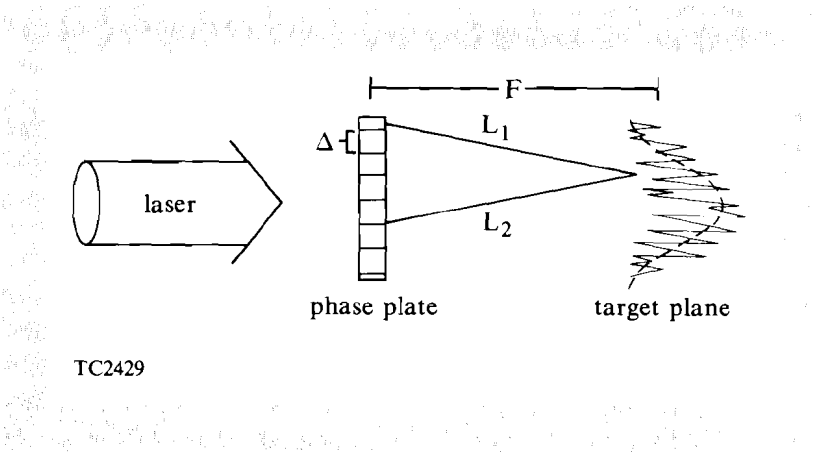

Fig. 37.20
The phase-plate intensity pattern in the focal plane consists of a diffraction-limited envelope superimposed upon a rapidly varying structure caused by the interference between rays from different DPP elements.

The strategy employed is to shift the interference pattern on a time scale Δt that is short compared to the characteristic hydrodynamic response time of the target. At any instant of time, a highly modulated intensity pattern will be present, but the time-averaged intensity over Δt will be smooth. The interference pattern can be shifted (or changed) by rapidly shifting the beam, or rapidly changing the relative phases between the individual beamlets. An example of the latter approach is induced spatial incoherence (ISI).[3] But ISI might not be a good candidate for a frequency-tripled glass-laser system such as OMEGA, since the required "chaotic" bandwidth could be difficult to triple efficiently and would produce high-intensity temporal spikes within the laser that could damage the laser glass. Therefore, we have been considering an alternate scheme, smoothing by spectral dispersion (SSD) of the laser light. Like ISI, it requires a bandwidth, but the smoothing mechanism is different, permitting the use of a nonchaotic bandwidth and allowing high-efficiency frequency tripling. A possible method of implementing SSD on a limited scale, with current technology, is described below. This relatively simple technique will not eliminate all the interference structure, but it takes a major step in that direction without degrading the performance of the high-power frequency-tripled laser system. Further improvements in uniformity are possible with other variations of SSD that are presently under investigation.

Implementation Considerations for SSD

The general concept of SSD is to spectrally disperse broad-bandwidth light onto a phase plate so that, ideally, each element of the DPP is irradiated by a different frequency.[4] The relative phase between rays from different phase-plate elements will then vary in time according to their frequency differences. The larger the bandwidth, the more rapidly the structure will change and the more rapidly the time-averaged intensity will smooth. However, if some phase-plate elements have the same "color" (frequency), a residual interference structure will be produced that will not smooth.

To implement this scheme on a laser system such as OMEGA, a number of key requirements must be met: (1) generation of bandwidth that will not damage the laser glass; (2) dispersion of the bandwidth

across the DPP elements together with high-efficiency frequency tripling; (3) identification of a dispersing configuration that will not significantly distort the beam; and (4) obtaining the improved uniformity over a sufficiently small averaging time.

1. Bandwidth Source

One form of bandwidth that can be easily propagated through a glass laser system is generated by phase modulation of the beam. The phase-modulated electric field is of the form[5] $E(t) = E_0(t)e^{i\Phi(t)}$, where the entire effect of bandwidth on the original field E_0 is contained in the time-varying phase. The laser intensity varies as $|E(t)|^2 = |E_0(t)|^2$ and contains no additional high-intensity spikes from the interference between different frequencies. This would not be true for the chaotic form of bandwidth required by ISI in which the different modes have random phases (i.e., $E(t) = \Sigma a_n e^{i\omega_n t + \phi_n}$ where ϕ_n is random). One relatively simple form of phase modulation can be obtained by passing the laser beam through an electro-optical (E-O) crystal with an imposed oscillating electric field. The effect is to produce a laser electric field of the form:

$$E(t) = E_0 e^{i\omega t + i\delta \sin \omega_m t}, \tag{1}$$

where δ and ω_m are the modulation amplitude and angular frequency of the E-O device, and ω is the fundamental angular frequency of the laser. By expanding the exponential term in a Bessel function series[5]:

$$E(t) = E_0 \sum_{-\infty}^{\infty} J_n(\delta) e^{i(\omega + n\omega_m)t}, \tag{2}$$

we see that the beam contains frequency side bands in increments of ω_n, which extend out to approximately $\pm\delta\omega_m$, at which point the mode amplitudes (J_n) begin to approach zero. Formally, Eq. (2) also contains a factor $\exp(i\, k_n z)$ where $k_n = (\omega + \omega_n)/c$; the time variable has actually been replaced by $t - z/c$.

2. Bandwidth Dispersion

A crucial element of SSD is that a large number of the DPP elements must be irradiated by different frequencies at each instant of time. The E-O phase-modulated beam, by itself, would not be adequate for SSD, because at any time all DPP elements would be irradiated by only a single dominant frequency given by the time derivative of the phase in Eq. (1). It remains to disperse the different frequencies in the spectrum across the DPP elements. This can be done, in part, by introducing a spatially varying time delay t_D across the beam in, say, the Y direction of the form $t_D = \alpha Y/\omega_m$. Replacing t by $t + t_D$ in Eq. (1), the time-delayed electric field becomes

$$E_D = E_0 e^{i\omega t + i\delta \sin(\omega_m t + \alpha Y)}. \tag{3}$$

The instantaneous frequency, given by the time derivative of the phase in Eq. (3), now varies across the beam. We see it is not necessary to allow the beams to freely propagate to spatially separate the different frequency components as was previously suggested[4] for SSD; "color" variation has been obtained already with only angular dispersion of the frequencies, resulting in a variable time delay.

Such a time delay can be conveniently introduced by means of a diffraction grating, as illustrated in Fig. 37.21. The grating will, of course, also introduce an angular dispersion to the different frequency components, which can be found from the Bessel-function expansion of Eq. (3):

$$E_D = E_o \sum J_n(\delta)\, e^{i(\omega + n\omega_m)t + in\alpha Y} \quad . \tag{4}$$

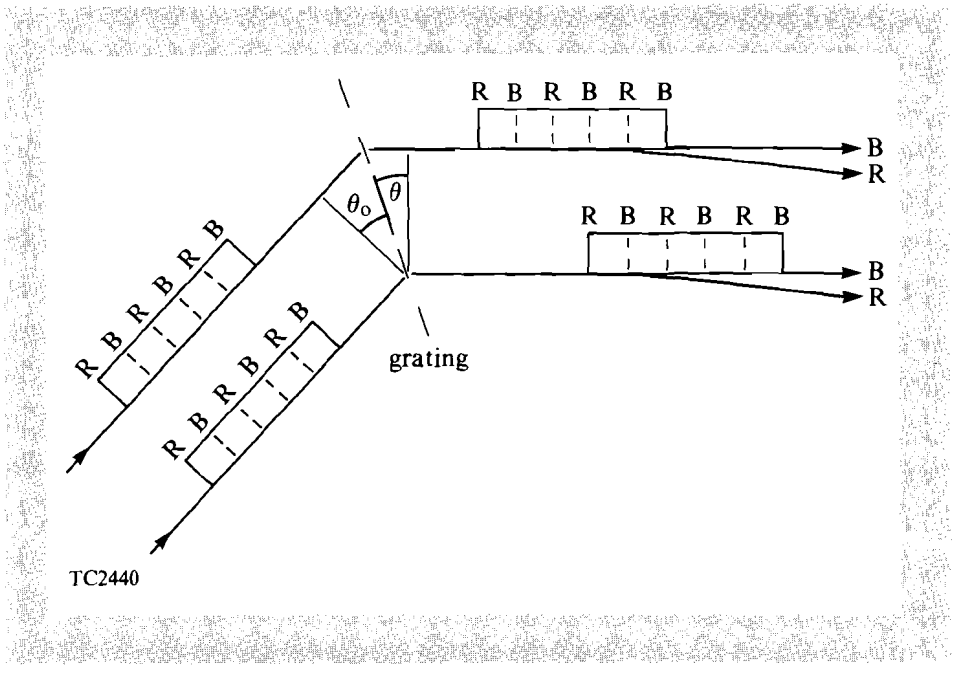

Fig. 37.21
The diffraction grating introduces a time delay across the beam in addition to angular dispersion of the spectrum.

Using the implicit kz dependence in the phase, a contour of constant phase for the nth harmonic is given by $k_n z + \alpha n Y =$ constant. The wave propagates at approximately the angle: $\alpha n/k$ relative to the direction of the fundamental frequency. This angular dispersion is important for high-efficiency frequency conversion as discussed below.

Unfortunately, the time delay, which produced the required frequency variation across the beam, has also distorted the temporal shape of the beam as shown in Fig. 37.21. Not only will the pulse be lengthened, but there will be intensity variations across the beam aperture. This can be corrected by inserting an additional grating before the E-O modulator (Fig. 37.22).

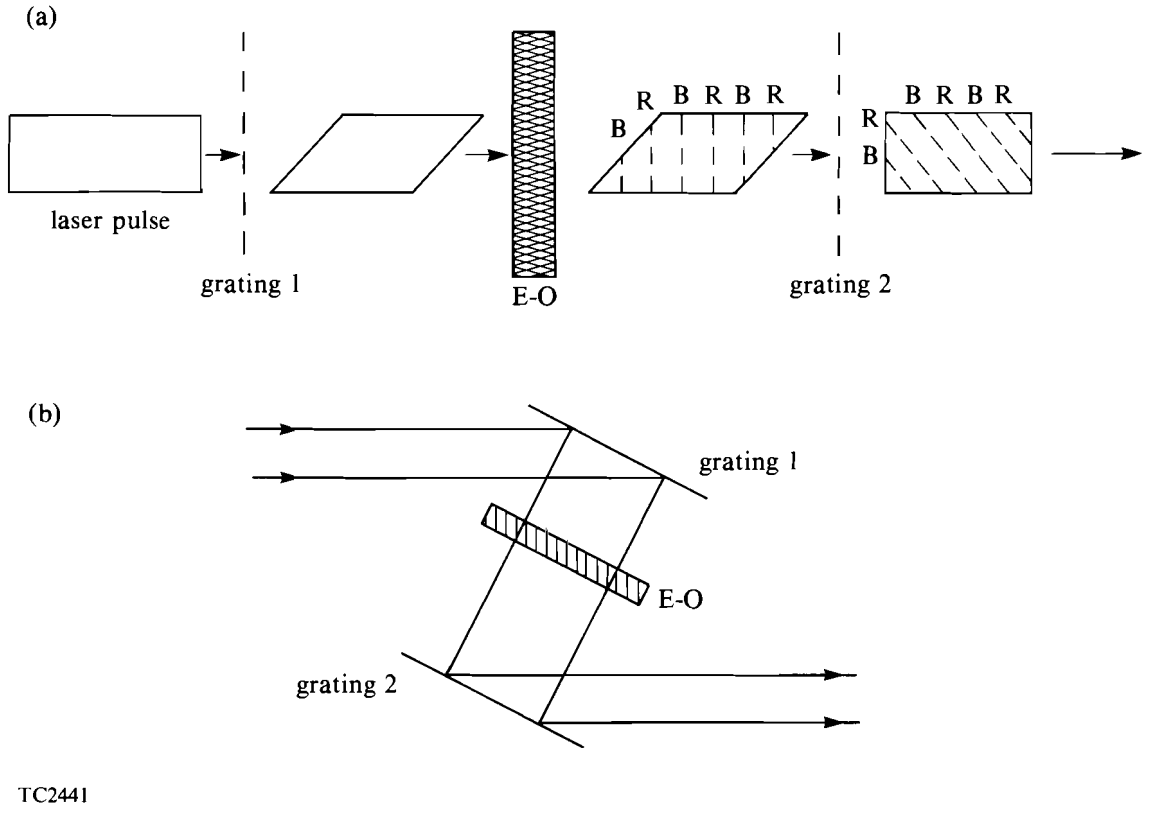

Fig. 37.22
The two-grating configuration. (a) Grating 1 introduces a "pre-delay" that compensates for the delay produced by grating 2. By placing the first grating before the modulator, it is possible to correct the time delay without affecting the angular dispersion of the spectrum. (b) A schematic of (a).

When the beam passes through the first grating, its residual bandwidth will, of course, be dispersed; this dispersion is a negligible effect for a typical bandwidth-limited laser beam, and will in any case be corrected by the second grating. The main effect is to introduce a time delay opposite to the one that will be induced by the grating after the E-O modulator. The time-distorted beam passes through the modulator where the bandwidth is imposed. The grating after the E-O modulator now serves a dual purpose: it restores the beam to its correct temporal shape, and it imposes the spatial-frequency variation required for SSD (and also, as discussed below, the correct dispersion for frequency tripling).

3. Diffraction Grating Considerations

The current strategy is to insert the diffraction gratings into the driver, thereby avoiding any additional optical elements at the end of the laser system. The spectral angular divergence imposed in the driver must then be able to propagate through the remainder of the laser and onto the target without significant energy loss or beam distortion. This places an upper bound on the amount of divergence permitted. For instance, if we do not want the spread in the beam at the target plane to be larger than, say, half the target diameter D_T then

$$F\theta \lesssim \tfrac{1}{2}D_T \ ,$$

where F is the focal length and θ is the full-angle beam spectral divergence. For OMEGA, $F \approx 60$ cm and, for recent experiments, $D_T \approx 300$ μm. Thus, the largest permitted divergence is ~ 200 μrad, at the 20-cm aperture at the end of the system. Such a divergence can propagate through the OMEGA laser system, if it is introduced near the end of the driver, at the 64-mm stage, where it would have a value three times greater (~ 600 μrad), because the beam divergence changes inversely as the diameter of the beam.

The limit on beam divergence also places an upper bound on the maximum bandwidth that will frequency triple with high efficiency. In order to remain within 10% of the maximum conversion efficiency[4,6] with the permitted 200-μrad divergence, the bandwidth must not be greater than ~ 2 Å in the IR. This bandwidth would normally be too small to smooth the laser intensity on the time scale of interest (~ 50 ps) for the OMEGA experiments. But upon frequency conversion, the frequency spread is also tripled. Further, we can take advantage of "color cycling," as will be discussed below, to further reduce the smoothing time for the long-wavelength interference structure.

We can now determine the grating configuration that would produce the 200-μrad dispersion of the 2-Å bandwidth. The grating dispersion in the first order is given by[7]

$$\frac{\Delta\theta}{\Delta\lambda} = \frac{1}{\cos(\theta)d} \ ,$$

where d is the spacing between grooves on the grating and θ is the angle between the transmitted beam and the normal to the grating. A typical value for d is 628 nm. For OMEGA, the beam divergence will be 2.9 times larger at the 64-mm point than it is at the output, i.e., $\Delta\theta/\Delta\lambda = 2.9 \times (200\ \mu\text{rad}/2\ \text{Å})$ at the diffraction grating. Therefore, $\cos\theta = 0.54$ and $\theta = 57°$. The minimum length of the grating L can also be determined; it is the beam diameter (58 mm) divided by $\cos\theta$, yielding $L = 10.6$ cm. Gratings with these parameters have been obtained.

4. "Color" Cycling

The time delay across the grating can be used further to our advantage. Fig. 37.22 shows that if the E-O modulation time τ ($=2\pi/\omega_m$) is shorter than the time delay t_D, then all the "colors" will cycle across the beam more than once at each instant in time. (More correctly, one cycle from the "reddish" to "bluish" components of the bandwidth occurs in 0.5 τ.) Thus, instead of the "red-blue" variation being distributed from one end of the DPP to the other, it can be distributed over smaller regions of the DPP, so that nearest elements will have a larger frequency difference and their average interference pattern will smooth in a shorter time. For instance, with $1.5\ \tau = t_D$, the smoothing time for nearest neighbors is three times shorter than if there had been only one color cycle. The price paid is that more

distant DPP elements will have the same color and their interference pattern will not smooth at all. However, the interference between distant elements produces shorter-wavelength structure that can be smoothed more easily within the target by thermal conduction of the deposited laser energy. The effect of color cycling is qualitatively similar to that produced by repeated echelon steps in the ISI technique.[2]

To calculate the E-O modulation frequencies that will produce different amounts of color cycling, we first determine the delay time. From Fig. 37.21,

$$t_D = L|\sin\theta + \sin\theta_o|/c, \tag{5}$$

where θ_o is the incident angle of the beam on the grating. The grating dispersion was chosen so that $\theta_o = \theta$ to prevent beam distortion. The incident angle is found from the usual grating equation[7]:

$$|\sin\theta_o + \sin\theta| = \frac{\lambda}{d} \quad . \tag{6}$$

Substituting Eq. (6) into Eq. (5) yields

$$t_D = \frac{L}{c}\frac{\lambda}{d} \quad . \tag{7}$$

For the above values of L and d, and for $\lambda = 1$-μm laser light, the delay time t_D is 590 ps. This is approximately the pulse width for current OMEGA experiments, so that the pulse shape after the first grating in Fig. 37.22 will be highly distorted. For the example of three color cycles in the transverse direction across the beam ($\tau = 0.67\,t_D$), the modulation frequency $\nu_m (= 1/\tau)$ is 2.5 GHz. The required modulation amplitude δ can also be determined by the following argument. The frequency spread $\Delta\nu$ produced by the 2-Å IR bandwidth is $\Delta\nu = \Delta\lambda c/\lambda^2 = 60$ GHz. The frequency bandwidth produced by E-O modulation is $\Delta\nu = 2\delta\nu_m$ [see discussion of Eq. (2)]. Thus, the modulation amplitude is $\sim 4\pi$ for $\nu_m = 2.5$ GHz.

Simulation Results

To calculate the total electric field on the target (i.e., laser focal plane), we use scalar diffraction theory[8] to propagate the beam from the phase plates. The beam is first decomposed into its individual frequency components; each frequency is transported separately and then summed in the focal plane. The initial amplitude of each frequency component is determined by the frequency-tripling process.

For a model of the frequency-tripled laser light, we use the following physical argument. The E-O broadened light is oscillating from "red" to "blue" such that at any instant of time only a small frequency range is dominating. The entire small range is approximately phase matched to the crystal because of the angular dispersion of the grating, and high-efficiency conversion should occur.

This process was calculated using the approximations discussed in Ref. 9. Figure 37.23(a) shows the initial 2-Å bandwidth given by Eq. (2), and Fig. 37.23(b) shows the calculated tripled spectrum. The frequency spread has tripled; the shape of the spectrum is given by Eq. (1) with both ω and δ tripled. This result would not apply to the general case of broad-bandwidth light where mode-mode interactions might degrade the conversion efficiency.

Thus, the electric field for the E-O-broadened, frequency-tripled light used here is assumed to be

$$E_{3\omega} = e^{i3\omega t + i3\delta\sin(\omega_m t + \alpha Y)} \quad .$$

The scalar amplitude of this wave in the focal plane, after passing through the phase plate, is

$$U(x,y) = U_0 e^{i3\omega t} \times \sum_{KL} \sum_{n} J_n(3\delta) e^{i(n\omega_m t - 2n\gamma L - 2Lq - 2Kp + \phi_{KL})} \times \frac{\sin(n\gamma + q_n)}{n\gamma + q_n} \frac{\sin p_n}{p_n} \quad , \tag{8}$$

Fig. 37.23
Calculation of the intensity spectrum showing bandwidth tripling upon frequency tripling of a phase-modulated pulse. The slight broadening of each spectral line is due to the finite pulse width of 700 ps used in the calculation.

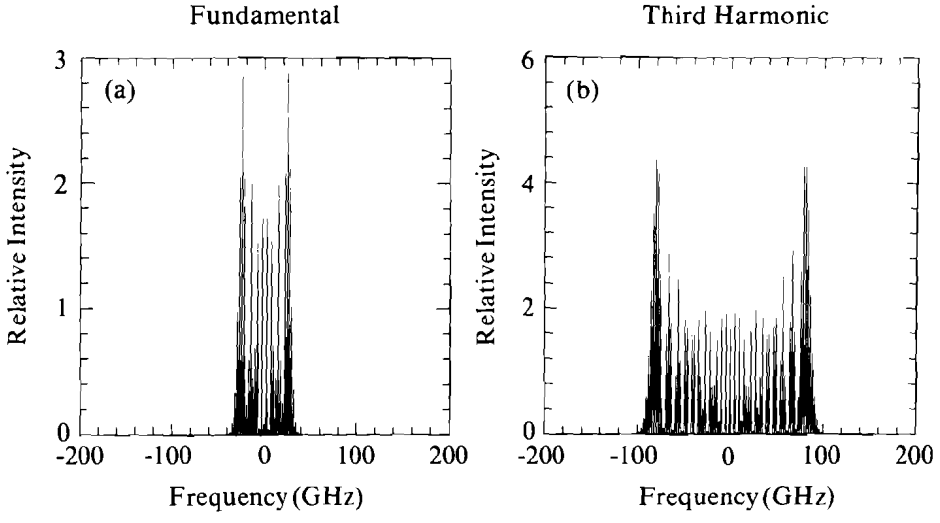

• E-O phase-modulated beam: $\nu = 2.5$ GHz, $\delta \approx 4\ \pi$

TC2553

where K, L corresponds to a DPP element, and ϕ_{KL} is the phase imposed by that element. The variables (p_n, q_n) are related to the coordinates (x, y) in the focal plane by

$$(p_n, q_n) = (x,y)k_n\Delta/2F \quad ,$$

where k_n is the wave number, Δ the distance between phase-plate elements, F the focal length, and $\gamma = \alpha\Delta/2$.

One effect of the spectral angular dispersion is to shift the center of the diffraction envelope for each mode in the q (y) direction. The envelope is no longer the same in the x and y directions; this can introduce long-wavelength modes of irradiation nonuniformity. For the small bandwidth used here, the distortion is relatively small and can be compensated for by using rectangular DPP elements so that the ratio of x to y length is $\sim$0.75 (Fig. 37.24). This reduces the diffraction size of the beam in the y direction to approximately compensate for the spread caused by spectral dispersion. The effect on Eq. (8) is to multiply p_n by 0.75.

The time-averaged, single-beam intensity in the focal plane is

$$I(x,y) = \frac{1}{\Delta t}\int_0^{\Delta t} |U|^2 dt \quad .$$

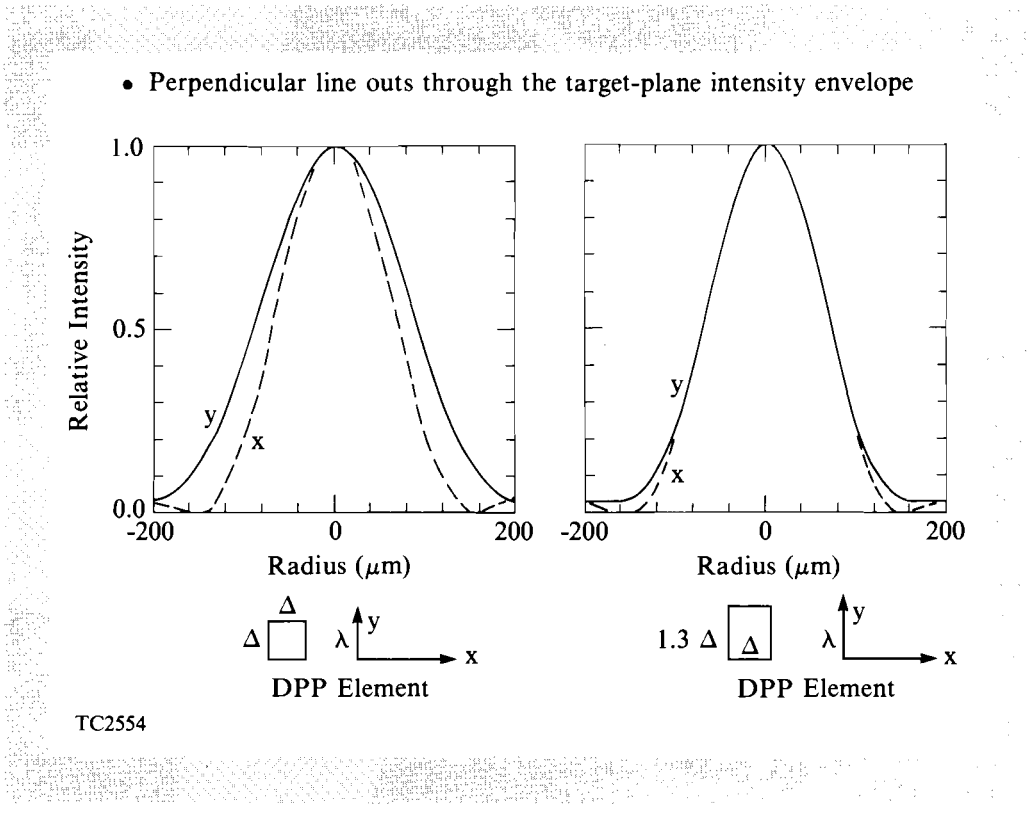

Fig. 37.24
Correction of the beam ellipticity, in the target plane, by elongating the phase-plate elements in the direction of frequency dispersion. This reduces the diffraction spread in that direction, in part compensating for the spectral dispersion.

The intensity on target is the superposition of 24 such intensity patterns. Figure 37.25 shows the rms energy-deposition nonuniformity as a function of the averaging time Δt. The deposited energy was assumed to be smoothed by thermal conduction over 1% of the target radius, which is a conservative estimate; computer simulations of OMEGA experiments show smoothing distances many times larger.

The nonuniformity without SSD ($\Delta t = 0$) is $\sim 12\%$ for the assumed amount of thermal smoothing. SSD, with the 2-Å IR bandwidth and 2.7-GHz modulation frequency, reduces the nonuniformity by factors of 2 to 3 in averaging times of 25–50 ps. The nonuniformity asymptotes to about 4% rms. This residual nonuniformity has two sources. First, bandwidth is dispersed only in the y direction so that all phase-plate elements in the x direction have the same frequency (for a given y); these will form a time-independent interference structure. Second, the oscillating bandwidth causes the interference pattern to repeat after each modulation cycle.

For comparison, results are also shown in Fig. 37.25 for increasing the number of beams and increasing the smoothing distance. A 60-beam configuration can reduce the nonuniformity by a factor of ~ 2, and increased smoothing ($\Delta R/R = 5\%$) reduces σ_{rms} by another factor of 2.

Although the resultant uniformity is not perfect, the predicted factor of 2 to 3 reduction in σ_{rms} could significantly improve results for OMEGA high-density experiments, and this improvement can be attained with relatively simple modifications of the laser system.

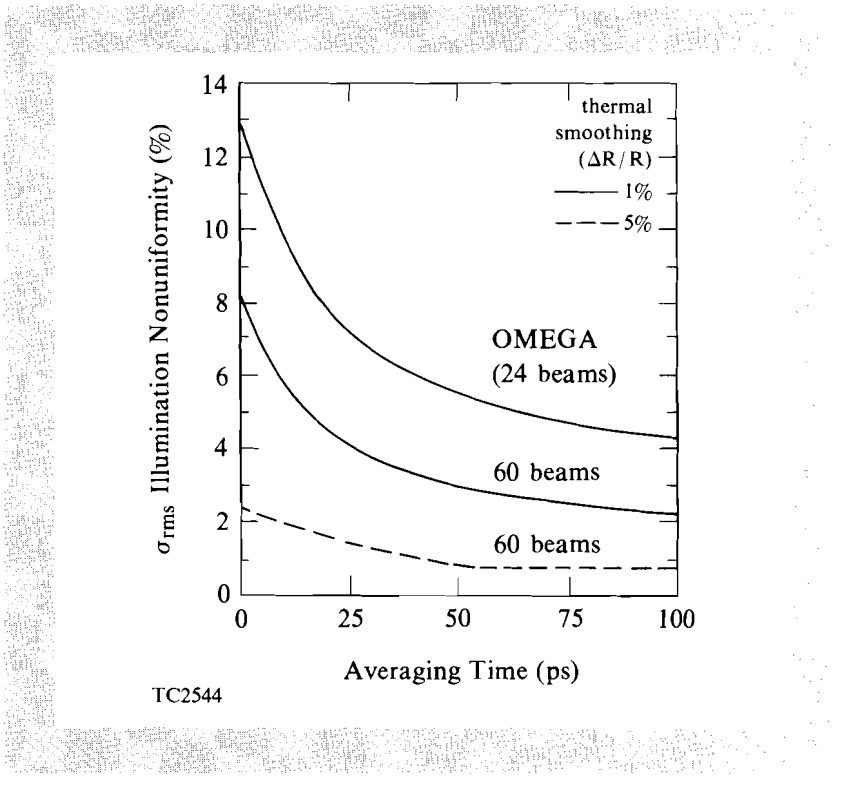

Fig. 37.25
The relatively simple variation of SSD reduces the time-averaged nonuniformity by factors of 2 to 3 in averaging times of 25–50 ps. A 2-Å IR bandwidth was used, and a thermal-smoothing distance of only 1% of the target radius was assumed. Increasing the number of beams from 24 to 60 reduces the nonuniformity by a factor of ~ 2, and increasing the smoothing distance to 5% of the radius, which is consistent with computer simulation, reduces σ_{rms} by an additional factor of 2.

Summary

A relatively simple form of SSD is being investigated for implementation on OMEGA. It is simple in the sense that all new optical elements are installed in the driver, and no additional components are required at the end of the system. An E-O frequency-modulated pulse is used for the bandwidth to prevent the formation of high-intensity spikes that could damage the laser glass, as might occur with a chaotic form of bandwidth. The essential spatial variation of colors on the DPP and angular dispersion for frequency tripling is accomplished with a set of diffraction gratings that take advantage not only of the dispersion properties of the gratings but also their time-delay characteristics.

The same features that make this technique relatively simple also limit the maximum bandwidth to ~2 Å for OMEGA. (The bandwidth could be increased to ~4 Å without increasing the spectral dispersion, and it will result in only about a 15% reduction in frequency-conversion efficiency.) However, even with 2 Å, adequate smoothing times can be achieved because this bandwidth is tripled upon frequency conversion and because we can employ color cycling. Computer simulations show that this variation of SSD can reduce the rms nonuniformity on OMEGA by factors of 2 to 3 in averaging times of 25–50 ps.

Even further improvements in uniformity are possible with SSD, but it would involve spatial dispersion of frequencies; in contrast, only angular dispersion was considered here. The spatial dispersion could be more difficult to implement and would require additional lenses around the tripling crystals for optimal conversion efficiency. Hybrids are also possible, with spatial dispersion in one direction and angular dispersion in the other. Such variations of SSD are presently under investigation.

ACKNOWLEDGMENT

This work was supported by the U.S. Department of Energy Office of Inertial Fusion under agreement No. DE-FC03-85DP40200 and by the Laser Fusion Feasibility Project at the Laboratory for Laser Energetics, which has the following sponsors: Empire State Electric Energy Research Corporation, New York State Energy Research and Development Authority, Ontario Hydro, and the University of Rochester. Such support does not imply endorsement of the content by any of the above parties.

REFERENCES

1. LLE Review **33**, 1 (1987).
2. Y. Kato *et al.*, *Phys. Rev. Lett.* **53**, 1057 (1984).
3. R. H. Lehmberg, A. J. Schmitt, and S. E. Bodner, *J. Appl. Phys.* **62**, 2680 (1987).
4. LLE Review **36**, 158 (1988).
5. A. Yariv, *Quantum Electronics*, 2nd ed. (John Wiley & Sons, Inc., New York, 1975), Sec. 14.4.

Section 2
NATIONAL LASER USERS FACILITY NEWS

During the first quarter of FY89 NLUF activity consisted of supporting an experiment from **J. DeGroot**'s group at the University of California at Davis (UCD). **K. Mizuno** from UCD and **P. Young** from LLNL collaborated with **W. Seka** at LLE to measure ion-acoustic-decay instabilities with the GDL laser. A series of CH, Al, Mo, and Au targets were irradiated with laser intensities of 10^{13} to 1.5 $\times$ 10^{15} W/cm^2 in the green (531 nm) and the optical spectrum around $3\omega/2$ was recorded with a streak camera and a time-integrating spectrograph. The data have been taken to UCD for analysis.

The Division of Plasma Physics of the APS meeting was held in Hollywood, Florida. Papers were presented by eleven different NLUF users at both the oral and poster presentations. The abstracts from these papers are in the *Bulletin of the APS*, Vol. 33, No. 9. Research topics covered included laser-plasma interactions, XUV and x-ray spectroscopy, x-ray lasers, high-density compressions, and radiation transport. All of the presentations were well received by conference attendees.

Proposals for FY90 are to be sent to the DOE San Francisco office. The deadline for submission has been changed from 15 December to a later date. Please address all technical questions to the NLUF manager at LLE and all administrative and proposal submission questions to Dennis Neely in the DOE San Francisco office. The DOE office has assured LLE that money for approved research will be available the first quarter of FY90.

Section 3
LASER SYSTEM REPORT

3.A GDL Facility Report

During the first quarter of FY89 the glass development laser (GDL) was used by three in-house experimental groups and one NLUF user. The in-house experiments were conducted in the Beta target irradiation facility and concentrated on x-ray laser studies, x-ray lithography, and the transmission of light through multilayered targets. The x-ray laser experiments were aimed at observing gain in collisionally pumped neon-like nickel and germanium. The x-ray lithography experiment measured the silicon content of corn, which may serve as a new source of ultrapure silicon. These experiments are a collaboration between LLE and researchers at SUNY at Buffalo. The third campaign is a continuation of the study of the temporal behavior of multilayered targets. Ultimately this program will determine the relative importance of transmitted light in the interpretation of various multilayered-target experiments on OMEGA. Users from the University of California at Davis performed experiments that temporally resolved the second-harmonic emission from the target in order to study parametric processes in laser-plasma interactions.

A summary of GDL operations this quarter follows:

Beamline Test, Calibration, Tuning, and Laser Alignment Shots	321
Test Shots	
X-Ray Laser	76
X-Ray Lithography	23
Multilayer Experiments	51
NLUF Users (UCD)	
Timing and Alignment Shots	35
Target Shots	58
TOTAL	564

3.B OMEGA Facility Report

During this reporting period, the OMEGA laser has been reexamined for techniques to improve irradiation uniformity. Two systems were in the process of being integrated into the system to achieve this goal. The first of these, power balance, consists of energy balancing the beams while ensuring that the beam pulse shapes are exact across all 24 beams. The second system involves the smoothing of the fine speckle pattern on target produced by the distributed phase plates. Implementation of several subsystems to accommodate the scheme of smoothing has been accomplished and full integration is expected within the next quarter.

Power-balance evaluation of the frequency-tripled pulse shapes showed strong dependence on the phase-matching angles, polarization angle, and intensity. Using the fiber-coupled, four-beam UV streak camera, tests were done to empirically determine the sensitivity to each of these parameters. Simultaneously, extensive computer modeling was developed to aid in the interpretation of the results and understanding of the conversion process in general. Tests of the birefringence of the last amplification stage of OMEGA, the 90-mm rods, indicated a polarization control element between the amplifier and the conversion crystals was necessary for consistent optimal tripling efficiency.

A high-contrast, high-damage-threshold thin-film polarizer was developed at the University's Thin-Film Coating Facility, and 24 units suitable for installation were delivered in November. The implementation of these devices virtually eliminated the problem of spatially varying polarization states and shot-to-shot changes due to amplifier birefringence. Techniques for error-free phase-match angle tuning were developed, and software was implemented to compensate for any temperature variations from the nominal ambient condition. The combination of these factors has led to stable frequency conversion at $100\% \pm 5\%$ of theoretical performance. By accurately

calibrating the output energy diagnostics and balancing the energy in each beam, the last component of power balance is satisfied, yielding the best irradiation balance for direct-drive implosion experiments.

As power balance requires accurate energy balance, a new computerized system was developed to enable faster, more precise adjustment of the distribution of energy from the single driver-line beam to the 24 beamlines. Utilizing tight control of the polarization into the polarizing dielectric beam splitters and an active feedback system, beam-to-beam balance can now be achieved to levels better than 2% rms. A schematic diagram of the system (Fig. 37.37) depicts motorized wave plates to adjust splitter ratios and diodes to monitor the induced change. As the wave plates are manipulated, laser pulses are detected at the output of the system, fed into the computer, and, within 15 min, a complete rebalance of the distribution is accomplished. This capability gets the balance near the stability of the amplifier chains (currently 1.50% rms). Future efforts may improve on these results as the mechanisms of instability are identified and eliminated.

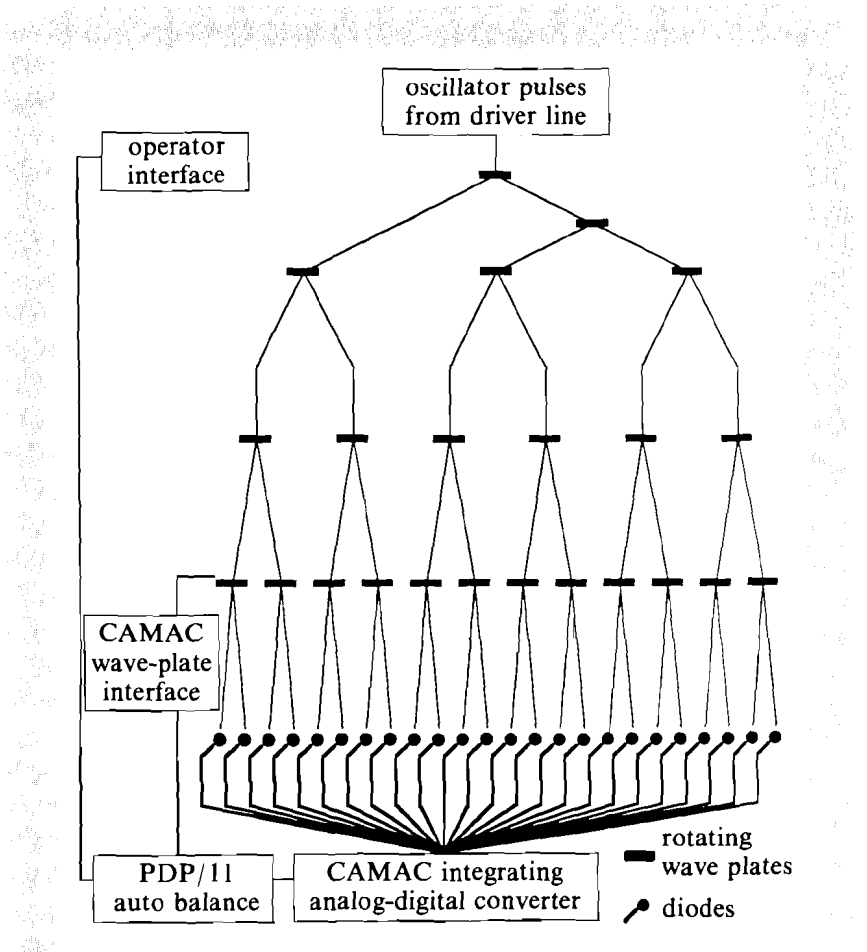

Fig. 37.37
Closed-loop feedback system used for intra-shot beam balancing on the OMEGA laser system.

Spatial smoothing of the power-balanced beams is the other goal of the new-term uniformity program. Since the scheme impacts mainly the front end of the laser system, there have been several changes made in the OMEGA driver line. Increasing the bandwidth of the laser, frequency dispersing the beam, and coupling the frequency-tripled light through distributed phase plates will result in a less-modulated target distribution. Other than the driver line, the only changes that had to be made to the laser were checking the *e*-axis orientation of the conversion crystals and rebuilding the cells to have the same dependence of phase-matching angle to wavelength. All crystals are reoriented at this time, ready for extended-bandwidth frequency-dispersed light. The theory and implementation of these concepts are covered elsewhere in this issue. This approach is one of the most significant laser developments since frequency tripling was pioneered at LLE in the early 1980s.

In summary, the Operations Group has been exclusively involved with the uniformity program. The following shot summary reflects the fact that most shots have been laser test shots for uniformity programs. Demonstration of spectral smoothing on target is this program's primary goal and, given the pace of current activity, results are expected early next quarter.

Driver Line and Test Shots	200
Laser	226
Target	51
TOTAL	477

ACKNOWLEDGMENT

This work was supported by the U.S. Department of Energy Office of Inertial Fusion under agreement No. DE-FC03-85DP40200 and by the Laser Fusion Feasibility Project at the Laboratory for Laser Energetics, which has the following sponsors: Empire State Electric Energy Research Corporation, New York State Energy Research and Development Authority, Ontario Hydro, and the University of Rochester. Such support does not imply endorsement of the content by any of the above parties.

PUBLICATIONS AND CONFERENCE PRESENTATIONS

Publications

A. Simon and R. W. Short, "Alternative Analysis of CO_2-Laser-Produced Plasma Waves," *Phys. Fluids* **31**, 3371–3374 (1988).

E. M. Epperlein, G. J. Rickard, and A. R. Bell, "Two-Dimensional Nonlocal Electron Transport in Laser-Produced Plasmas," *Phys. Rev. Lett.* **61**, 2453–2456 (1988).

D. J. Harter and P. Bado, "Wavelength Tunable Alexandrite Regenerative Amplifier," *Appl. Opt.* **22**, 4392–4395 (1988).

J. S. Coe, P. Maine, and P. Bado, "Regenerative Amplification of Picosecond Pulses in Nd:YLF: Effect of Gain Narrowing and Gain Saturation," *J. Opt. Soc. Am. B* **5**, 2560–2563 (1988).

K. Meyer, M. Pessot, G. Mourou, R. Grondin, and S. Chamoun, "Subpicosecond Photoconductivity Overshoot in Gallium Arsenide Observed by Electro-Optic Sampling," *Appl. Phys. Lett.* **53**, 2254–2256 (1988).

S. H. Batha, R. Bahr, L. M. Goldman, W. Seka, and A. Simon, "Observations of Enhanced Thomson Scattering," *Phys. Fluids* **31**, 3667–3674 (1988).

A. Simon, S. Radin, and R. W. Short, "Long-Time Simulation of the Single-Mode Bump-on-Tail Instability," *Phys. Fluids* **31**, 3649–3659 (1988).

J. C. Lee, J. H. Kelly, D. L. Smith, and S. D. Jacobs, "Gain Squaring in a Cr:Nd:GSGG Active Mirror Amplifier Using a Cholesteric Liquid Crystal Mirror." *IEEE J. Quantum Electron.* **24**, 2238–2242 (1988).

B. Yaakobi, D. Shvarts, T. Boehly, P. Audebert, R. Epstein, B. Boswell, M. C. Richardson, and J. M. Soures, "X-Ray Laser Studies at LLE," *IEEE Trans. Plasma Sci.* **16**, 505–511 (1988).

P. A. Jaanimagi, D. K. Bradley, J. Duff, G. G. Gregory, and M. C. Richardson, "Time-Resolving X-Ray Diagnostics for ICF," *Rev. Sci. Instrum.* **59**, 1854 (1988).

D. K. Bradley, P. A. Jaanimagi, J. Delettrez, C. P. Verdon, F. Marshall, J. D. Kilkenny, and P. Bell, "X-Ray Gated Images of Imploded Microballoons," *High Speed Photography, Videography, and Photonics VI*, (SPIE, Bellingham, WA, 1988), Vol. 981, pp. 176–185.

P. A. Jaanimagi, D. D. Meyerhofer, and M. C. Richardson, "Diagnosing One Picosecond Duration Ultra-High Brightness Sources," *High Speed Photography, Videography, and Photonics VI*, (SPIE, Bellingham, WA, 1988), Vol. 981, pp. 146–152.

Forthcoming Publications

A. Simon and R. W. Short, "Comments on 'Studies of Raman Scattering from Overdense Targets Irradiated of Several Kilojoules of 0.53-micron Laser Light'," to be published in *Physics of Fluids*.

H. G. Kim, "Recent Progress in Laser Fusion," to be published in the *Proceedings of the First KSEA Northeast Regional Conference*, Lehigh University, Bethlehem, PA.

M. Pessot, J. Squier, P. Bado, G. Mourou, and D. J. Harter, "Chirped Pulse Amplification of 300 fs Pulses in an Alexandrite Regenerative Amplifier," to be published in *IEEE Journal of Quantum Electronics*.

Y. F. Maa and S. H. Chen, "Synthesis of Thermotropic Liquid Crystalline Side-Chain Polymers Via Chemical Modification of Polymeric Carboxylic Acids," to be published in *Macromolecules*.

M. L. Tsai, S. H. Chen, K. L. Marshall, and S. D. Jacobs, "Thermotropic and Optical Properties of Chiral Nematic Polymers," to be published in *International Journal of Thermophysics*.

R. L. McCrory and C. P. Verdon, "Computer Modelling and Simulation in ICF," to be published in *Il Nouvo Cimento*.

F. W. Smith, S. Gupta, H. Q. Le, M. Frankel, V. Diadiuk, M. A. Hollis, D. R. Dykaar, G. A. Mourou, T. Y. Hsiang, and A. R. Calawa, "Picosecond GaAs-Based Photoconductive Optoelectronic Detectors," to be published in *Applied Physics Letters*.

S. Skupsky and T. Kessler, "A Source of Hot Spots in Frequency-Tripled Laser Light," to be published in *Optics Communications*.

J. C. Lee, A. Schmid, and S. D. Jacobs, "Effects of Anchoring Under Intense Optical Fields in a Cholesteric Liquid Crystal," to be published in *Molecular Crystals and Liquid Crystals.*

R. Epstein, "The Design and Optimization of Recombination XUV Lasers," to be published in *Physics of Fluids.*

E. M. Epperlein, G. J. Rickard, and A. R. Bell, "A Code for the Solution of the Vlasov-Fokker-Planck Equation in 1-D or 2-D," to be published in *Computer Physics Communications.*

W. R. Donaldson, "Radial Line Structure Experiments," to be published in the *Proceedings of the 4th Workshop: Pulse Power Techniques for Future Accelerators*, Erice, Sicily, 3-10 March 1988.

P. Maine and G. Mourou, "Amplification of 1 ns Pulses in Nd:Glass Followed by Compression to 1 ps," to be published in *Optics Letters.*

P. C. Cheng, S. P. Newberry, H. Kim, and M. D. Wittman, "X-Ray Contact Microradiography and Shadow Projection X-Ray Microscopy," to be published in the *European Journal of Cell Biology.*

R. L. McCrory, J. M. Soures, C. Verdon, M. Richardson, P. Audebert, D. Bradley, J. Delettrez, L. Goldman, R. Hutchison, S. Jacobs, P. Jaanimagi, R. Keck, H. Kim, T. Kessler, J. Knauer, R. Kremens, S. Letzring, F. Marshall, P. McKenty, W. Seka, S. Skupsky, and B. Yaakobi, "High-Density Laser-Fusion Experiments at the Laboratory for Laser Energetics," to be published in the *Proceedings of the 8th International Workshop on Laser Interaction and Related Plasma Phenomena.*

G. Mourou, "Picosecond Electro-Optic Sampling," to be published in the *Proceedings of the High Speed Electronics Conference*, Stockholm, Sweden, August 1986.

R. L. McCrory and J. M. Soures, "Inertially Confined Fusion," to be published in *Applications of Laser Plasmas,* Chapter 7.

O. Barnouin, B. Yaakobi, J. Delettrez, R. Epstein, P. Jaanimagi, and L. M. Goldman, "Experimental and Numerical Study of Thermal Transport in 24-Beam Ultraviolet Irradiation of Spherical Targets," to be published in the *Journal of Applied Physics.*

S. Krishnamurthy and S. H. Chen, "Purification of Thermotropic Liquid Crystalline Siloxane Oligimer with Supercritical Carbon Dioxide," to be published in *Makromol. Chem.*

Conference Presentations

N. Sampat and S. Swales, "Real-Time Image Processing Techniques Used in Studying Cryogenically Cooled Laser Fusion Targets," presented at the 5th Annual International Electronic Imaging Exposition and Conference, Boston, MA. 3–6 October 1988.

R. L. McCrory, J. M. Soures, C. P. Verdon, F. J. Marshall, S. A. Letzring, S. Skupsky, R. L. Kremens, J. P. Knauer, H. Kim, J. Delettrez, R. L. Keck, and D. K. Bradley, "Direct-Drive Laser Implosion of DT to 20–40 g/cm^3," presented at the 19th ECLIM Conference, Madrid, Spain. 3–7 October 1988.

J. Knauer, J. M. Soures, R. L. McCrory, D. Bradley, R. S. Craxton, J. Delettrez, R. Epstein, P. Jaanimagi, R. Keck, R. Kremens, S. Letzring, F. J. Marshall, M. C. Richardson, W. Seka, R. Short, S. Skupsky, C. Verdon, and B. Yaakobi, "Diagnostics for Laser-Fusion High-Density Implosion Experiments," presented at the American Vacuum Society Conference, Atlanta, GA, 3–9 October 1988 (invited talk).

T. Kessler, R. S. Craxton, W. Donaldson, J. Kelly, S. Letzring, and S. Skupsky, "Phase Conversion for a Laser Microfusion Facility," presented at the 8th Topical Meeting on the Technology of Fusion Energy, Salt Lake City, UT, 9–13 October 1988.

R. L. McCrory, J. M. Soures, C. P. Verdon, F. J. Marshall, S. A. Letzring, T. J. Kessler, J. P. Knauer, H. Kim, S. D. Jacobs, R. L. Kremens, S. Skupsky, R. L. Keck, D. K. Bradley, W. D. Seka, B. Yaakobi, P. A. Jaanimagi, J. A. Delettrez, and P. W. McKenty, "High Density Direct-Drive Cryogenic Implosion Experiments," presented at the 12th International IAEA Conference on Plasma Physics and Controlled Nuclear Fusion Research, Nice, France, 12–19 October 1988.

M. Guardalben, A. Bevin, K. Marshall, A. Schmid, and F. Kreuzer, "1053-nm High-Field Effect in Monomeric and Polymeric Conjugated Systems," presented at the Symposium on Optical Materials for High Power Lasers, Boulder, CO, 16–28 October 1988.

The following presentations were made at the 30th Annual APS Conference, Hollywood, FL, 31 October–4 November 1988:

S. Batha, D. D. Meyerhofer, W. Seka, A. Simon, and L. M. Goldman, "Observations of Raman Up-Scatter in a Long Scale-Length Plasma."

T. Boehly, B. Yaakobi, D. Shvarts, P. Audebert, R. Epstein, D. D. Meyerhofer, M. C. Richardson, M. Russotto, J. M. Soures, and J. Wang, "X-Ray Laser Studies at LLE."

D. K. Bradley, J. Delettrez, C. Hestdalen, P. A. Jaanimagi, J. P. Knauer, F. J. Marshall, C. P. Verdon, J. D. Kilkenny, and P. Bell, "X-Ray Imaging of Microballoons Imploded by the OMEGA Laser System."

R. S. Craxton, "Simulations of X-Ray Amplified Spontaneous Emission From Line-Focus Laser-Produced Plasmas."

J. Delettrez, D. D. Meyerhofer, R. Epstein, J. P. Matte, H. Pepin, J. Kiefer, M. Chaker, and P. Audebert, "Modeling of the Interaction of 1-ps Laser Pulses with Solid Targets at One Micron."

E. M. Epperlein and R. Short, "Nonlocal Electron Transport Effects on the Filamentation of Laser Beams."

R. Epstein, S. Skupsky, and J. Delettrez, "Measuring High Compression in Laser Fusion Experiments Using the Energy Spectrum of Knock-On Particles."

P. A. Jaanimagi, D. K. Bradley, J. Delettrez, T. Kessler, P. W. McKenty, M. C. Richardson, S. Skupsky, and C. P. Verdon, "Studies of Time-Resolved Illumination Uniformity on OMEGA."

R. L. Keck, S. Skupsky, J. P. Knauer, R. L. Kremens, F. J. Marshall, and C. P. Verdon, "Target ρR Measurements of OMEGA Implosions Via the 'Knock-On' Technique."

J. P. Knauer, R. L. McCrory, J. M. Soures, C. P. Verdon, F. J. Marshall, S. A. Letzring, T. J. Kessler, H. Kim, S. D. Jacobs, R. L. Kremens, S. Skupsky, R. L. Keck, D. K. Bradley, W. D. Seka, B. Yaakobi, P. A. Jaanimagi, J. A. Delettrez, P. W. McKenty, and M. C. Richardson, "OMEGA Implosions of Gas Filled CH Shells and CH Coated GMB's."

S. A. Letzring, T. J. Kessler, H. Kim, R. Gram, and M. Wittman, "Experimental Apparatus for Producing and Measuring Cryogenic Fuel-Filled Targets on the OMEGA Laser System."

R. S. Marjoribanks, M. C. Richardson, D. K. Bradley, J. Delettrez, R. Epstein, G. G. Gregory, and P. A. Jaanimagi, "Time-Resolved Ionization Studies in UV-Laser-Produced Plasmas."

F. J. Marshall, S. A. Letzring, C. P. Verdon, S. Skupsky, R. L. Keck, J. P. Knauer, R. L. Kremens, D. K. Bradley, T. Kessler, J. Delettrez, H. Kim, R. L. McCrory, and J. M. Soures, "Cryogenic Target Implosion Experiments with OMEGA."

P. W. McKenty, S. Skupsky, C. P. Verdon, and R. L. McCrory, "Numerical Evaluation of Time-Dependent Ablation Pressure Nonuniformities in Imploding ICF Targets."

D. D. Meyerhofer, R. Bahr, S. Batha, H. Chen, M. Richardson, and S. Uchida, "Backscattering Measurements During High Intensity, 1 ps, Laser-Solid Interactions."

M. C. Richardson, D. K. Bradley, J. Delettrez, R. Epstein, P. A. Jaanimagi, B. Yaakobi, C. F. Hooper, R. C. Mancini, D. Kilcrease, and L. Woltz, "Time-Resolved, X-Ray Diagnosis of Compressed Ar-Filled Polymer Shell Targets."

R. W. Short, "Raman Forward Scatter in Long-Scale-Length Low-Temperature Plasmas."

A. Simon and R. W. Short, "Saturated Plasma Wave Model of Raman Scattering Experiments."

S. Skupsky, R. S. Craxton, T. Kessler, S. Letzring, R. Short, and J. M. Soures, "Laser Beam Smoothing by Spectral Dispersion (SSD)."

J. M. Soures, "High-Density, Direct-Drive Target Implosion Experiments" (invited talk).

C. P. Verdon, F. J. Marshall, S. Letzring, D. K. Bradley, J. Delettrez, R. L. Keck, J. P. Knauer, R. L. Kremens, R. L. McCrory, S. Skupsky,

and J. M. Soures, "Theoretical Interpretation of OMEGA High Density Implosion Experiments."

J. Wang, T. Boehly, B. Yaakobi, D. Shvarts, P. Audebert, R. Epstein, D. D. Meyerhofer, M. C. Richardson, M. Russotto, and J. M. Soures, "Analysis of Multiple-Foil XRL Experiments."

R. C. Mancini, C. F. Hooper, D. Kilcrease, L. Woltz, M. C. Richardson, D. K. Bradley, J. Delettrez, R. Epstein, P. A. Jaanimagi, and B. Yaakobi, "Broadening of Satellite and Resonance Lines from High-Density Laser Implosion Experiments."

J. C. Moreno, S. Goldsmith, H. R. Griem, R. Epstein, J. Knauer, and P. Jaanimagi, "Radiation Cooling in Laser-Produced Plasmas due to High-Z Layers."

A. Lindquist, S. D. Jacobs, and V. Plotsker, "Chemo-Mechanical Polishing of Phosphate Glass as a Pretreatment of Rapid Final Polishing," presented at the Workshop on Optical Fabrication and Testing, Santa Clara, CA, 2-4 November 1988.

H. Kim, "Recent Progress in Laser Fusion," presented at the First KSEA Northeast Regional Conference, Lehigh University, Bethlehem, PA, 5 November 1988.

S. D. Jacobs, "Optical Materials for Laser Applications," presented at the American Institute of Chemical Engineering Conference, Washington, DC, 27 November-2 December 1988.

M. Pessot, J. Squier, G. Mourou, and D. Harter, "Generation of 100 fs, 20 GW Pulses in Alexandrite Using Chirped Pulse Amplification," presented at the Optical Society of America Annual Meeting, Sunnyvale, CA, 31 November-4 December 1988.

ACKNOWLEDGMENT

The work described in this volume includes current research at the Laboratory for Laser Energetics, which is supported by Empire State Electric Energy Research Corporation, New York State Energy Research and Development Authority, Ontario Hydro, the University of Rochester, and the U.S. Department of Energy Office of Inertial Fusion under agreement No. DE-FC03-85DP40200.